Volume 2, Issue 4, December 2022

INTELLIGENCE & ROBOTICS

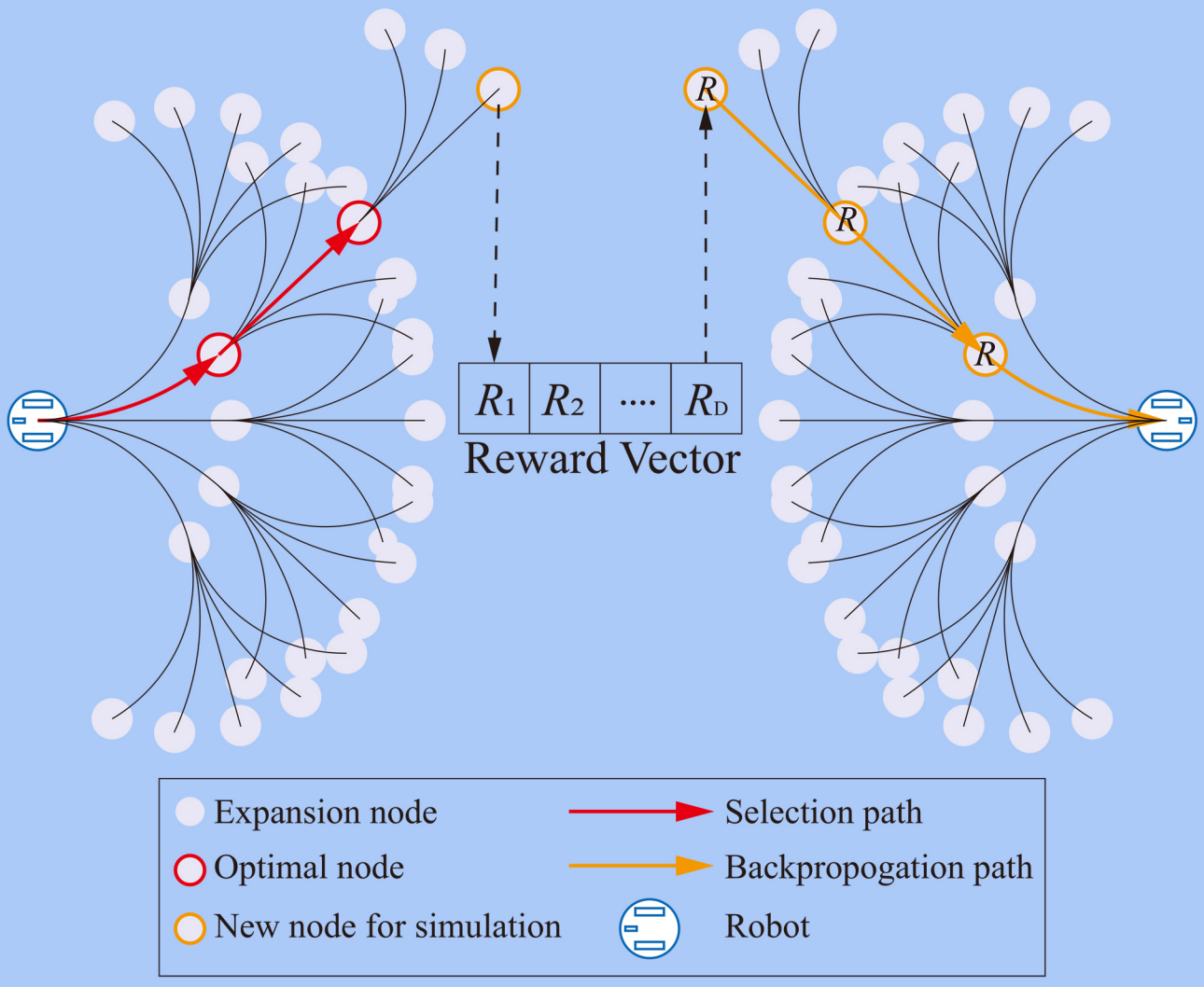

An informative planning-based multi-layer robot navigation system as applied in a poultry barn

Tingjun Lei, Guoming Li, Chaomin Luo, Li Zhang, Lantao Liu, Richard Stephen Gates

Open Access
ISSN 2770-3541 (Online)
www.intellrobot.com

Editor-in-Chief

Simon X. Yang

Prof. Simon X. Yang is currently the Head of the Advanced Robotics and Intelligent Systems Laboratory at the University of Guelph. His research interests include artificial intelligent, robotics, sensors and multi-sensor fusion, wireless sensor networks, control systems, bio-inspired intelligence, machine learning, neural networks, fuzzy systems, and computational neuroscience.

Our Features

(1) Gold Open Access
(2) Strong Editorial Board
(3) Rigorous Peer-review
(4) Free English Ianguage Editing Service
(5) Online First Once Accepted
(6) Free Publication Before 31 Dec 2024
(7) Wide Promotion (Twitter\LinkedIn\WeChat\Facebook)

Editorial Board

- 1 Editor-in-Chief
- 2 Executive Editor
- 5 Advisory Editorial Members
- 42 Associate Editors
- 20 Youth Editorial Board Members

Scope

Top-quality unpublished original technical and non-technical application-focused articles are welcome from intelligence and robotics, particularly on the inter-disciplinary areas of intelligence and robotics, including but not limited to the following areas:

- biological, bio-inspired, and artificial intelligence;
- neural networks, fuzzy systems, and evolutionary algorithms;
- sensing, multi-sensor fusion, localization, data analysis, modeling, planning, and control for various mobile, aerial, and underwater robotic systems;
- robot cooperation, teleoperation, and human-machine interactions.
- development and maintenance of real-world intelligent and robotic systems by multidisciplinary teams of scientists and engineers.

Journal Home
https://intellrobot.com/

Submission Link
https://oaemesas.com/login?JournalId=ir

EDITORIAL BOARD

EDITORIAL BOARD

GENERAL INFORMATION

About the Journal

Intelligence & Robotics (*IR*), ISSN 2770-3541 (Online), publishes top-quality unpublished original technical and non-technical application-focused articles on intelligence and robotics, particularly on the interdisciplinary areas of intelligence and robotics. The Journal seeks to publish articles that deal with the theory, design, and applications of intelligence and robotics, ranging from software to hardware. The scope of the Journal includes, but is not limited to, biological, bio-inspired, and artificial intelligence; neural networks, fuzzy systems, and evolutionary algorithms; sensing, multi-sensor fusion, localization, data analysis, modeling, planning, and control for various mobile, aerial, and underwater robotic systems; and robot cooperation, teleoperation and human-machine interactions. The Journal would be interested in distributing development and maintenance of real-world intelligent and robotic systems by multidisciplinary teams of scientists and engineers.

Information for Authors

Manuscripts should be prepared in accordance with Author Instructions.
Please check https://intellrobot.com/pages/view/author_instructions for details.
All manuscripts should be submitted online at https://oaemesas.com/login?JournalId=ir.

Copyright

Permissions

For information on how to request permissions to reproduce articles/information from this journal, please visit www.intellrobot.com.

Disclaimer

The information and opinions presented in the journal reflect the views of the authors and not of the journal or its Editorial Board or the Publisher. Publication does not constitute endorsement by the journal. Neither the *IR* nor its publishers nor anyone else involved in creating, producing or delivering the *IR* or the materials contained therein, assumes any liability or responsibility for the accuracy, completeness, or usefulness of any information provided in the *IR*, nor shall they be liable for any direct, indirect, incidental, special, consequential or punitive damages arising out of the use of the *IR*. *IR*, nor its publishers, nor any other party involved in the preparation of material contained in the *IR* represents or warrants that the information contained herein is in every respect accurate or complete, and they are not responsible for any errors or omissions or for the results obtained from the use of such material. Readers are encouraged to confirm the information contained herein with other sources.

Published by

OAE Publishing Inc.
245 E Main Street Ste 107, Alhambra CA 91801, USA
Website: www.oaepublish.com

Contacts

E-mail: editorial@intellrobot.com
Website: www.intellrobot.com

Intelligence & Robotics

CONTENTS

Volume 2 / Issue 4 /

Research Article

Review

Lei *et al. Intell Robot* 2022;2(4):313-32
DOI: 10.20517/ir.2022.18

Intelligence & Robotics

Research Article

Open Access

Check for updates

An informative planning-based multi-layer robot navigation system as applied in a poultry barn

Tingjun Lei[1], Guoming Li[2,3], Chaomin Luo[1], Li Zhang[4], Lantao Liu[5], Richard Stephen Gates[2,3,6]

[1]Department of Electrical and Computer Engineering, Mississippi State University, Mississippi State, MS 39762, USA.
[2]Department of Agricultural and Biosystems Engineering, Iowa State University, Ames, IA 50011, USA.
[3]Department of Animal Science, Iowa State University, Ames, IA 50011, USA.
[4]Department of Poultry Science, Mississippi State University, Mississippi State, MS 39762, USA.
[5]Department of Intelligent Systems Engineering, Indiana University, Bloomington, IN 47408, USA.
[6]Egg Industry Center, Iowa State University, Ames, IA 50011, USA.

Correspondence to: Prof. Chaomin Luo, Department of Electrical and Computer Engineering, Mississippi State University, 406 Hardy Road, Mississippi State, MS 39762, USA. E-mail: Chaomin.Luo@ece.msstate.edu; ORCID: 0000-0002-7578-3631

How to cite this article: Lei T, Li G, Luo C, Zhang L, Liu L, Gates RS. An informative planning-based multi-layer robot navigation system as applied in a poultry barn. *Intell Robot* 2022;2(4):313-32. http://dx.doi.org/10.20517/ir.2022.18.

Received: 10 Jun 2022 **First Decision:** 29 Jul 2022 **Revised:** 13 Aug 2022 **Accepted:** 25 Aug 2022 **Published:** 12 Oct 2022

Academic Editor: Simon X. Yang **Copy Editor:** Jia-Xin Zhang **Production Editor:** Jia-Xin Zhang

Abstract

Many real-world robot applications, as found in precision agriculture, poultry farms, disaster response, and environment monitoring, require search, locate, and removal (SLR) operations by autonomous mobile robots. In such application settings, the robots initially search and explore the entire workspace to find the targets, so that the subsequent robots conveniently move directly to the targets to fulfill the task. A multi-layer robot navigation system is necessary for SLR operations. The scenario of interest is the removal of broiler mortality by autonomous robots in poultry barns in this paper. Daily manual collection of broiler mortality is time- and labor-consuming, and an autonomous robotic system can solve this issue effectively. In this paper, a multi-layer navigation system is developed to detect and remove broiler mortality with two robots. One robot is assigned to search a large-scale workspace in a coverage mode and find and locate objects, whereas the second robot directly moves to the located targets to remove the objects. Directed coverage path planning (DCPP) fused with an informative planning protocol (IPP) is proposed to efficiently search the entire workspace. IPP is proposed for coverage directions in DCPP devoted to rapidly achieving spatial coverage with the least estimation uncertainty in the decomposed grids. The detection robot consists of a developed informative-based directed coverage path planner and a You Only Look Once (YOLO) V4-based dead bird detector. It refines and optimizes the coverage path based on historical data on broiler mortality distribution in a broiler barn. The removal robot collects dead broilers driven by a new hub-based multi-target path routing (HMTR) scheme, which is applicable to row-based environments. The proposed methods show great potential to navigate in broiler barns ef-

ficiently and safely, thus being a useful component for robotics. The effectiveness and robustness of the proposed methods are validated through simulation and comparison studies.

Keywords: Directed coverage path planning, informative planning protocol (IPP), broiler mortality, YOLO V4, hub-based multi-target routing (HMTR) scheme

1. INTRODUCTION

1.1. Background

Global broiler production has been growing since the 1960s; in the United States alone, over 9.22 billion broilers were produced in 2020 at a value of 21.7 billion dollars[1]. A modern broiler barn holds 25,000 to 100,000 broilers on the open litter floor. Within the intensive production system, broiler mortality could be largely due to disease and metabolic problems and unsuitable environmental conditions and management[2]. The mortality rate is commonly 5% in an eight-week production cycle[1] and can reach 10% without appropriate management[3]. As a daily task, producers need to collect and remove broiler mortality timely, which is an arduous, time-consuming, and unpleasant task. A farmer spends hours daily identifying, gathering, and transporting dead birds in a typical broiler barn (e.g., 25,000 birds/barn). Manual mortality collection is relatively simple when broilers are young because they are lightweight and small. However, older broilers are bigger and weigh more, and, to avoid overwork, farmers may deposit the mortality in scattered piles within the broiler barn for subsequent removal[3]. A dead bird residing on a litter floor can result in higher levels of bacterial accumulation and increase the risk of disease spread via direct contact or vector transmission[3]. Additionally, caretakers risk their health if exposed to harsh working environments (e.g., concentrated ammonia and dust) for a long term[2]. Therefore, autonomous robotic systems for collecting broiler mortality are warranted to improve labor efficiency and reduce biosecurity issues.

Robotic systems have been developed to facilitate poultry production[4,5]. Vroegindeweij *et al.* developed a PoultryBot to avoid obstacles and pick up floor eggs in cage-free hen housing systems[6]. Li *et al.* developed an egg picking robot based on a deep learning detector and a robot arm[7]. Some poultry robots are commercialized to help farmers monitor environments, inspect bird health and welfare status, stimulate bird movement, aerate litter, and disinfect poultry barns. However, robots for poultry mortality removal are still not commercially available. Many aspects need to be considered for developing such a robot[8]. Among them, robot path planning is one of the most essential parts of effective and efficient determination of robot routes[9,10].

1.2. Related work

Many approaches have been proposed to achieve reliable autonomous robot motion planning, such as ant colony optimization (ACO)[11–13], fireworks algorithm (FWA)[14], bat-pigeon algorithm (BPA)[15], graph-based method[16], and neural network models[17–19]. Lei *et al.* proposed a hybrid model to optimize the trajectory of the global path using a graph-based search algorithm associated with an ant colony optimization (ACO) method[11]. A hybrid fireworks algorithm with LIDAR-based local navigation capable of generating short collision-free trajectories in unstructured environments was developed[14]. The cuckoo search algorithm has also been successfully applied to the efficient and safe navigation of robots[20]. A bat-pigeon algorithm[15] was developed with crack detection-driven autonomous vehicle navigation and mapping, in which a local search-based bat algorithm and a global search-based pigeon-inspired optimization algorithm are effectively integrated to improve the speed and performance of robot path planning and mapping. Wang and Meng[16] suggested a nonuniform sampling technique, which efficiently computes high-quality collision-free paths based on a generalized Voronoi graph. A biologically motivated neural network model using a shunting equation was proposed by Yang and Luo[17] for real-time path planning with obstacle avoidance. Luo *et al.* extended the model of trajectory planning with safety consideration in conjunction with the virtual obstacle

algorithm[21]. However, the design and implementation of path planning in a broiler barn involve multiple aspects for mortality removal. Especially with the large scale of modern broiler barns (e.g. 12 m × 200 m), poultry mortality is widely distributed anywhere in the barn, which increases the difficulty of detecting and removing dead broilers. Therefore, we propose a system for searching and removing broiler mortality with two robots. One is a broiler mortality detection robot and the other is a broiler mortality removal robot. The major function of the detection robot is to precisely and efficiently search the whole broiler barn and indicate the position of dead broilers. Thus, coverage path planning (CPP) algorithms need to be introduced to assist robots in search and exploration tasks, such as bio-inspired neural networks[22], Boustrophedon grid decomposition[23], deep learning[24,25], *etc.*

Luo and Yang[22] developed the bio-inspired neural network (BNN) method to navigate robots to perform complete coverage path planning (CCPP) while avoiding obstacles within dynamic environments. The robot is attracted to unscanned areas and repelled by the previous scanned areas or obstacles based on the neural activity through the BNN model. The next position of the robot depends on the current position of the robot and neuron activity associated with its current position. Zhu *et al.* proposed a complete coverage path planning model using Glasius BNN, which is extended to multiple robots to lower the overall search time and improve efficiency[19]. Unlike the BNN approach, the boundary representation model that defines the workspace is adopted by the Boustrophedon cellular decomposition (BCD) method and deep reinforcement learning approach (DRL). The BCD method proposed by Acar and Choset[23] decomposes the environment into many line scan partitions explored through a back-and-forth path (BFP) in the same direction. BCD is an effective CCPP method for more diverse, non-polygonal obstacles in a workspace. In trapezoidal decomposition as a cell, it is covered in back-and-forth patterns. For a complex configuration space with irregular-shaped obstacles, BCD needs to construct a graph that represents the adjacency connections of the cells in the Boustrophedon decomposition. Similarly, Nasirian *et al.* utilized traditional graph theory to segment the workspace and proposed a deep reinforcement learning approach to solve the CCPP problem in a complex workspace[24]. Lei *et al.* proposed a deep learning method to detect the workspace and generate turning waypoints for the robot to complete the coverage of the entire workspace[25]. The trajectory generated by the above-presented algorithms completely covers the workspace in light of the size of the robot, which is more suitable for a large-sized workspace with a broad sensing range. However, with the limited sensing range of robots in broiler barns, a complete coverage trajectory requires a large amount of time and energy, which may not be affordable to the farmers.

The methods of object detection have been extensively studied, and many object detectors are utilized in many agricultural settings. Li *et al.* proposed a fast region-based CNN (R-CNN) detector with high accuracy to adapt to the illumination of different colored lights in the farm and detect the cage-free floor eggs[26]. A mask R-CNN object detector was developed by Li *et al.* to detect hen preening behaviors in barns to automatically monitor poultry behaviors, judge the comfort level of hens, and assist welfare-oriented poultry management[27]. Bochkovskiy *et al.* proposed a YOLO V4 object detector, which is a deep learning-based object detection technique with high accuracy[28]. It is an effective object detector to localize objects in real-time processing.

1.3. Proposed methods and original contribution

A directed coverage path planning (DCPP) fused with an informative planning protocol (IPP) is proposed to efficiently search the entire barn. The broiler barn is first decomposed into large grids based on the workspace dimensions to obtain overall global trajectories with coverage directions. IPP continues to rapidly achieve spatial coverage with the least estimation uncertainty in the decomposed grids. Flexible and efficient trajectories are formed by utilizing historical information of broiler mortality spatial distribution[29] and the direction information from the previous steps. With the assistance of current state-of-the-art computer vision algorithms in precision agriculture, such as deep learning techniques[30], the robot could detect dead birds in the grids of vision range and find the mortality location for the removal robot. Such a comprehensive path planning

method for the localization robot could pinpoint targets and avoid unnecessary searching trajectories, saveing the robot time and energy.

After the locations of dead broilers are precisely and efficiently identified, the removal robot is deployed to collect the mortalities. To save time and energy, the total length of the path to remove multiple dead broilers in succession should be minimized[31]. In that regard, a new hub-based multi-target routing (HMTR) scheme is developed in this paper, which originates from the row-based environment routing of broiler barn. By introducing hub grids, computational efficiency is improved for distance calculations between targets. Based on the locations of the dead birds, the best visiting sequence is determined while planning collision-free trajectories simultaneously. Furthermore, a reactive local navigator is developed to dynamically update the path and map in real time to avoid moving obstacles and unforeseen obstacles in the dynamic environment. This is of great help to robot safety and obstacle avoidance and prolongs the life of the robot.

Overall, we propose a system for detecting and removing broiler mortality with two robots. The detection robot consists of an informative directed coverage path planner and a You Only Look Once (YOLO) V4-based dead bird detector. The removal robot collects dead broilers by the hub-based multi-target path routing (HMTR) scheme. Meanwhile, with the reactive local navigator, the robots avoid obstacles and reach the target position through the real-time updated information of the onboard LIDAR sensors.

The major contributions of this paper are summarized as follows:

- A multi-layer robot navigation system for search, locate, and remove (SLR) operations is developed for the removal of dead broilers in a poultry barn to reduce the daily laborious and time-consuming work.
- A directed coverage path planning (DCPP) method integrated with an informative planning protocol (IPP) is developed to efficiently search targets in a large-scale workspace, which is initially decomposed into grids, and the optimal coverage directions are obtained based on the workspace. The detection robot adaptively explores the workspace to generate the trajectory in the grids in light of the historical data of searched targets and the coverage directions.
- The informative planning protocol (IPP) is developed to integrate coverage directions devoted to rapidly achieving *spatial* coverage with the least estimation uncertainty in the decomposed grids.
- To efficiently reach the targets, a new hub-based multi-target path routing (HMTR) scheme is proposed to row-based environments. The total visiting distance is minimized through obtained targets to generate an optimal sequence to connect all the targets.
- Practically, to apply this navigation system in the poultry barn, multiple robots with this developed navigation system are utilized, consisting of a dead broiler search robot to search and locate the dead broilers and a dead broiler removal robot to collect the dead broiler afterwards.

2. PRELIMINARY DEFINITION

2.1. Workspace setup and robot configuration

The complex barn environment is simplified into a rectangular robot workspace (152 m long × 12 m wide) based on typical United States broiler barn dimensions[32]. The workspace where the robot needs to collect dead broilers consists of multiple feeding and drinking lines that run the length of the barn, start and end positions of the robot, and dead and live broilers that are randomly located in the barn. Two feeding and three drinking lines are arranged in parallel in the middle, each measuring 140 m long and 0.3 m wide [Figure 1]. The distance between lines is 1.75 m, and endpoints of the lines are 6 m away from the ends of the barn. The start and end positions are located near the gate of the barn and could be altered in a real-world application. Live/dead birds are simplified as 20 cm diameter circles. With a stocking density of nearly 929 cm^2/bird (1 ft^2/bird), the barn is assumed to have 20,000 birds. The workspace is illustrated in Figure 1.

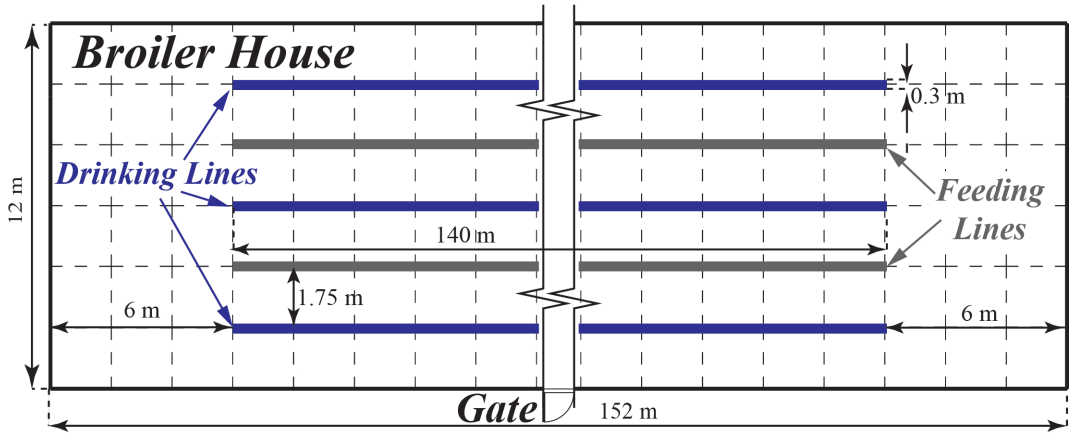

Figure 1. Illustration of simulated workspace based on a broiler barn. Blue lines are drinking lines, while grey lines are feeding lines. In total, 20,000 broilers are randomly distributed in the workspace.

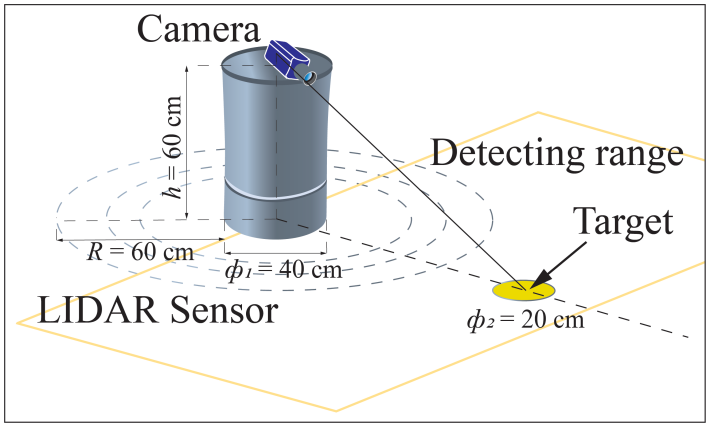

Figure 2. Illustration of the cylindrical robot with a camera and LIDAR sensor. Cylinder represents robot, dot circles represent LIDAR sensor scans, while the yellow circle is a target (dead broiler).

The tested robots in this paper are assumed to be cylinders, each 20 cm in radius and 60 cm in height. The payload based on bird volume (10 cm in height and 11–30 cm in diameter[33]) is estimated as 30 dead birds. It is equipped with a camera to capture bird images in real time. The entire workspace is decomposed into non-overlapping grids, each measuring 200 cm long × 200 cm wide [Figure 1]. A LIDAR sensor is mounted into the robot to detect static (i.e., feeding and drinking lines) and dynamic (i.e., live broilers) obstacles. The effective maximum detection range is limited by complex environments to a radius with approximately 60 cm. The basic function of the robot is to search for dead and live broilers during their moving, arrive at the mortality, and avoid moving birds. The parameters of the robot are set as follows: maximum linear velocity of 1 m/s, maximum angular velocity of 20 rad/s, maximum acceleration/deceleration of 0.2 m/s^2, and maximum angular acceleration/deceleration of 50 rad/s^2. These parameters are suited to industrial levels. The proposed autonomous robot is illustrated in Figure 2.

2.2. Overall workflow for robot path planning

The overall procedure of the multi-layer robot navigation system is shown in Figure 3. The workspace is decomposed into a grid-based working map and fed into the robots. The whole robotic framework consists of the detection robot and removal robot, where the detection robot is run at first followed by the removal robot. The detection robot considers the map information and historical mortality distribution while it outputs a

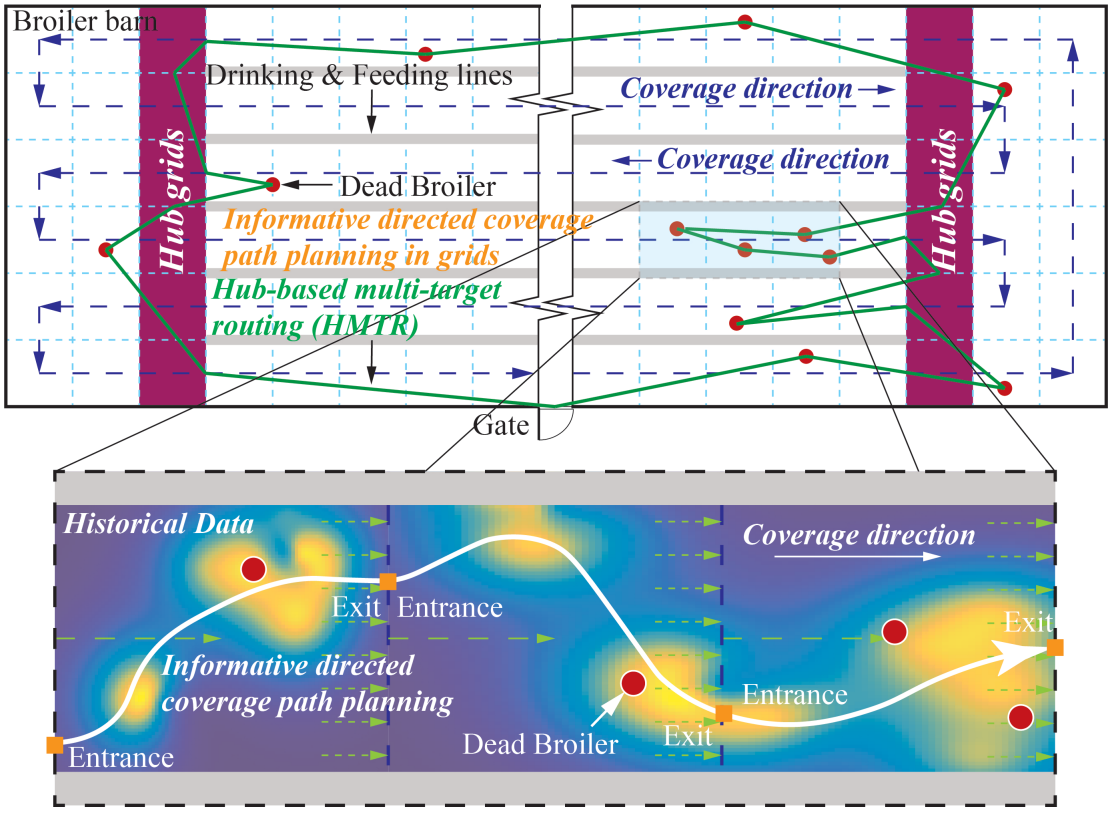

Figure 3. Overall procedure of the multi-layer. The dashed blue lines represent the DCPP with the coverage directions. The informative planning protocol integrates coverage directions and continues to rapidly achieve spatial coverage with the least estimation uncertainty in the decomposed grids. Red circles are the dead broilers found by YOLO V4-based dead broiler detector in the boiler barn. The maroon grids are the hubs in the row-based environment. The green lines represent the hub-based multi-target paths. Note that the heat map in this figure only represents the distribution of the historical data of dead chickens, which is different from the information heat maps with generated coverage direction information in the rest of the paper. DCPP: Defined contribution pension plan.

mortality-based coverage trajectory. It mainly consists of two parts: (1) informative directed coverage path planning; and (2) target detection. The removal robot determines the final trajectory in real time by utilizing the coordinates of dead birds throughout a broiler barn. It consists of an HMTR scheme.

3. METHOD

3.1. The overall workflow of the proposed work

Details of the corresponding algorithms are described in the following sections. The overall workflow of the path planning for the broiler mortality detection and removal robots is illustrated in Figure 4.

The proposed multi-layer robot navigation system illustrated in Figure 4 consists of informative directed coverage path planning (directed coverage path planning and informative planning protocol), the hub-based multi-target routing (HMTR) scheme, target detection, and YOLO V4. In this navigation system, the initial robot is tasked with finding and locating objects in a large-scale setting, while the second robot proceeds directly to the targets it has discovered to remove the objects. To effectively search the full vast workspace, a directed coverage path planning (DCPP) coupled with an informative planning protocol (IPP) is proposed in the system, as shown in Figure 4. To quickly achieve spatial coverage with the least amount of estimation error in the deconstructed grids, IPP is recommended for coverage directions in DCPP. The detection robot is driven by the You Only Look Once (YOLO) V4-based dead bird detector and an informative-based directed coverage path planner. As applied in the poultry barn, two robots are utilized in this multi-layer navigation system to

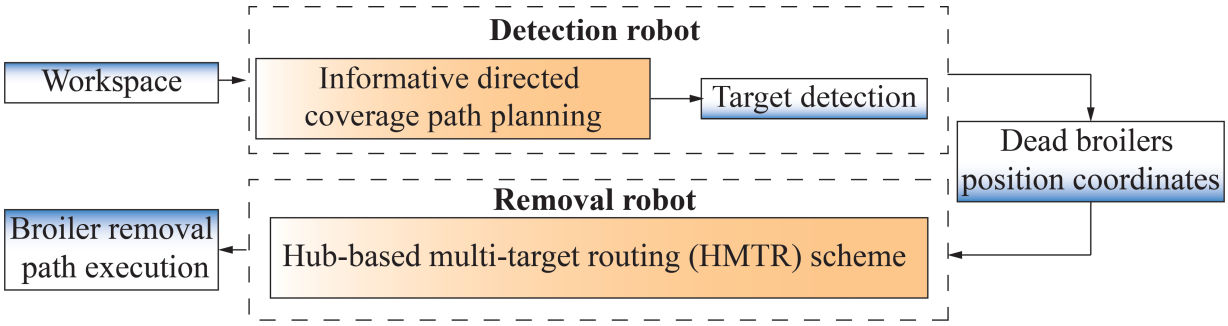

Figure 4. Overall workflow of the path planning for the broiler mortality detection and removal robots. The dynamic window approach (DWA) local navigator is also utilized to avoid live broilers in simulations.

find and eliminate broiler mortality.

3.2. Directed coverage path planning

The directed coverage path planning (DCPP) is utilized to generate an overall trajectory of the broiler mortality detection robot. It should meet the following requirements:

1. The mobile robot must move through all regions of interest in the barn.
2. Motion trajectories should be simplified as straight lines.
3. The robot should cover the regions with minimal overlapping.
4. The path should be optimized with one of the criteria, such as distance, time, and energy.
5. The start and end points for the robots should be co-located so that farmers do not need to enter the barn and retrieve the stopped robot from the barn interior.

In this paper, the criterion to generate a directed coverage path is the total shortest path, which could save running energy for the robots. In the decomposed working map, the adjacent grids share at least one boundary, while nodes of the adjacent grids are connected to form overall trajectories. There are two commonly used methods for CPP: zigzag motion planning and spiral motion planning, namely back-and-forth and boundary sweep methods[17].

The robot moves along the lengthwise direction of the workspace under the zigzag motion planning, and the total path length is calculated by Equation (1):

$$\mathcal{L}_z = (\mathcal{L}_l - \mathcal{L}_g) \times \left(\frac{\mathcal{L}_s}{\mathcal{L}_g}\right) + \mathcal{L}_s - \mathcal{L}_g \tag{1}$$

where $\mathcal{L}_z$ is the total length of zigzag motion planning; L_l is the length of the long side of a workspace; $\mathcal{L}_s$ is the length of the short side of a workspace; and $\mathcal{L}_g$ is the length of a grid. The robot under the zigzag motion planning moves along the long side of the workspace $\mathcal{L}_s/\mathcal{L}_g$ times and along the short side $\mathcal{L}_s/\mathcal{L}_g - 1$ times. It turns $2(\mathcal{L}_s/\mathcal{L}_g - 1)$ times.

Under the spiral motion planning, the robot moves along the boundary of the workspace progressively and at the same time toward the center spirally. The total travel distance (TD) on the short side $\mathcal{D}_s$ is

$$\mathcal{D}_s = \frac{\mathcal{L}_s \times (\mathcal{L}_s - \mathcal{L}_g)}{2 \times \mathcal{L}_g} \tag{2}$$

The total travel distance on the long side $\mathcal{D}_l$ is

$$\mathcal{D}_l = \frac{2\mathcal{L}_l\mathcal{L}_s - (\mathcal{L}_s)^2 + \mathcal{L}_g\mathcal{L}_s - 2(\mathcal{L}_g)^2}{2\mathcal{L}_g} \tag{3}$$

$$\mathcal{L}_p = \mathcal{D}_s + \mathcal{D}_l = \frac{2\mathcal{L}_l\mathcal{L}_s - 2\left(\mathcal{L}_g\right)^2}{2\mathcal{L}_g} \tag{4}$$

where L_p is the total length of spiral motion planning. However, the start and end points of the robot coverage path are different based on the two traditional methods, which cannot meet Requirement 5. The total path length should include the returning path towards the start point, which could be suboptimal under the two planning methods.

Lemma 1. *The length of returning path under zigzag planning in the workspace ($\mathcal{L}_{zR}$) is constrained as*

$$\mathcal{L}_s - \mathcal{L}_g \le \mathcal{L}_{zR} \le \sqrt{\left(\mathcal{L}_l - \mathcal{L}_g\right)^2 + \left(\mathcal{L}_s - \mathcal{L}_g\right)^2} \tag{5}$$

Proof. Since $\mathcal{L}_l \ge \mathcal{L}_s > \mathcal{L}_g$, we have $\mathcal{L}_s - \mathcal{L}_g < \sqrt{\left(\mathcal{L}_l - \mathcal{L}_g\right)^2 + \left(\mathcal{L}_s - \mathcal{L}_g\right)^2}$.

The equality holds on the left of Equation (5) when $\mathcal{L}_s = 2\times n\times\mathcal{L}_g$ for $n = 1, 2, 3, \ldots$. Then, the $\mathcal{L}_{zR} = \mathcal{L}_s - \mathcal{L}_g$.

The equality is satisfied on the right of Equation (5) when $\mathcal{L}_s = (2\times m - 1)\times\mathcal{L}_g$ for $m = 2, 3, 4, \ldots$. Then, the $\mathcal{L}_{zR}$ is

$$\mathcal{L}_{zR} = \sqrt{(\mathcal{L}_l - \mathcal{L}_g)^2 + (\mathcal{L}_s - \mathcal{L}_g)^2} \tag{6}$$

This completes the proof of Lemma 1. □

Lemma 2. *The length of returning path under the spiral planning in the workspace ($\mathcal{L}_{pR}$) is given*

$$\sqrt{(\frac{\mathcal{L}_s}{2})^2 + (\frac{\mathcal{L}_s - 2\mathcal{L}_g}{2})^2} \le \mathcal{L}_{pR} \le \sqrt{(\frac{\mathcal{L}_s - \mathcal{L}_g}{2})^2 + (\frac{2\mathcal{L}_l - \mathcal{L}_s + \mathcal{L}_g}{2})^2} \tag{7}$$

Proof. Since $\mathcal{L}_l \ge \mathcal{L}_s > \mathcal{L}_g$, $\left(\frac{L_s - 2L_g}{2}\right)^2 < \left(\frac{\mathcal{L}_s - \mathcal{L}_g}{2}\right)^2$ and $\left(\frac{\mathcal{L}_s}{2}\right)^2 < \left(\frac{2\mathcal{L}_l - \mathcal{L}_s + \mathcal{L}_g}{2}\right)^2$, we have $\sqrt{\left(\frac{\mathcal{L}_s}{2}\right)^2 + \left(\frac{\mathcal{L}_s - 2\mathcal{L}_g}{2}\right)^2}$ $< \sqrt{\left(\frac{\mathcal{L}_s - L_g}{2}\right)^2 + \left(\frac{2\mathcal{L}_l - \mathcal{L}_s + \mathcal{L}_g}{2}\right)^2}$.

The equality holds on the left of Equation (7) when $\mathcal{L}_s = 2\times n\times\mathcal{L}_g$ for $n = 1, 2, 3, \ldots$ Then, the $\mathcal{L}_{pR}$ is

$$\mathcal{L}_{pR} = \sqrt{\left(\frac{\mathcal{L}_s}{2}\right)^2 + \left(\frac{\mathcal{L}_s - 2\mathcal{L}_g}{2}\right)^2} \tag{8}$$

The equality holds on the right of Equation (7) when $\mathcal{L}_s = (2\times m - 1)\times\mathcal{L}_g$ for $m = 2, 3, 4, \ldots$

Then, the $\mathcal{L}_{pR}$ is

$$\mathcal{L}_{pR} = \sqrt{\left(\frac{\mathcal{L}_s - \mathcal{L}_g}{2}\right)^2 + \left(\frac{2\mathcal{L}_l - \mathcal{L}_s + \mathcal{L}_g}{2}\right)^2} \tag{9}$$

This completes the proof of Lemma 2. □

The robot follows the first two steps of spiral motion planning, then repeats the zigzag motion planning, and finally returns to the start point. The robot is assumed to run along the feeding and drinking lines without moving across them. The DCPP finally provides the robot with overall trajectories from the start to end points.

The total path length of DCPP ($\mathcal{L}_M$) is calculated through Equation (10):

$$\mathcal{L}_M = 2\times\left(\mathcal{L}_l + \mathcal{L}_s - 2\mathcal{L}_g\right) + \left(\mathcal{L}_l - 2\mathcal{L}_g\right)\times\frac{\mathcal{L}_s - 2\mathcal{L}_g}{\mathcal{L}_g} \tag{10}$$

The procedure of the proposed DCPP in a broiler barn is described in Algorithm 1. It is worth noting that the DCPP does not provide the robot with an actual coverage path, which could vary based on the IPP.

Algorithm 1: Directed coverage path planning procedure in a broiler barn

```
Initialize the left turn times τ = 0;
Initialize the next step state as null, 𝒮 = [];
Initialize the robot heading to the longer side of the barn;
while (the robot does not reach target position) do
    if (τ < 2) then
        if (no obstacle on the right) then
            Turn right and move forward;
        else if (no obstacle in the front) then
            Move forward;
        else if (no obstacle on the left) then
            Turn left and move forward;
            τ = τ + 1;
        end
    end
    if (τ ≥ 3 and the robot can move forward) then
        if (no obstacle in the front) then
            Set 𝒮 = [Move forward];
        else if (no obstacle on the left) then
            Set 𝒮 = [Turn left and move forward];
            Turn left;
        else if (no obstacle on the right) then
            Set 𝒮 = [Turn right and move forward];
            Turn right;
        end
        Perform 𝒮;
    end
end
```

3.3. Informative planning protocol

The informative planning protocol (IPP) further refines and optimizes the coverage path based on historical data on broiler mortality distribution in a broiler barn. In the general case, the IPP incorporates the multi-objective informative planning and uses DCPP and historical data to guide the robots to more frequently visit those places with a higher probability of broiler mortality appearance. This multi-objective optimization problem is stated in Equation (11).

$$\begin{aligned} \boldsymbol{m}^* &= \underset{\boldsymbol{m}\in\mathcal{M}}{\operatorname{argmax}} \left\{\mathfrak{D}(\boldsymbol{m}), \mathfrak{I}_1(\boldsymbol{m}), \mathfrak{I}_2(\boldsymbol{m}), \cdots, \mathfrak{I}_n(\boldsymbol{m})\right\}, \\ &\text{s.t. } \mathcal{C}_{\boldsymbol{m}} \le \mathcal{B} \end{aligned} \tag{11}$$

where $\boldsymbol{m}$ is a sequence of robot motion planning, $\boldsymbol{m}^*$ is the selected robot motion with maximum information gain, $\mathcal{M}$ is the list of possible robot motion sequences, $\mathcal{C}_{\boldsymbol{m}}$ is the cost budget, and $\mathcal{B}$ is a budget with regard to time, memory, energy, maximum iteration times, etc. $\mathfrak{I}_i(\boldsymbol{m}), i = 1, 2, ..., n$, represents the information gathered by the robot motions and n is the number of the information source in the grid[34]. $\mathfrak{D}(\boldsymbol{m})$ represents the information from planned DCPP directions.

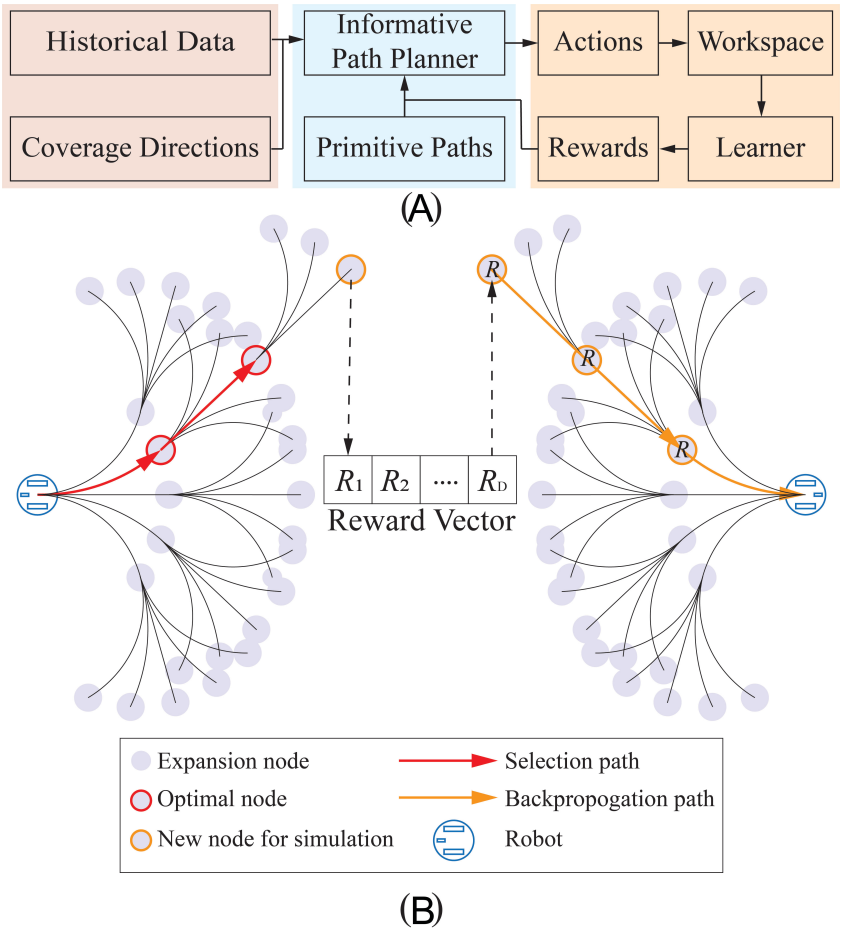

Figure 5. Illustration of the informative planning protocol (IPP): (A) general process of IPP; and (B) a specific example of IPP. The trees in (B) are mirrored for readable presentation, and the two robots are the same.

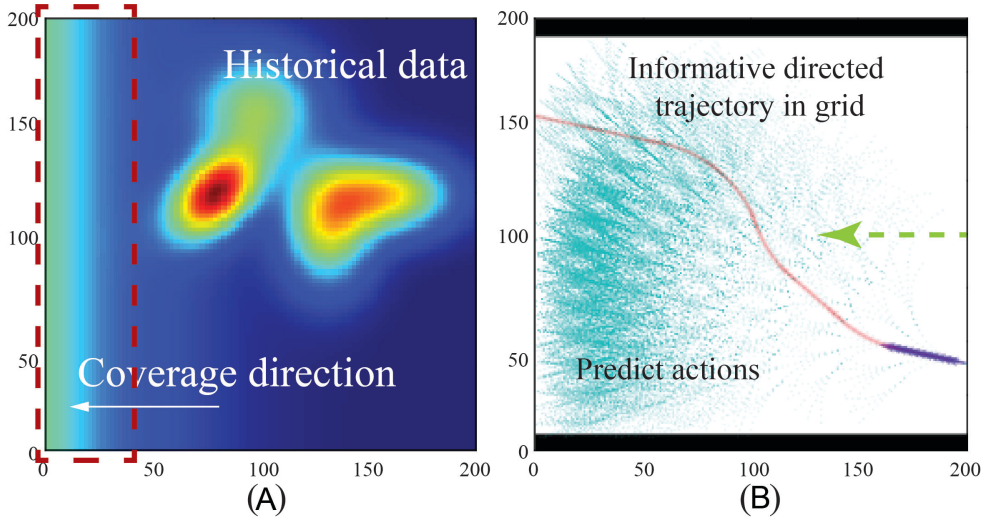

Figure 6. Illustration of the informative directed path planning in the grid, which performs target finding, i.e., where the dead broilers most likely exist: (A) heat map with historical data of dead broilers and DCPP direction information; and (B) the final planned informative directed trajectory in the grid.

The informative directed coverage path planning is shown in Figure 5. In Figure 5A, the planner weighs different objectives (e.g., rapidly covers the space as driven by DPCC or moves to the most likely area as driven by heat map) and optimizes the multi-objective problem to choose a preferred solution from a given set of optimal solutions. The preferred solution is then reflected as actions planned into the workspace, and the learner further improves it in a back-propagation direction. Finally, the most promising solution is determined based on rewards, and a mortality-based coverage path is constructed accordingly. A specific example of the IPP is depicted in Figure 5B. The major component is a primitive path which is built with robot kinematic constraints and divided into five sub-branches, each connected by two nodes. The path is constructed accumulatively during each iteration, and the most informative nodes are explored and selected first for the area with the highest probability of broiler mortality appearance. The rewards are only utilized in the selected nodes for optimization. The framework consists of selection, expansion, simulation, and back-propagation in each iteration. During selection, starting at the initial position, target nodes are recursively selected until an undependable node is encountered. During expansion, each expandable node is subdivided into five sub-branches. During simulation, the multiple-objective function is operated in each expandable node to gain a reward vector. Finally, during back-propagation, the rewards are backed up in each selected and expandable node.

Note that the information in this paper is defined by the broiler mortality historical data for the past 30 days. Since historical data as a priority map also have uncertainty, we utilize the Gaussian process (GP) to transform them into a continuous information map. The amounts of information in each grid can be varied with the number of dead broilers detected. To ensure the robot's path tends to the next planned grid, we set $\mathfrak{D}(\boldsymbol{m})$ as the average value of the current grid information at the adjacent edge, which proportionally decreases with the distance in the opposite direction of DCPP in the grid. More $\mathfrak{D}(\boldsymbol{m})$ information can be clearly found in the red dashed rectangle near the edge of the next grid [Figure 6A]. The planned path tends to be an optimized decision between the length and information gain along it, which might be conflicting in nature. Note that the IPP is only executed within each grid. The path obtained by DCPP becomes an information-oriented application in each grid, guiding the robot to the next grid. The resultant trajectory in the grid is shown in Figure 6B.

The time complexity depends on the Monte Carlo Tree Search (MCTS) tree depth and the steps of each simulation. Assume in an arbitrary iteration i, the tree depth is d_i. Then, the number of total actions is $O(d_i \times n_a)$, where n_a is the number of defined primitive actions. Assume each simulation process costs $O(S)$, which is a problem-dependent value (e.g., the steps of simulation are preset depending on the simulation time budget, considering that longer simulations are more accurate, while shorter simulations return a result more quickly). Then, the complexity for one search iteration is $O(d_i \times n_a + S)$. If we proceed N iterations, the complexity is $O(N(d_i \times n_a + S))$. For multiple objective computation, the complexity becomes $O(N(d_i \times n_a^2 + S))$ due to required extra computation in the MCTS selection step. For practical runtime assessment, a concrete example is when searching 1000 iterations with five available actions on a standard laptop, MCTS takes around 0.3 s and multi-objective MCTS (formally ParetoMCTS) needs about 1 s. With a better computer, the runtime should be even better. This suffices to make a real-time decision.

3.4. Target detection

The target detection is to localize dead birds in real-time processing[35,36]. The dead birds are detected by the YOLO V4 dead bird detector[28] [Figure 7]. The images are captured by the camera and input into the detector. The detector should first be well trained and developed in view of the captured images. Then, the trained YOLO V4 takes the acquired image as an input to convert it into a map with default grids. Predefined anchors are tiled onto each grid cell, and predictions of bounding boxes along with confidences and class names are made accordingly. With the non-maximum suppression rule, the bounding box with the highest confidence is retained for dead bird detection. Finally, the detection results, including indices, centroid coordinates, and

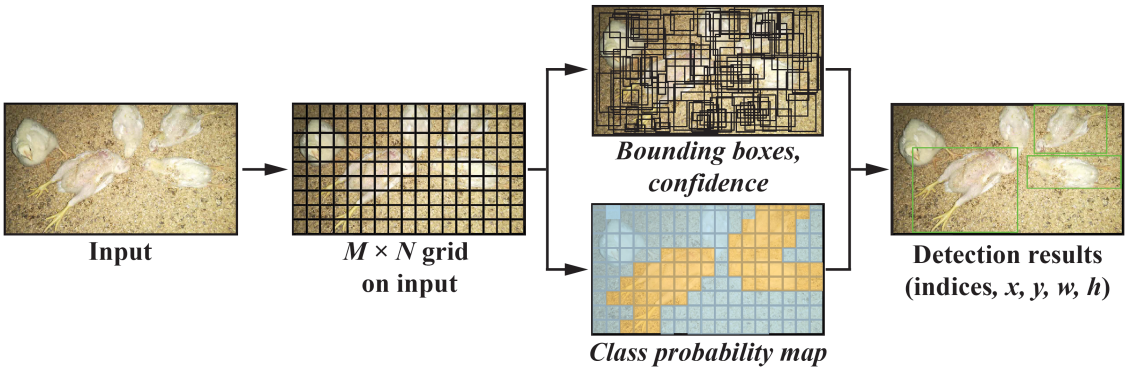

Figure 7. Network architecture of You Only Look Once (YOLO) V4 dead bird detector. Dead birds are enclosed with green bounding boxes.

width and height of bounding boxes, are utilized to pinpoint broiler mortality in each cell. Based on our previous testing, the YOLO V4 achieves on average 90% precision, recall, and F1 scores for detection, 4.8 mm root mean square error for localization, and 7 fps for processing speed when dealing with broiler mortality at various bird ages, light intensities, and bird body gestures. Therefore, it is suitable to serve our purpose of real-time detecting and localizing broiler mortality in this research.

The motivation for selecting the YOLO V4 is that it is a stable, mature, and efficient model and provides reliable and accurate detection results. The major function of this model serving part of the robotic navigation system is to localize dead birds. We also understand that there are more recent deep learning object detection models available, such as YOLO V7 that can be easily trained with custom datasets and replaces YOLO V4. The path planning for the removal robot is completed after the locations of broiler mortality are obtained in the coverage path.

3.5. Multi-target routing scheme

The dead broilers in the coverage path of a broiler barn are located as multiple targets collected by the removal robot. The robot should start from and return to the same point (entrance/exit gate of the barn), as addressed in Section 2.3. Meanwhile, multi-target path planning of the robot should have two major functions: obstacle avoidance and minimal travel distance regarding time and energy consumption. In those regards, multi-target path planning consists of two steps. The first step is point-to-point navigation, which generates the shortest collision-free path between target points. The second step is to navigate the robot to the targets in sequence, so as to minimize the total length of the trajectory.

To achieve the optimal visiting sequence of $\mathcal{N}$ targets, it is necessary to define the cost of path lengths between target points, that is, the shortest distance with obstacle avoidance between target points. Dijkstra's algorithm is utilized to minimize the length of point-to-point navigations. However, Dijkstra's algorithm needs to build a $\mathcal{N}_s \times \mathcal{N}_s$ adjacent matrix. The $\mathcal{N}_s$ is the total number of grids in a decomposed workspace (i.e., 456 for the current broiler barn) , resulting in highly expensive computation. Therefore, in light of the broiler layout, we design hub grids to reduce the computational effort. Note that the proposed hub-based multi-target routing (HMTR) scheme is applicable to all row-based environments for multi-target navigation, such as storage buildings, crops, power stations, *etc*.

The hub grid refers to the grid at the two ends of the feeding and drinking lines. For instance, in Figure 8, six hub grids are shown in the pink dashed line rectangle. It has the characteristics of unobstructed connection of targets in the corridor formed by the feeding and drinking lines, such as the hub grids connecting targets $\mathcal{T}_1$, $\mathcal{T}_2$, and $\mathcal{T}_3$ with no collision. It also features a collision-free connection to targets outside the corridor, such as the hub grid that can connect target $\mathcal{T}_4$ without collision. When the connecting lines between target

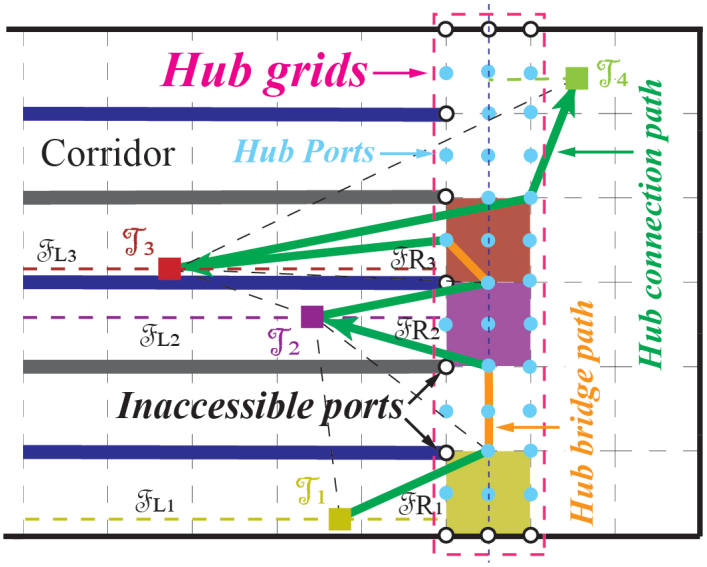

Figure 8. Example illustration of the HMTR scheme.

points are blocked by obstacles, as shown by the black dotted lines in Figure 8, the corresponding hub grids are initially obtained for connection. The selection of the corresponding hub grids to the targets i and j is made by the total distance. Let $\mathcal{F}_{Li}$ be the distance from the target point i to the centerline of the hub grid on the left side and $\mathcal{F}_{Ri}$ be the distance from the target point i to the centerline of the hub grid on the right side. If $(\mathcal{F}_{Li} + \mathcal{F}_{Lj}) > (\mathcal{F}_{Ri} + \mathcal{F}_{Rj})$, the hub grid on the right side is selected. If $(\mathcal{F}_{Li} + \mathcal{F}_{Lj}) \leq (\mathcal{F}_{Ri} + \mathcal{F}_{Rj})$, the hub grid on the left side is selected.

To further optimize the path selection, we decompose the hub grid into nine ports that can be connected. When the port is blocked by a feeding or drinking line, it is regarded as inaccessible. The total path length between target points i and j is $\mathfrak{L}_{ij}$, which is the addition of the length of the hub bridge path and the length of the hub connection path shown in Figure 8. Dijkstra's algorithm is utilized to minimize the length of point-to-point navigations. The trajectory is established between two points, which can be selected from each accessible port or the dead broilers. Each point is recursively connected with the other points, and the distances of connection lines passing through obstacles are assigned by an infinite number. As a result, point-to-point navigation with obstacles is excluded, and feasible solutions are retained. The shortest paths between each pair of points are selected from those feasible solutions. Each dead bird skips intermediate connections between adjacent grids and connect directly to the nearest port in the hub grid or to another dead bird, avoiding obstacles with the shortest traveling distance and improving computational efficiency.

The Miller–Tucker–Zemlin (MTZ) algorithm is then introduced for sequencing the navigation among the target points[37]. We define the connection variable as $\mathfrak{C}_{ij}$ and path lengths between target points i and j as $\mathfrak{L}_{ij}$. The objective function is then given by

$$\min \sum_{i} \sum_{j} \mathfrak{L}_{ij} \mathfrak{C}_{ij} \tag{12}$$

To ensure that the result is a valid tour, several constraints must be added [Equation (13)]

$$\begin{aligned} &\textstyle\sum_{i \in \mathcal{V}} \mathfrak{C}_{ij} = 1, \quad \forall j \in \mathcal{V}, i \neq j \\ &\textstyle\sum_{j \in \mathcal{V}} \mathfrak{C}_{ij} = 1, \quad \forall i \in \mathcal{V}, i \neq j \end{aligned} \tag{13}$$

where $\mathcal{V}$ is the set of number of target points. The first set of equalities is a go-to constraint, which requires that each target point is visited only once and is different from the others. The second set of equalities is a come-from constraint, which requires that the departure of each target point also occurs once and is different from the other ones.

Equations (12) and (13) may form multiple enclosed paths for all target points, with the formation of subtours. The MTZ constraints are utilized to eliminate unnecessary subtours and ensure a single enclosed path with the shortest length [Equation (14)]. Each visited node is labeled, resulting in the uniqueness of each visit.

$$\mathcal{U}_i + \mathfrak{C}_{ij} \leq \mathcal{U}_j + (n-1) \times \left(1 - \mathfrak{C}_{ij}\right) \quad 2 \leq j \leq n \tag{14}$$

where $\mathcal{U}$ is the sequence of each target point visited and n is the number of target points. When $\mathfrak{C}_{ij} = 1$, the equality holds ($\mathcal{U}_i + 1 = \mathcal{U}_j$).

Based on the MTZ algorithm, we finally obtain a visiting sequence of dead broilers. The robot with that sequence starts and ends at the gate of the broiler barn with the shortest collision-free paths.

Algorithm 2: Hub-based multi-target routing (HMTR) scheme

Load $\mathcal{N}$ obtained broiler locations as $\mathcal{T}_1, ..., \mathcal{T}_\mathcal{N}$ and robot initial location as $\mathcal{T}_0$.
Initialize the connection variable matrix $\mathfrak{C}$;
for $i = 0 : \mathcal{N}$ **do**
  for $j = 0 : \mathcal{N}$ **do**
    if $\mathcal{T}_i$ *can direct connect to* $\mathcal{T}_j$ **then**
      $\mathfrak{L}_{ij} = \sqrt{(x_{\mathcal{T}_i} - x_{\mathcal{T}_j})^2 + (y_{\mathcal{T}_i} - y_{\mathcal{T}_j})^2}$;
    else
      if $(\mathcal{F}_{Li} + \mathcal{F}_{Lj}) > (\mathcal{F}_{Ri} + \mathcal{F}_{Rj})$ **then**
        Select corresponding right-side hub grids;
      else
        Select corresponding left-side hub grids;
      end
      Select the best ports in the hub grids;
      Use Dijkstra algorithm to obtain $\mathfrak{L}_{ij}$
    end
  end
end
Use MTZ method to find the optimal visiting sequence.

4. SIMULATION AND COMPARATIVE STUDIES

Simulation and comparative studies were carried out to validate the effectiveness and efficiency of the proposed path planning methods of real-time autonomous mobile robots. The environments referred to are those in a typical broiler barn. The robot was parameterized as described in Section 2.1 based on commercialized poultry robots. These settings were taken to exemplify our proposed method and could be tailored according to specific applications.

Table 1. Comparison of path length and approximated travel time in broiler barn. The robot is assumed to have a linear velocity of 0.4 m/s

Models	Path length (m)	Approximated travel time (min)
Proposed model	1182	49
BCD	16,408	683

4.1. Path planning for the detection robot

The proposed DCPP was initially compared with the zigzag and spiral methods. The start and end points for the broiler mortality robot were the same for the three methods, and our proposed method did not have redundant return paths. The total path length of the three methods was 912 m for the proposed method, 920 m for the zigzag method, and 917 m for the spiral method, respectively. The overall path based on the DCPP is depicted in Figure 9B.

With the assistance of DCPP, IPP is shown in Figure 9A and C. The cases are executed between two feeding/drinking lines, indicated as black bars on the left and right of the figures. The robot accounts for the overall DCPP direction and historical dead bird distribution data depicted as heat maps with red color areas indicating a higher possibility of broiler mortality appearance. Cyan areas indicate multiple branches subdivided by IPP. A path indicated as a red line designates a maximal information gain. Once the robot meets a random obstacle (indicated as the black object in Figure 10), such as welfare enrichment (e.g., perches, straw bales, and pecking stones)[38], the information gain of IPP is optimized with the historical data and DCPP direction while avoiding the obstacle. Not only is the trajectory planned with previous data, but it is also updated with new data [Figure 11], resulting in a real-time efficient path for the robot. In Figure 11, the trajectory changes from roaming between two obstacles to roaming atop the upper obstacle after the broiler mortality distribution data are updated based on the YOLO V4 dead bird detection and localization.

Limited by the working environment in the broiler barn, it is assumed that the detection range of the robot is 50 cm and the linear speed is 0.4 m/s. Through the traditional CCPP algorithm, such as BCD method, the path length of the CCPP is 16,408 m, which requires approximately 683 min to complete. However, DCPP with IPP is fine-tuned on the basis of the information gained on the paths generated by DCPP. In light of various information distribution in different environments, the final generated global trajectory length in each grid is only 12%-37% longer than DCPP. The final path length of the DCPP with IPP is 1182 m, which requires approximately 49 min to complete. Compared with the traditional CCPP, our proposed algorithm has a shorter path length and the travel time also meets the demands of broiler barns. The final results are outlined in Table 1.

4.2. Path planning of the removal robot

With the AI-based advancement of sensing techniques, locations of broiler mortality are obtained in an overall trajectory for the second robot. The HMTR receives the mortality location information and generates a collision-free route to reach the targets in a reasonable and efficient sequence so that the total traveling distance is minimized. To validate the adaptability and efficiency of our algorithms in various number of targets, three datasets were selected for simulation and comparative studies[39]. In each dataset, we iteratively performed 30 executions to compute the mean and standard deviation of path length. Table 2 summarizes the qualitative comparison results between the features of our algorithm and state-of-art models, such as genetic algorithm (GA), particle swarm optimization (PSO), self-organizing maps (SOM), and imperialist competitive algorithm (ICA). The SOM algorithm is similar to a typical artificial neural network algorithm, except it utilizes a competitive learning process instead of back-propagation that utilizes gradient descent. The ICA algorithm is a biologically inspired algorithm, which simulates the social-political process of imperialism and

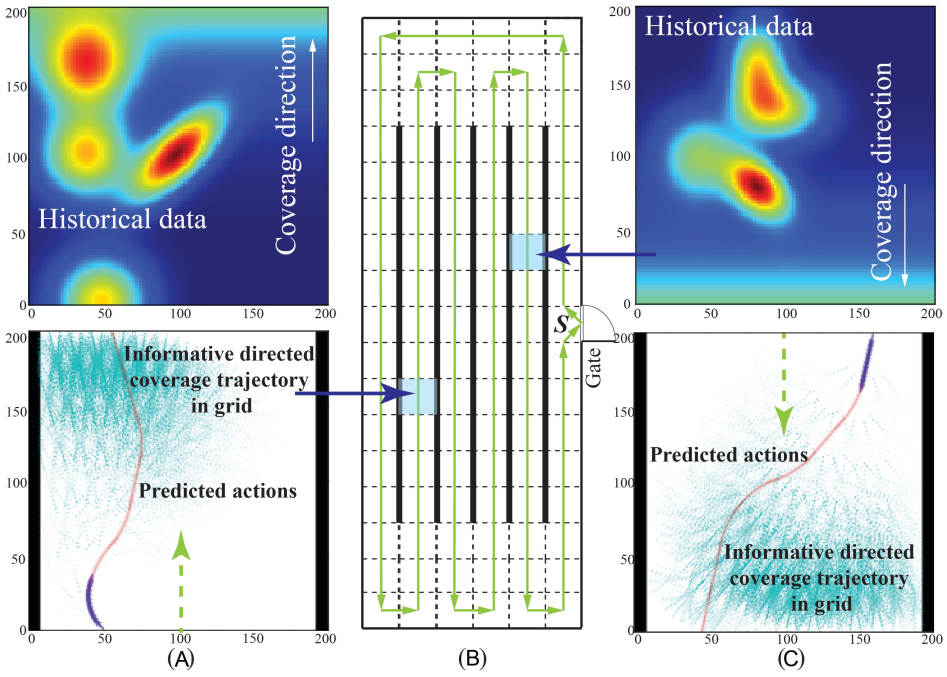

Figure 9. Illustration of robot global path planning in the tested workspace: (A and C) examples of informative trajectory between two feeding/drinking lines in various DCPP directions and historical dead bird distribution data; and (B) the overall DCPP trajectory.

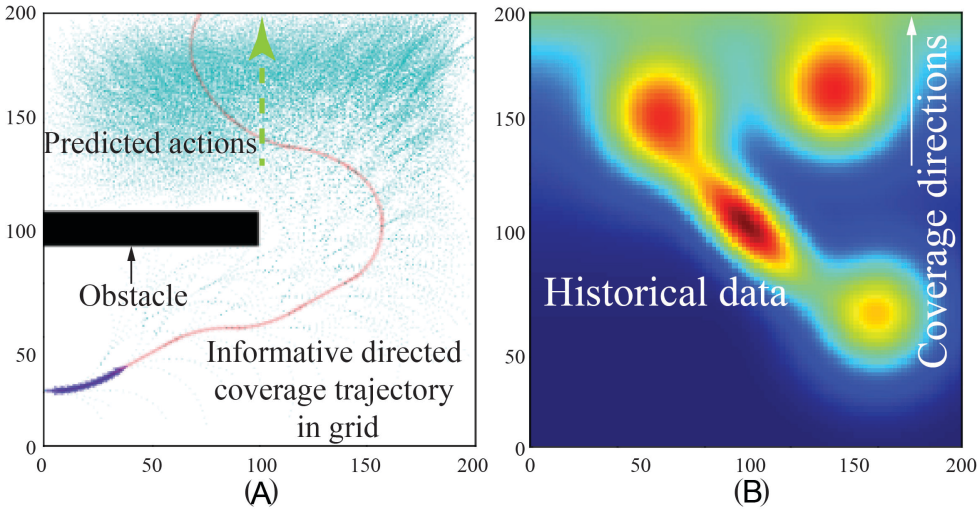

Figure 10. Informative planning protocol avoids a random obstacle in the grid: (A) the final planned informative directed coverage trajectory in grid; and (B) heat map with historical data of dead broilers and DCPP direction information.

imperialistic competition in humans.

Then, the reactive local navigator was utilized to generate real-time commands (e.g., acceleration, deceleration, and turning) for the robot arriving at a dead bird. Figure 12 shows three instances of grids for local navigation. Based on our simulation studies, using the dynamic window approach (DWA) local navigator, the robot successfully reached the existing dead birds and simultaneously avoided moving/still broilers. Robot running time and local trajectories could vary with grid locations, dead bird number in a grid, and distribution of live birds. As shown in Figure 12A, the two connected grids were between feeding and drinking lines surrounded

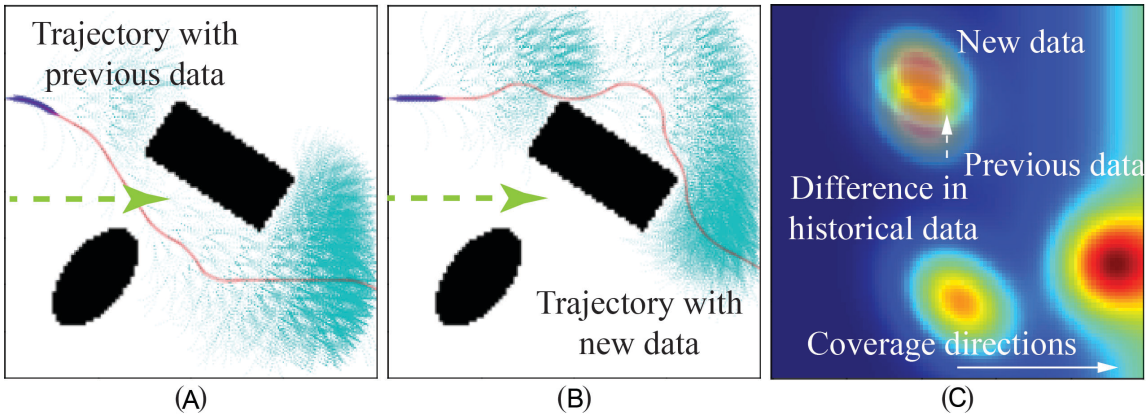

Figure 11. Different trajectories generated by updated historical data: (A) the planned trajectory with previous data; (B) the new planned trajectory with new data; and (C) heat map with different historical data.

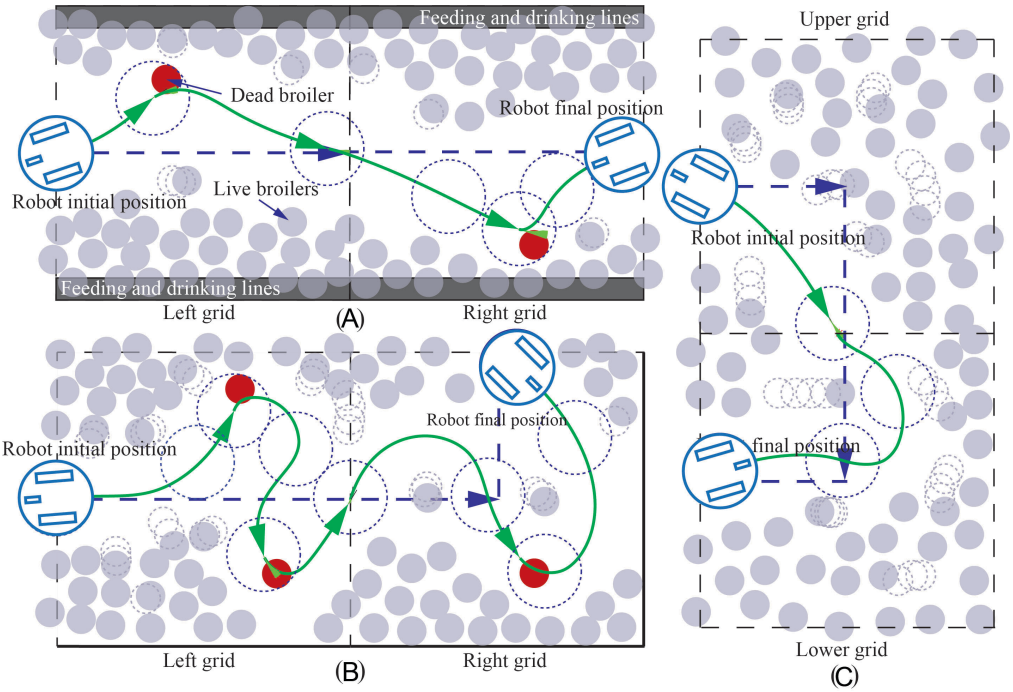

Figure 12. Illustration of robot local navigation at various locations: (A) sample of grids between feeding and drinking lines; (B) sample of grids at the corner; and (C) sample of grids for robot U-turning. Green lines represent the robot real motion trajectory, blue dashed lines represent trajectories generated by global path planning, navy blue solid circles are robot final positions in the figure, navy blue dashed circles illustrate different stages of robot positions, grey rectangles are feeding lines and drinking lines, red dots are dead broilers, and slate grey dots are live broilers.

by birds, which were the most common cases in broiler barns, and two dead birds were distributed separately in the two grids. The trajectory of the robot was relatively straightforward due to less blockage of moving birds, in which the running time was 22–24 s for the left grid and 24–26 s for the right grid. As shown in Figure 12B, the connected grids were at the corner of the barn with two dead birds in the left grid and one dead bird in the right grid, resulting in a running time of 56–58 s for the left grid and 34–36 s for the right grid. As shown in Figure 12C, the robot needed to make a U-turn between the two connected grids to complete the path. Even though no dead birds were detected in the grids, the the live birds could still interfere with the robot due to their random distribution and unpredictable movements. Therefore, the running time varied for the two grids:

Table 2. Comparison of minimum path length, average path length, and standard deviation (STD) of path length with other models. The values are reported for 30 executions

Test data set	Model	Min length (m)	Average length(m)	Length STD (m)
Bays29	GA	9.47e+03	9.98e+03	4.46e+03
	PSO	9.07e+03	9.25e+03	2.38e+03
	SOM	1.01E+04	1.28E+04	7.59E+03
	ICA	1.09E+04	1.22E+04	9.87E+03
	Proposed model	9.07e+03	9.07e+03	0
KroA200	GA	2.39e+05	2.57e+05	1.15e+04
	PSO	1.09e+05	1.17e+05	5.50e+03
	SOM	2.13E+05	2.60E+05	2.19E+04
	ICA	2.12E+05	2.60E+05	6.67E+03
	Proposed model	1.06e+05	1.06e+05	0
PA561	GA	1.37e+05	1.93e+05	6.30e+04
	PSO	1.11e+05	1.14e+05	1.60e+03
	SOM	1.01E+05	1.21E+05	1.84E+04
	ICA	1.48E+05	1.51E+05	2.43E+03
	Proposed model	1.03e+05	1.03e+05	0

12–14 s for the upper grid and 19–21 s for the lower grid. In a broiler barn, the cases shown in Figure 12A took up the most proportion (420 grids), within which most contained no dead broilers, and the average robot running time was 20–28 s in a single grid. Therefore, our proposed methods have a reasonable running time in commercial-scale poultry barns, and they would be beneficial for rapidly detecting and collecting broiler mortality. Simulation and comparison studies demonstrate the effectiveness and efficiency of the proposed real-time robot safety-aware navigation.

5. CONCLUSION

A robotic system for detecting and collecting dead broilers in a barn is a promising direction for solving the issue of broiler mortality removal. Aiming at this vision, we developed an informative planning protocol-based multi-layer robot navigation system through detection and removal robots. The detection robot consists of DCPP for constructing the overall trajectory; IPP for detailing the trajectory based on historical data, DCPP direction, and obstacles; and a YOLO V4 dead bird detector for providing the precise locations of broiler mortality along the trajectory. The removal robot receives the mortality location information and plans an optimal ordered route by the HMTR scheme. The comparison and simulation results demonstrate the great potential of the proposed methods for robot navigation, being useful tools for supporting precision broiler management.

There are also many possible avenues for future work. A challenging extension is that we will integrate our algorithm to test the robots in the real scene of the broiler barn and develop a suitable human–robot interaction platform for effective control. Another interesting topic is the application of multiple robots to cooperatively search the environment to reduce the overall work time and simultaneously complete the functions of search, identification, and removal to improve efficiency.

DECLARATIONS

Acknowledgments

The authors would like to thank the editor-in-chief, the associate editor, and the anonymous reviewers for their valuable comments.

Authors' contributions

Wrote and reviewed the manuscript: Lei T, Li G, Luo C, Zhang L, Liu L, Gates RS
All authors contributed equally.

Financial support and sponsorship
None.

Availability of data and materials
Not applicable.

Conflicts of interest
All authors declared that there are no conflicts of interest.

Ethical approval and consent to participate
Not applicable.

Consent for publication
Not applicable.

REFERENCES

1. United States Department of Agriculture NASS. Poultry-production and value 2020 summary; 2018. Available from: https://www.nass.usda.gov/Publications/Todays_Reports/reports/plva0421.pdf [Last accessed on 30 Aug 2022].
2. Tottori J, Yamaguchi R, Murakawa Y, Sato M, Uchida K, et al. The use of feed restriction for mortality control of chickens in broiler farms. *Avian Dis* 1997:433–37. DOI
3. Schwean-Lardner K, Fancher B, Gomis S, Van Kessel A, Dalal S, et al. Effect of day length on cause of mortality, leg health, and ocular health in broilers. *Poultry Sci* 2013;92:1–11. DOI
4. Astill J, Dara RA, Fraser ED, Roberts B, Sharif S. Smart poultry management: smart sensors, big data, and the internet of things. *Comput Electr Agricult* 2020;170:105291. DOI
5. Ren G, Lin T, Ying Y, Chowdhary G, Ting K. Agricultural robotics research applicable to poultry production: a review. *Comput Electr Agricult* 2020;169:105216.
6. Vroegindeweij BA, Blaauw SK, IJsselmuiden JM, van Henten EJ. Evaluation of the performance of PoultryBot, an autonomous mobile robotic platform for poultry houses. *Biosyst engineer* 2018;174:295–315. DOI
7. Li G, Chesser GD, Huang Y, Zhao Y, Purswell JL, et al. Development and optimization of a deep-learning-based egg collecting robot. *Trans ASABE* 2021:0. DOI
8. Liu L, Luo C, Shen F. Multi-agent formation control with target tracking and navigation. In: IEEE International Conference on Information and Automation (ICIA); 2017. pp. 98–103. DOI
9. Chen J, Luo C, Krishnan M, Paulik M, Tang Y. An enhanced dynamic delaunay triangulation-based path planning algorithm for autonomous mobile robot navigation. In: Intelligent Robots and Computer Vision XXVII: Algorithms and Techniques. vol. 7539. SPIE; 2010. pp. 253–64. DOI
10. Zhao W, Lun R, Gordon C, Fofana AB, Espy DD, et al. A privacy-aware Kinect-based system for healthcare professionals. In: IEEE International Conference on Electro Information Technology (EIT); 2016. pp. 0205–10. DOI
11. Lei T, Luo C, Ball JE, Rahimi S. A graph-based ant-like approach to optimal path planning. In: *IEEE Congr Evol Comput (CEC)*. IEEE; 2020. pp. 1–6. DOI
12. Lei T, Luo C, Jan GE, Fung K. Variable speed robot navigation by an ACO approach. In: International Conference on Swarm Intelligence. Springer; 2019. pp. 232–42. DOI
13. Wang L, Luo C, Li M, Cai J. Trajectory planning of an autonomous mobile robot by evolving ant colony system. *Int J Robot Autom* 2017;32:406–13. https://www.researchgate.net/profile/Chaomin-Luo/publication/319032211_Trajectory_planning_of_an_autonomous_mobile_robot_by_evolving_ant_colony_system/links/5997a952458515644325892e/Trajectory-planning-of-an-autonomous-mobile-robot-by-evolving-ant-colony-system.pdf [Last accessed on 30 Aug 2022].
14. Lei T, Luo C, Ball JE, Bi Z. A hybrid fireworks algorithm to navigation and mapping. In: Handbook of Research on Fireworks Algorithms and Swarm Intelligence. IGI Global; 2020. pp. 213–32. DOI
15. Lei T, Luo C, Sellers T, Rahimi S. A bat-pigeon algorithm to crack detection-enabled autonomous vehicle navigation and mapping. *Intell Syst Applic* 2021;12:200053. DOI
16. Wang J, Meng MQH. Optimal path planning using generalized Voronoi graph and multiple potential functions. *IEEE Trans Industr Electron* 2020;67:10621–30. DOI
17. Yang SX, Luo C. A neural network approach to complete coverage path planning. *IEEE Trans Syst, Man, Cybern, Part B (Cybernetics)* 2004;34:718–24. DOI

18. Luo C, Yang SX, Krishnan M, Paulik M. An effective vector-driven biologically-motivated neural network algorithm to real-time autonomous robot navigation. In: IEEE International Conference on Robotics and Automation (ICRA); 2014. pp. 4094–99. DOI
19. Zhu D, Tian C, Jiang X, Luo C. Multi-AUVs cooperative complete coverage path planning based on GBNN algorithm. In: 29th Chinese Control and Decision Conference (CCDC); 2017. pp. 6761–66. DOI
20. Lei T, Sellers T, Rahimi S, Cheng S, Luo C. A nature-inspired algorithm to adaptively safe navigation of a Covid-19 disinfection robot. In: International Conference on Intelligent Robotics and Applications. Springer; 2021. pp. 123–34. DOI
21. Luo C, Gao J, Murphey YL, Jan GE. A computationally efficient neural dynamics approach to trajectory planning of an intelligent vehicle. In: 2014 International Joint Conference on Neural Networks (IJCNN). IEEE; 2014. pp. 934–39. DOI
22. Luo C, Yang SX. A bioinspired neural network for real-time concurrent map building and complete coverage robot navigation in unknown environments. *IEEE Trans Neural Netw* 2008;19:1279–98. DOI
23. Acar EU, Choset H. Sensor-based coverage of unknown environments: Incremental construction of morse decompositions. *Int J Robot Res* 2002;21:345–66. DOI
24. Nasirian B, Mehrandezh M, Janabi-Sharifi F. Efficient coverage path planning for mobile disinfecting robots using graph-based representation of environment. *Front Robot AI* 2021;8:4. DOI
25. Lei T, Luo C, Jan G, Bi Z. Deep learning-based complete coverage path planning with re-joint and obstacle fusion paradigm. *Front Robot AI* 2022. DOI
26. Li G, Hui X, Lin F, Zhao Y. Developing and evaluating poultry preening behavior detectors via mask region-based convolutional neural network. *Animals* 2020;10:1762. DOI
27. Li G, Xu Y, Zhao Y, Du Q, Huang Y. Evaluating convolutional neural networks for cage-free floor egg detection. *Sensors* 2020;20:332. DOI
28. Bochkovskiy A, Wang CY, Liao HYM. Yolov4: optimal speed and accuracy of object detection. *arXiv preprint arXiv:200410934* 2020. DOI
29. Tabler G, Berry I, Xin H, Barton T. Spatial distribution of death losses in broiler flocks. *J appl poultry res* 2002;11:388–96. DOI
30. Li G, Ji B, Li B, Shi Z, Zhao Y, et al. Assessment of layer pullet drinking behaviors under selectable light colors using convolutional neural network. *Comput Electr Agricult* 2020;172:105333. DOI
31. Lei T, Luo C, Sellers T, Wang Y, Liu L. Multi-task allocation framework with spatial dislocation collision avoidance for multiple aerial robots. *IEEE Trans Aerosp Electr Syst* 2022. DOI
32. United States Department of Agriculture NASS. Agricultural resource management survey (ARMS) of the U.S. broiler industry; 2011. https://www.nass.usda.gov/Surveys/Guide_to_NASS_Surveys/Ag_Resource_Management/ARMS_Broiler_Factsheet/Poultry%20Results%20-%20Fact%20Sheet.pdf[Lastaccessedon30Aug2022].
33. Mendeş M. Growth curves for body weight and some body measurement of Ross 308 broiler chickens. *J Appli Animal Res* 2009;36:85–88. DOI
34. Chen W, Liu L. Pareto Monte Carlo tree search for multi-objective informative planning. *arXiv preprint arXiv:211101825* 2021. DOI
35. Yang Y, Deng Q, Shen F, Zhao J, Luo C. A shapelet learning method for time series classification. In: IEEE 28th International Conference on Tools with Artificial Intelligence (ICTAI); 2016. pp. 423–30. DOI
36. Xing Y, Shen F, Luo C, Zhao J. L3-SVM: a lifelong learning method for SVM. In: 2015 international joint conference on neural networks (IJCNN). IEEE; 2015. pp. 1–8. DOI
37. Integer programming formulation of traveling salesman problems. *J ACM (JACM)* 1960;7:326–29. DOI
38. Bergmann S, Schwarzer A, Wilutzky K, Louton H, Bachmeier J, et al. Behavior as welfare indicator for the rearing of broilers in an enriched husbandry environment—a field study. *J Veterin Behav* 2017;19:90–101. https://www.sciencedirect.com/science/article/pii/S1558787816301915 [Last accessed on 30 Aug 2022].
39. Bixby B, Reinelt G. Traveling salesman problem library; 2022. http://elib.zib.de/pub/mp-testdata/tsp/tsplib/tsp/index.html [Last accessed on 30 Aug 2022].

Sellers *et al*. *Intell Robot* 2022;2(4):333-54
DOI: 10.20517/ir.2022.21

Intelligence & Robotics

Research Article

Open Access

A node selection algorithm to graph-based multi-waypoint optimization navigation and mapping

Timothy Sellers[1], Tingjun Lei[1], Chaomin Luo[1], Gene Eu Jan[2], Junfeng Ma[3]

[1]Department of Electrical and Computer Engineering, Mississippi State University, Mississippi State, MS 39759, USA.
[2]Department of Electrical Engineering, National Taipei University and Tainan National University of the Arts, Taipei 72045, Taiwan.
[3]Department of Industrial and Systems Engineering, Mississippi State University, Mississippi State, MS 39759, USA.

Correspondence to: Prof. Chaomin Luo, Department of Electrical and Computer Engineering, Mississippi State University, 406 Hardy Road, Mississippi State, MS 39762, USA. E-mail: Chaomin.Luo@ece.msstate.edu; ORCID: 0000-0002-7578-3631

How to cite this article: Sellers T, Lei T, Luo C, Jan GE, Ma J. A node selection algorithm to graph-based multi-waypoint optimization navigation and mapping. *Intell Robot* 2022;2(4):333-54. http://dx.doi.org/10.20517/ir.2022.21

Received: 20 Jul 2022 **First Decision:** 12 Aug 2022 **Revised:** 18 Aug 2022 **Accepted:** 25 Aug 2022 **Published:** 12 Oct 2022

Academic Editor: Simon X. Yang **Copy Editor:** Jia-Xin Zhang **Production Editor:** Jia-Xin Zhang

Abstract

Autonomous robot multi-waypoint navigation and mapping have been demanded in many real-world applications found in search and rescue (SAR), environmental exploration, and disaster response. Many solutions to this issue have been discovered via graph-based methods in need of switching the robot's trajectory between the nodes and edges within the graph to create a trajectory for waypoint-to-waypoint navigation. However, studies of how waypoints are locally bridged to nodes or edges on the graphs have not been adequately undertaken. In this paper, an adjacent node selection (ANS) algorithm is developed to implement such a protocol to build up regional path from waypoints to nearest nodes or edges on the graph. We propose this node selection algorithm along with the generalized Voronoi diagram (GVD) and Improved Particle Swarm Optimization (IPSO) algorithm as well as a local navigator to solve the safety-aware concurrent graph-based multi-waypoint navigation and mapping problem. Firstly, GVD is used to form a Voronoi diagram in an obstacle populated environment to construct safety-aware routes. Secondly, the sequence of multiple waypoints is created by the IPSO algorithm to minimize the total travelling cost. Thirdly, while the robot attempts to visit multiple waypoints, it traverses along the edges of the GVD to plan a collision-free trajectory. The regional path from waypoints to the nearest nodes or edges needs to be created to join the trajectory by the proposed ANS algorithm. Finally, a sensor-based histogram local reactive navigator is adopted for moving obstacle avoidance while local maps are constructed as the robot moves. An improved $\mathcal{B}$-spline curve-based smooth scheme is adopted that further refines the trajectory and enables the robot to be navigated smoothly. Simulation and comparison studies validate the effectiveness and robustness of the proposed model.

Keywords: Adjacent node selection (ANS) algorithm, safety-aware roads, path planning, multiple-waypoint optimization, navigation and mapping

1. INTRODUCTION

Robotics system has been applied to numerous fields, such as transportation[1], healthcare service[2,3], agriculture[4], manufacturing[5], *etc.*, in recent years. Robot navigation is one of the fundamental components in robotic systems, which includes multi-waypoint navigation system[6–8]. As an increasing demand and limited onboard resources for autonomous robots, it requires the ability to visit several targets in one mission to optimize multiple objectives, including time, robot travel distance minimization, and spatial optimization[9–15]. For example, due to a global pandemic, the world struggled to sanitize heavily populated areas, such as airports, hospitals, and educational buildings. Autonomous robots with multi-waypoint navigation systems can effectively sanitize all targeted areas without endangering the workers[14,16]. As well as in agriculture management, multi-waypoint strategies allow the robotic system to navigate and survey multiple areas to assist in production and collection.

In order to employ robotic systems in real-world scenarios, one critical factor is to develop autonomous robot multi-waypoint navigation and mapping system[17]. In order to solve the autonomous robot navigation problem, countless algorithms have been developed, such as graph-based[18,19], ant colony optimization (ACO)[20–22], bat-pigeon algorithm (BPA)[23], neural networks[24–26], fuzzy logic[27], artificial potential field (APF)[28], sampling-based strategy[14,29], hybrid algorithms[30], task planning algorithm[31], *etc.* Chen *et al.* produced a hybrid graph-based reinforcement learning architecture to develop a method for robot navigation in crowds[18]. Luo *et al.* proposed an improved vehicle navigation method, which utilizes a heading-enabled ACO algorithm to improve trajectory towards the target[20]. Lei *et al.* developed a Bat-Pigeon algorithm with the ability to adjust the speed navigation of autonomous vehicles[23]. Luo *et al.* developed the model for multiple robots complete coverage navigation while using a bio-inspired neural network to dynamically avoid obstacles[32]. Na and Oh established a hybrid control system for autonomous mobile robot navigation that utilizes a neural network for environment classification and behavior-based control method to mimic the human steering commands[25]. Lazreg and Benamrane[27] developed a neuro-fuzzy inference system associated with a Particle Swarm Optimization (PSO) method for robot path planning using a variety of sensors to control the speed and position of a robot. Jensen-Nau *et al.*[28] integrated a Voronoi-based path generation algorithm and an artificial potential field path planning method, in which the latter is capable of establishing a path in an unknown environment in real-time for robot path planning and obstacle avoidance. Penicka and Scaramuzza[14] developed a sampling-based multi-waypoint minimum-time path planning model that allows obstacle avoidance in cluttered environments. Ortiz and Yu[30] proposed a sliding control method in combination with simultaneous localization and mapping (SLAM) method to overcome the bounded uncertainties problem, which utilizes a genetic algorithm to improve path planning capabilities. Bernardo *et al.* proposed a task planning method for home environment ontology to translate tasks given by other robots or humans into feasible tasks for another robot agent[31].

In robotic path planning, one of the special topics is autonomous robot multi-waypoint navigation which has been studied for many years. For instance, Shair *et al.* proposed a model for real-world waypoint navigation using a variety of sensors for accurate environmental analysis[33]. The system is designed utilizing the wide area augmentation system (WAAS) and the European geostationary navigation overlay service (EGNOS) for GPS in combination with aerial images to provide valuable positioning data to the system. Yang[34] brought about a multi-waypoint navigation system based on terrestrial signals of opportunity (SOPs) transmitters, which has the ability to operate in environments that are not available to global navigation satellite systems (GNSS) for unmanned aerial vehicles (UAV). Janoš *et al.* proposed a sampling-based multi-waypoint path planner, space-

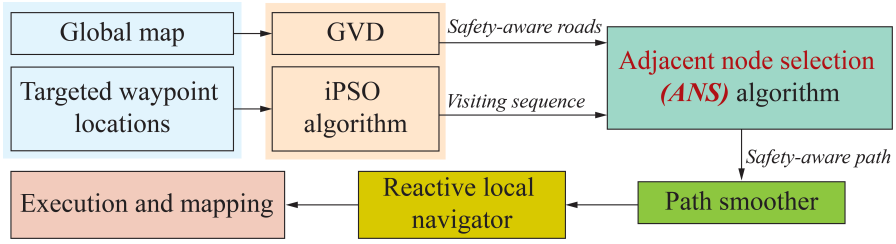

Figure 1. Illustration of the proposed model framework.

filling forest method to solve the problem of finding collision-free trajectories while the sequence of waypoints is formed by multiple trees[29]. However, the aforementioned approaches have not taken into account the safety of the robot during navigation. In real-world applications, an autonomous vehicle has odometry errors during operation. The safety-aware road model is developed utilizing the Generalized Voronoi diagram (GVD) approach. Once the safety-aware roads are defined, a particle swarm optimization (PSO) algorithm-based multi-waypoint path planning algorithm is proposed to visit each waypoint in an explicated sequence while simultaneously avoiding obstacles. In this paper, the Adjacent Node Selection (ANS) algorithm is developed to select the closest nodes on the safety-aware roads to generate the final collision-free trajectories with minimal distance. Furthermore, in our hybrid algorithm, we utilize a histogram-based reactive local navigator to avoid dynamic and unknown obstacles within the workspace. Through all of these methods, an effective and efficient safety-aware multiple waypoint navigation model was established, which has been validated by both simulations and comparison studies.

This paper proposes an Adjacent Node Selection (ANS) algorithm for obtaining an optimal access node into graph-based maps. To the best of our knowledge, there are no known similar algorithms that improve the paths created from the waypoint to the graph. The ANS algorithm can be applied to any graph-based mapping environment, which improves the various graph-based models used for autonomous robotic path planning systems. In finding an access point into the graph utilizing one of the nodes in the system, the ANS algorithm conducts point-to-point selection in dense obstacle field of environments to obtain a node to gain access to the graph that forms a resumable path from a waypoint to the graph. The algorithm's overall goal is to find a node in a graph-based map and shorten the overall path length from each waypoint to waypoint, and the waypoint to the graph.

One can see in Figure 1 the overall framework of our proposed model. Initially, the model is provided with a global map of its environment and the location of each target waypoint. The GVD utilizes the global map to construct the safety-aware roads, which are used to guide the robot throughout the environment. The targeted waypoint locations are used as input to the improved PSO (IPSO) algorithm that act as our waypoint sequencing module, which is utilized to find a near-optimal sequence to visit each waypoint. The ANS algorithm utilizes the output from the previous stages. The ANS algorithm finds the best node for each waypoint to use as an access point to the graph. If there is no direct path from one waypoint to a node in the graph, the algorithm conduces point-to-point navigation with nodes within a specified range, which will be explained in later sections of the paper. Once each waypoint has found its access point, the safety-aware path is constructed, which is then applied to our path smoothing algorithm. Finally, we utilize a reactive local navigation system to detect obstacles autonomously and simultaneously build a map of the environment along the generated path.

The main contributions of this paper with this framework of concurrent multi-waypoint navigation and mapping with collision avoidance as are summarized as follows: (1) An adjacent node selection (ANS) algorithm is proposed to build up regional bridges from waypoints to nodes or edges on the graph in multi-waypoint navigation and mapping; (2) a concurrent multi-waypoint navigation and mapping framework of an autonomous robot is developed by the generalized Voronoi diagram (GVD) and IPSO algorithm as well as a local navigator;

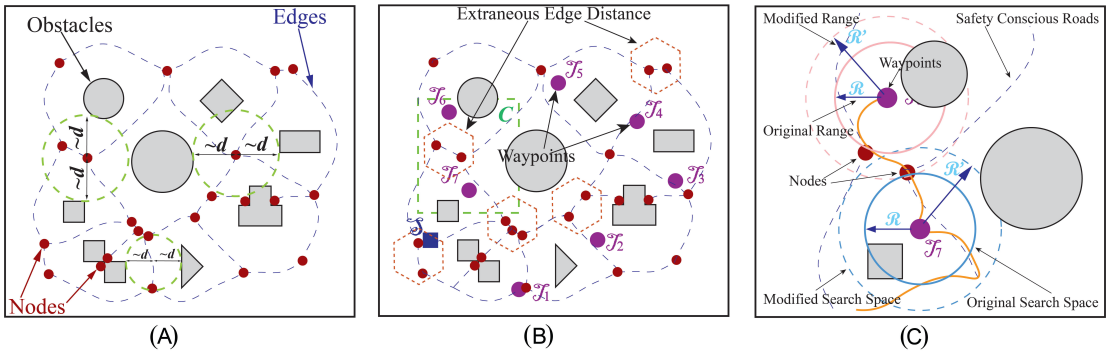

Figure 2. Illustration of the ANS algorithm and the safety-aware model by creation of the GVD. (A) Depicts the equidistance property of the nodes and edges in the GVD model. (B) illustrates how we remove extraneous edge distances, which are small edges within the graph that reduce the search space or range in the ANS algorithm. (C) illustrates how the removal of those extraneous edges improves the range and how an access node to the graph can be found.

(3) a GVD method is employed to plan safety-aware trajectories in an obstacle populated environment, while the sequence of multiple waypoints is created by the IPSO algorithm to minimize the total distance cost; (4) a sensor-based histogram robot reactive navigator coupled with map building is adopted for moving obstacle avoidance and local mapping. An improved $\mathcal{B}$-spline curve-based speed modulation module is adopted for smoother navigation.

The structure of this paper is as follows. Section II presents the safety-aware model that constructs the safety-conscious roads for robot traversal. Section III describes the proposed adjacent node selection algorithm to find an access node into the graph-based map. Section IV, the improved PSO-based (IPSO) multi-waypoint navigation model for waypoint sequencing is explained. Section V illustrates the reactive local navigator for real-time workspace building and obstacle avoidance. Section VI depicts simulation results and comparative analyses. Several important properties of the proposed framework are summarized in Section VII.

2. SAFETY-AWARE MODEL

Computational geometry has exceedingly studied the Voronoi diagrams (VD) model, which is an elemental data structure used as a minimizing diagram of a finite set of continuous functions[28,35]. The minimized function defines the distantance to an object within the workspace. The VD model decomposes the workspace into several regions, each consisting of the points near a given object than the others. Let $\mathcal{G} = \{g_1 \cdots, g_n\}$ be a set of points of $\mathbb{R}^d$ to each g_i associated with a specific Voronoi region $V(g_i)$. This can be expressed by the following equation[36,37]:

$$V(g_i) = \{x \in \mathbb{R}^d : \|x - g_i\| \leq \|x - g_j\|, \forall j \leq n\} \quad (1)$$

The intersection of $n-1$ half spaces can be denoted by the region $V(g_i)$. Each half space holds a point g_i along with another point of $\mathcal{G}$. The regions $V(g_i)$ are convex polyhedrons due to the bisectors acting as hyperplanes between each region. The generalized Voronoi diagram (GVD) is a modified version of the VD model defined as the set of points Euclidean distance from two obstacles[37]. The workspace is represented as a graph by the GVD model consisting of nodes, edges, and vertices[28].

The proposed ANS algorithm utilizes nodes and edges obtained from the GVD illustrated in Figure 2A. The nodes in the GVD act as junctions to connect waypoints, whereas the edges are used to determine the search range in view of waypoints. Solely the nodes in the search range are calculated, other than the entire workspace, thus reducing the computational expense. Figure 2B reveals that the range of some edges fails to evaluate how spare of the workspace is configurated. These edges with short lengths are distractors for evaluating and computing the search range, thus need to be eliminated shown in Figure 2B. In our ANS algorithm, those

edges with the shortest 10% are eliminated, while the rest of the edges are averaged to compute the radius of the search range. One circumstance is exhibited in Figure 2C, in which some nodes fail to fall into the search range once the excessively short edges are excluded. The original search space in solid circles and modified search space in dashed circles based on the ANS algorithm are shown in Figure 2C. As may be seen, after excessively short edges are effectively eliminated, an appropriate search range is achieved.

GVD nodes form the Euclidean distance between two or more obstacles, while the edges are the junction of two nodes that depict the distance between each neighboring node to another. Vertices are the connection points between three or more nodes. Using these features from the GVD model, an obstacle-free path with our safety-aware model is effectively created. The safety-aware model is constructed by inputting an image and extracting all significant features from the image, thus allowing the model to construct a map from the input image. The safety-aware roads are the clearest path between obstacles that occupy the available space in the map , which can be seen in Figure 2.

In this paper, in order to explain our proposed ANS algorithm, how the nodes are determined and constructed with the GVD will be presented in some detail. We will introduce some definitions and notations. Lee and Drysdale[36] derive four basic definitions for determining the optimal placement of edges and nodes within the GVD graph.

DEFINITION 1. A closed line segment M consists of two endpoints α and γ. A straight line is denoted by (α, γ), which is also known as an open segment. Elements within the derivation are referred to as points or segments. The straight line containing M is denoted by $\overleftrightarrow{M}$. The same line directed from α to γ is denoted by $\vec{M}$.

DEFINITION 2. The projection $\sigma(\epsilon, M)$ of a point q onto a closed segment M, is the intersection of $\overleftrightarrow{M}$ and is perpendicular to M and passing through ϵ.

DEFINITION 3. The distance between $\omega(\epsilon, M)$ is a point ϵ and a closed segment M in the Euclidean metric is defined as the distance $\omega(\epsilon, \sigma(\epsilon, M))$ between the point ϵ and its projection onto M if $\sigma(\epsilon, M))$ belongs to M and is min $(\omega(\epsilon, \alpha), \omega(\epsilon, \gamma))$ otherwise. In other words, $\omega(\epsilon, M) = \min_{u \in M}(\epsilon, u)$. The point of M, which is closest to ϵ, is called the image $I(\epsilon, M)$ of ϵ on M.

DEFINITION 4. The bisector $\beta(c_i, c_j)$ of two elements c_i and c_j is the locus of points equidistant from c_i and c_j. The bisector $\beta(Z, Q)$ of two sets of elements Z and Q is defined to be the locus of points equidistant from Z and Q, where the distance $\omega(\epsilon, Z)$ between a point ϵ and a set of elements Z is defined to be $\min_{c \in Z} \omega(\epsilon, c)$. The bisector $\beta(c_i, c_j)$ is said to be oriented if a direction is imposed upon it so that elements c_i and c_j lie to the left and the right of it, respectively. An oriented bisector $\beta(Z, Q)$ is defined similarly.

Utilizing these four definitions, we can easily establish edges among spaces or obstacles, which uses the equidistant to create an optimal edge that lies directly between the two spaces. As seen in the above definitions, we can also create edges between irregular-shaped spaces and obstacles.

To characterize the GVD, we expect the robot to be operated at a point within the workspace, a W, which is populated by convex obstacles $C_1, ..., C_n$. Non-convex obstacles are displayed as the union of convex shapes. The distance between a point and an obstacle is the minimal distance between the point and all points of the obstacle. The distance function, and its "gradient" are represented as:

$$d_i(x) = min_{c_0 \in C_i} \|x - c_0\| \tag{2}$$

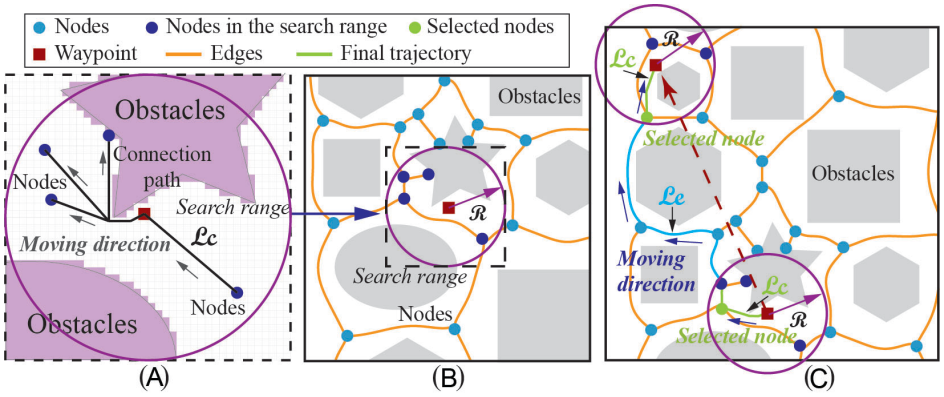

Figure 3. Details of the Adjacent Node Selection (ANS) algorithm. (A) The IPSO-based connection path planning in the search range. (B) The search range determination and node selection inside. (C) The final generated path with the minimum path length.

$$\nabla d_i(x) = \frac{x - c_0}{\|x - c_0\|} \tag{3}$$

where in Equation (2) d_i is the distance to obstacle C_i from a point x, and in Equation (3) $\nabla d_i(x)$ is the unit vector in the direction from x to c_0, where c_0 is the closest point to x in C_i. The essential structure block of the GVD is the arrangement of points equidistant to two sets C_i and C_j, with the end goal that each set in this set is the minimal distance to the obstacles C_i and C_j than other obstacles. This type of structure is known as the two-equidistant face,

$$f(i,j) = \begin{cases} x \in \mathbb{R}^m : 0 \le d_i(x) = d_h(x) \\ \forall d_i \ne i, j \\ \nabla d_i(x) \ne \nabla d_j(x) \end{cases} \tag{4}$$

Each face has a co-dimension in the ambient space, which causes the two-equidistant faces to be seen as one-dimensional. The intersection of both faces forms the GVD and is denoted by the following equation:

$$GVD = \bigcup_{i=1}^{n-1} \bigcup_{j=i+1}^{n} f(i,j) \tag{5}$$

3. ADJACENT NODE SELECTION ALGORITHM

The details of the adjacent node selection algorithm are shown in Figure 3. Within the search range obtained, we applyIPSO-based path planning algorithm to generate the connection path from the waypoint to all the potential nodes in the range. The connection path is planned in the grid-based map as shown in Figure 3A. The search range in the larger map is shown in Figure 3B, which is also a part of Figure 6. Finally, with the formation of a collision-free path to the adjacent nodes from the two waypoints, we obtain the optimal path selection by calculating the overall path length $\mathcal{L}_c + \mathcal{L}_e$.

To show the necessity of IPSO-based path planning from waypoints to adjacent nodes, a more specific scenario is shown in Figure 4. In Figure 4A, all straight lines connecting nodes and waypoints are separated by obstacles. Among them, points i and point j are located in our search range. If we only rely on the Euclidean distance between node and waypoint, it can be found that the point i is closer to the waypoint. However, after considering the path with obstacle avoidance, the path for point i to the waypoint is longer. To sum up, the obtained search range with ANS algorithm and the IPSO-based path planning algorithm can reduce the computational cost while ensuring a short and safe trajectory. The details of the procedure are described in Algorithm 2.

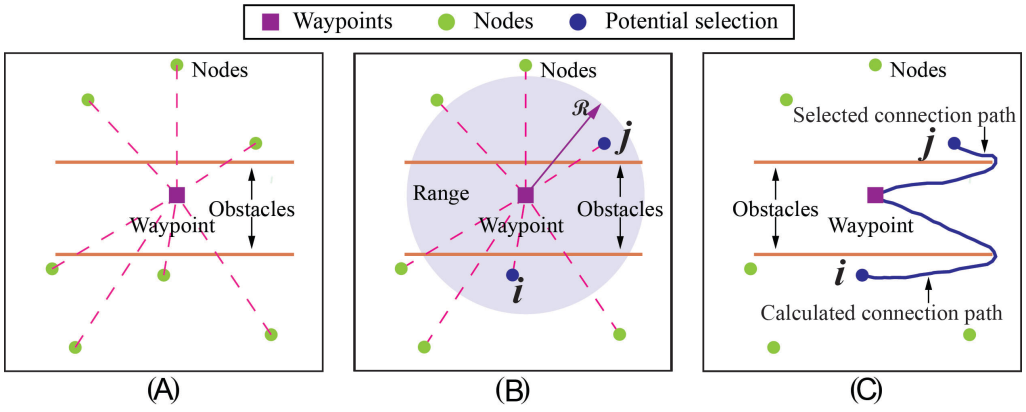

Figure 4. Illustration of ANS method within a more specific sense, where an obstacle obstructing the connection path. (A) The multiple connection paths have been obstructed by the obstacles. (B) It selects the nodes in the defined range. (C) It conducts IPSO point-to-point algorithm to achieve the optimal path to the selected node.

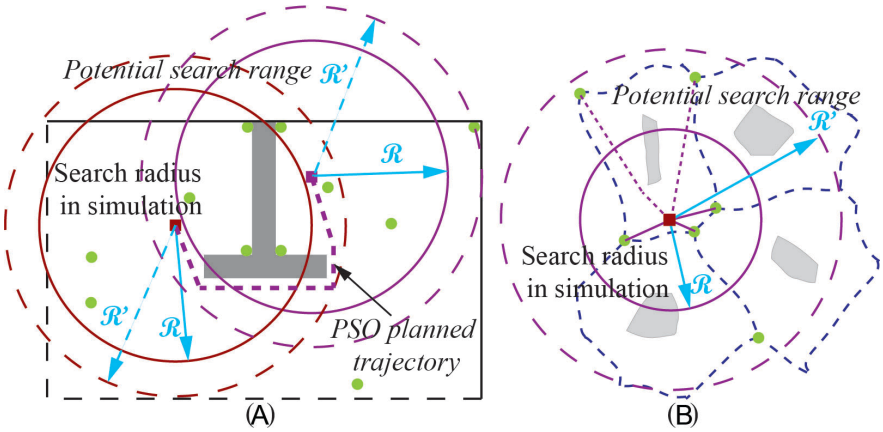

Figure 5. Illustration of the ANS algorithm analysis. (A) From Figure 11 it is enclosed by a pink dashed box. (B) From Figure 13 it is enclosed by a pink dashed box.

We carry out further discussions on our proposed ANS algorithm. Figure 5A and Figure 5B are parts of Figure 11 and Figure 13 (enclosed in pink dashed boxes), respectively. As shown in Figure 5A, the solid circles represent the search radius of the waypoints in the simulation and the red solid dots depict the nodes in the workspace. In Figure 11, we end up with the trajectory that follows the generated safe-aware road. However, if the space in the map is more sparse, our search radius $\mathcal{R}$ may increase to $\mathcal{R}'$, which may achieve the waypoints in their respective search spaces. Thus, instead of following the safe-awareness road, a new connection path is obtained through the improved PSO algorithm directly, as shown in dashed lines in Figure 5A. Moreover, the sparseness of the overall workspace may not represent the complexity of local obstacles. Therefore, the choice of the radius of the search space may require more mathematical proof and analysis.

With the increasing radius of the potential search range, more nodes are applicable for selection, such as the nodes connected with dashed lines in Figure 5B. Enlarging the search space may avoid some unnecessary detours and give a shorter path. Therefore, the trade-off between path length and safety of the autonomous robot still requires more consideration.

4. IMPROVED PSO-BASED MULTI-WAYPOINT NAVIGATION

The particle swarm optimization (PSO) algorithm is a swarm-based bio-inspired algorithm based on the behavioral observation of birds. It uses an iterative methodology to optimize randomly initialized particles to define a path from the initial position to the goal[27]. In this section an improved PSO (IPSO) algorithm by introduction of a weighted particles is addressed to resolve the multi-waypoint sequence issue.

4.1. Multi-waypoint visiting sequence

In real-world scenarios, one important factor is that the GPS coordinates provide portions for the multiple waypoints. Traveling from one waypoint to another, the distance between them determines their associated cost. The primary purpose of traveling from one waypoint to another is to simultaneously find the minimal cost of all generated trajectories. Using the coordinates of each waypoint and the PSO algorithm, the minimal-distance path can be found within the environment. The PSO algorithm finds the best waypoint visiting sequence by initializing randomized particles. The algorithm denotes the local best position as x^b and the global best position as x^g. Then by taking advantage of a fitness function, the algorithm guides each particle towards the local and global best positions. The particle velocities are updated as follows:

$$v_p(t+1) = v_p(t) + \alpha_1\omega_1[x_p^b(t) - x_p(t)] + \alpha_2\omega_2[x_p^g(t) - x_p(t)] \tag{6}$$

$$x_p^{(t+1)} = x_p^{(t)} + v_p^{(t+1)} \tag{7}$$

where, $v_p(t)$ represents the velocity of particle p at instant t, $x_p(t)$ is the position of particle p at instant t, α_1 and α_2 are the positive acceleration constants used to scale the contribution of cognitive and social components. ω_1 and ω_2 are the uniform random number between 0 and 1. $x_p^b(t)$ is the best position the particle p achieved up to instant t at current iteration, $x_p^g(t)$ is the global position that any of p's neighbors has reached up to instant t. However, if a particle p_i lies close to the $x_p^b(t)$ and $x_p^g(t)$, only one term guides the p_i to search the potential solution.The optimization process in our navigation issue is more likely trapped in local minima. Thus, an improved PSO algorithm is utilized to provide a more promising search direction for all particles during the optimization process.

$$x^w = \sum_{i=1}^{P} \bar{\alpha}_i^w x_i^b(t) \tag{8}$$

$$\bar{\alpha}_i^W = \frac{\hat{\alpha}_i^W}{\sum_{j=1}^{P} \hat{\alpha}_i^W} \tag{9}$$

$$\hat{\alpha}_i^W = \frac{\max_{1\le k\le M}\left(\mathcal{F}\left(x_k^b(t)\right)\right) - \mathcal{F}\left(x_i^b(t)\right) + \varepsilon}{\max_{1\le k\le M}\left(\mathcal{F}\left(x_k^b(t)\right)\right) - \min_{1\le k\le M}\left(\mathcal{F}\left(x_k^b(t)\right)\right) + \varepsilon}, \quad i = 1, 2, \ldots, M, \tag{10}$$

where ε is a positive constant, $\hat{\alpha}$ is the weighted constant of each particle. $\mathcal{F}(\cdot)$ is the fitness function. The worst and the best fitness values of all personal best particles are represented by $\max_{1\le k\le M}(\mathcal{F}\left(x_k^P\right))$ and $\min_{1\le k\le M}(\mathcal{F}\left(x_k^P\right))$, respectively. The order is optimized through this method, in which each waypoint is visited. A sequence of particles are initialized to compose a population in the original PSO algorithm. A possible optimal solution to an optimization issue in our multi-waypoint sequence is discovered by one particle in

the PSO. This particle indicates a possible optimal solution to the multi-waypoint navigation issue and moves to explore an optimal solution in a certain search space. In this paper, a weighted particle is introduced into a swarm to suggest a more reasonable search direction for all the particles. As a result, the best position of particle and neighbor guides the particle to move along the corrected direction for better covergence.

The multi-waypoint visiting sequence problem can be used to solve the transportation planning problem and Covid-19 disinfection robot path planning in hospitals, in which agents (vehicles) need to be delivered as well as the overall cost and time need to be minimized[14]. The algorithm of the improved PSO to finding multi-waypoint visiting sequence is explained in Algorithm 1. The objective of the algorithm is to minimize the total trajectory length of Cartesian coordinates (X_n, Y_n) of waypoints given.

In the IPSO model the $\mathcal{P}_A$ represents the particle agent, which is denoted by the $\mathcal{P}_A : \{\mathcal{P}_b, \mathcal{P}_g, \mathcal{N}\}$. $\mathcal{N}$ holds a group of particle agents which are predetermined as neighbors of $\mathcal{P}_A$. The $\mathcal{P}_A$ are defined by the following parameters.

(1) Each $\mathcal{P}_A$ requests each neighbor's current personal best location.
(2) Each $\mathcal{P}_A$ returns its current personal best to neighbors.
(3) Obtains the center location of each surrounding cluster.
(4) Determines if the current position has been visited.
(5) Determines if current position is optimal if not record current position.

Every $\mathcal{P}_A$ obtains a set of neighbors of positions during the initial setup. Utilizing a variety of topologies one can create numerous properties of neighboring particle agents to obtain better performance. Within the proposed model, we assume that each $\mathcal{P}_A$ has a static set of neighbors. Each $\mathcal{P}_A$ keeps track of its local best solution, $\mathcal{P}_b$, which is where a solution closest to the optimal solution is found in the problem space, while the global best solution is recorded in the parameter $\mathcal{P}_g$. During each iteration the $\mathcal{P}_A$ evaluates its current position and determines if it needs to perform a fitness evaluation, while simultaneous checking if the termination criteria has been met. If the termination criteria have not been met then it updates its $\mathcal{P}_b$, obtains the neighbor's $\mathcal{P}_b$ and calculates the $\mathcal{P}_g$, and marks the current position as visited.

4.2. Safety-aware IPSO multi-waypoint path planning

To ensure the robot safely reaches the waypoints via the planned visiting sequence, the safety-aware road is selected to guide the autonomous robot. Nevertheless, there is a problem with the connection path from the location of the waypoints to safety-aware roads. When we integrate the position information of a waypoint in the workspace, it may be necessary to obtain the collision-free connection path length from the waypoint to all nodes, which is computationally expensive. As shown in Figure 6A, with $\mathcal{N}$ nodes obtained in the workspace, there are $\mathcal{N}$ possible connection paths from the waypoints to the nodes in the workspace. With the initial $\mathcal{N} \times \mathcal{N}$ adjacent distance matrix obtained from GVD graph and the increasing $\mathcal{M}$ waypoints in the workspace, the size of new distance matrix is expanded to $(\mathcal{N} + \mathcal{M}) \times (\mathcal{N} + \mathcal{M})$. Since most of the connection path computations are unnecessary, a new adjacent node selection (ANS) algorithm is proposed to reduce the computational effort by restricting the search space in local regions rather than the entire working region.

The local regions are shown in Figure 6B, and the dark blue nodes, such as α and β nodes in the regions, are potential adjacent nodes to connect. The radius $\mathcal{R}$ of the local area shall be determined by the potential workspace, which determines the number of nodes in the search range. For instance, in an area with clustered obstacles, there are many nodes in the environment; thus, the search radius may be small. However, In an area with sparse obstacles, there are fewer nodes in the environment; thus, the search radius needs to be larger to include all potential nodes.

Since the entire workspace is projected through the GVD graph, we can interpret the sparseness of the entire

Algorithm 1: Improved PSO (IPSO) algorithm for waypoint sequencing

Initialize a population of particles

Set the size of the swarm to S_p, the maximum number of iteration T_{max}.

for *i=1 to* S_p **do**

  Initialize X_i within the search range of (X_{min},X_{max}) frandomly;

  Initialize V_i within the velocity range of (V_{min},V_{max}) randomly;

  $P_i = X_i$;

end

Evaluate each x_p;

Identify the best position P_g;

while *(a stop criterion is not satisfied &* $t < T_{max}$*)* **do**

  for *p=1 to* S_p **do**

    Update α_1 and α_2 by Equation (8), Equation (9), and Equation (10);

    $x^w = \sum_{i=1}^{P} \bar{\alpha}_i^w \, x_i^b(t)$

  end

  ; // The sum of particle weights

  $\bar{\alpha}_i^W = \left(\hat{\alpha}_i^W / \sum_{j=1}^{P} \hat{\alpha}_i^W\right)$; // Average the weights together

  $\hat{\alpha}_i^W = \frac{\max_{1\le k\le M}\left(\mathcal{F}\left(x_k^b(t)\right)\right) - \mathcal{F}\left(x_i^b(t)\right) + \varepsilon}{\max_{1\le k\le M}\left(\mathcal{F}\left(x_k^b(t)\right)\right) - \min_{1\le k\le M}\left(\mathcal{F}\left(x_k^b(t)\right)\right) + \varepsilon}$; // Calculate the weights of each particle

  $v_p(t+1) = v_p(t) + \alpha_1 \, \omega_1 \, [\, x_p^b(t) - x_p(t)] + \alpha_2 \, \omega_2 \, [\, x_p^g(t) - x_p(t)]$; // Update the fitness value for each particle

  $x_p^{t+1} = x_p^{t+1} + V_p^{t+1}$; // Add the fitness value to the particle position

  $x_p^{b,t+1} = x_p^{b,t}$; // Store the initial local best position

  $x_p^{g,t+1} = x_p^{g,t}$

end

; // Store the initial global best position

Evaluate $\mathcal{F}(x_p^{t+1})$;

if $\mathcal{F}(x_p^{b,t+1}) < \mathcal{F}(x_p^{t+1})$ **then**

  Update $x_p^{g,t+1}$; // Update the new local best position

end

if $\mathcal{F}(x_p^{g,t+1}) < \mathcal{F}(x_p^{b,t+1})$ **then**

  Update $x_p^{g,t+1}$; // Update the new global best position

end

workspace through the distance of the edge list $\mathcal{E}$. Nevertheless, some edge distances cannot represent the sparseness of the entire workspace, such as the edges enclosed by the red dotted line in Figure 6B.

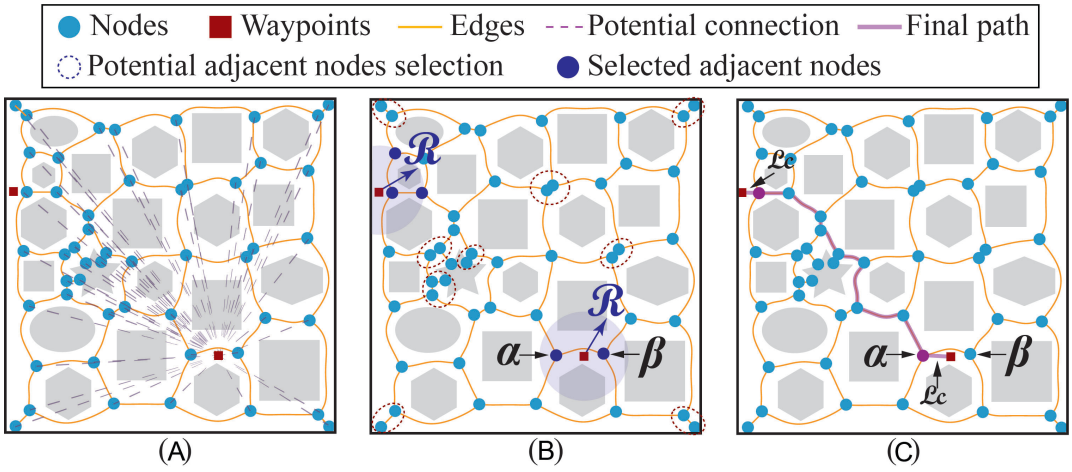

Figure 6. Illustration of the Adjacent Node Selection (ANS) algorithm. (A) The workspace with nodes, edges and waypoints. (B) The node selection in the search range. (C) The final generated path.

Therefore, to exclude these extraneous edges of distance, we sort the entire edge list before removing the lowest 10%. The radius $\mathcal{R}$ of the search range is defined as the average of the remaining edge distance. After obtaining the nodes in the search environment, we plan a collision-free trajectory from the current waypoint to reach each node through the IPSO algorithm.

The IPSO navigation algorithm is initiated in the search range to obtain the optimal path. The local search region is interpreted into grid-based map, where the obstacle areas are inaccessible grids in the workspace. Dijkstra's algorithm is utilized as a local search algorithm and the cost function within the model. For graph-based maps, they must be a method for traveling from one node to another utilizing the edges within the graph. One method of this is Dijkstra's algorithm, which utilizes a weighted graph to determine the shortest path from a source node to a target node. The algorithm also keeps track of the known shortest distances from each node while simultaneously updating their weights to improve the overall shortest path from each node. By recursively establishing a path with random solutions generated in the workspace, the IPSO algorithm can construct the collision-free path with the least fitness value, which also represents the path with minimum length. Therefore, the length of the connecting path $\mathcal{L}_c$ can be obtained, and by combining the length of the GVD path $\mathcal{L}_e$, the optimal safety-aware trajectory is obtained as shown in Figure 6C.

To effectively reduce and smooth the overall path from each waypoint to the waypoint, various methods have been developed to achieve this goal, for example, the $\mathcal{B}$-spline curve, which works by taking a set of points that are used to curve sharp close turns around obstacles and is very effective and thus widely used in smooth polylines, due to its closed-form expression of the position coordinates. The original methodology of the $\mathcal{B}$-spline curve method, in some cases, changes the trajectory of the original path created by the global navigation system. The problem can be mediated by implementing the piecewise $\mathcal{B}$-spline method, which only smooths the path around each obstacle. Lei *et al.* evaluated the effectiveness of the improved $\mathcal{B}$-spline method, and ultimately found that the hybrid method was able to reduce the overall all path in point-to-point navigation [38]. The $\mathcal{B}$-spline curve can be defined by a cardinal functions $L_{j,r}(q)$, control points B_j and degree $(r-1)$, which is given by the following equations.

$$K(q) = \sum L_{j,r}(q) B_j \tag{11}$$

where $B_j = [B_{jx}, B_{jy}]$ are the $(n+1)$ control points and a knot vector u. $N_{i,k}(u)$ are the basic functions, which are defined recursively as follows:

$$L_{j,r}(q) = \frac{(q-x_j)}{x_{j+r-1}-x_j} N_{j,r-1}(q) + \frac{(x_{j+r}-q)}{x_{j+r}-x_{j+1}} N_{j+1,r-1}(q) \tag{12}$$

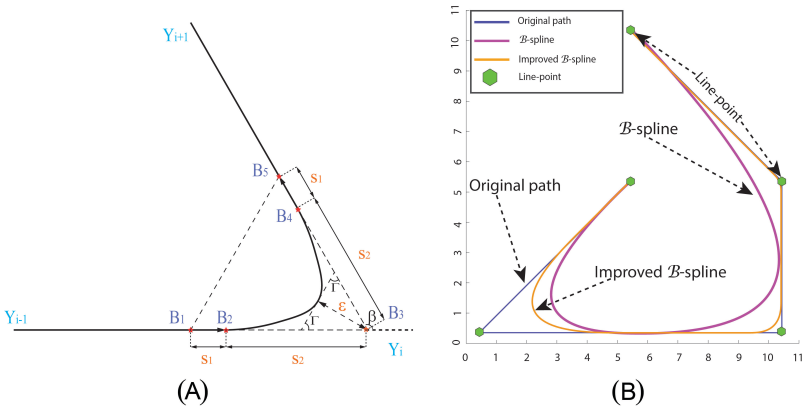

Figure 7. Illustration of the $\mathcal{B}$-spline function. (A) The improved segmented $\mathcal{B}$-spline curve. (B) The same path smoothed by the fundamental $\mathcal{B}$-spline and the improved $\mathcal{B}$-spline function.

$$L_{j,r}(q) = \begin{cases} 1, & q_j q_j \le q \le q_{j+1} \\ 0, & otherwise \end{cases} \quad ; \; q \in [0,1] \tag{13}$$

Geometric continuity G^2 is the metric used to evaluate smoothing methods, which is defined by the tangent unit and curvature vector at the intersection of two continuous segments[38] [Figure 7A]. To achieve G^2 continuity, the control points B_j of $\mathcal{B}$-spline curve to the path point, Y_j, is defined as

$$\begin{aligned} B_1 &= Y_j - (1+v)s_2 q_{j-1} \\ B_2 &= -s_2 q_{j-1} \\ B_3 &= Y_j \\ B_4 &= Y_j + s_2 q_j \\ B_5 &= Y_j + (1+v)s_2 q_{j-1} \end{aligned} \tag{14}$$

where c is smoothing length ratio $v = s_1/s_2$, and q_{j-1} defines the unit vector of $Y_{j-1}Y_j$. q_j represents the unit vector of the line Y_jY_{j+1}. The combined sum of s_1 and s_2 is the smoothed length. The half of the corner angle is denoted as: $\Gamma = \beta/2$. Using a knot vector of [0, 0, 0, 0, 0.5, 1, 1, 1, 1], the smoothing error distance ϵ and maximum curvature K_{max} within the smooth path can be expressed as:

$$\epsilon = \frac{s_2 \sin\Gamma}{2} \tag{15}$$

$$R_{max} = \frac{4\sin\Gamma}{3s_2\cos^2\Gamma} \tag{16}$$

Using the previous equations the smoothing error distance ϵ can be defined by the existing maximum curvature R_{max} given by the robot:

$$\epsilon = \frac{2\tan^2\Gamma}{3R_{max}} \tag{17}$$

The improved $\mathcal{B}$-spline model has specific advantages over the basic $\mathcal{B}$-spline model, one of which is its ability to smooth many different trajectories with various angles, as seen in Figure 7B. The curve produced by the improved $\mathcal{B}$-spline model is significantly closer to the original path than the original model. When considering the constraints of the robot, the improved $\mathcal{B}$-spline mode performs better in various degrees of angles. The overall advantages of the improved $\mathcal{B}$-spline model are as follows:

(1) The path generated is tangent and curvature continuity, so that the robot can have a smooth steering command, which can correct any discontinuity of normal acceleration and establish a safer path for the robot to follow.

(2) The improved model generates a better curve by solely affecting the two lines within the corner of the original trajectory. Each curve generated affects others within the lines.

(3) The improved model easily adjusts to the smoothed path based on the environment constraints or the robot.

Algorithm 2: Pseudocode for the adjacent node selection (ANS) algorithm

Input: Edge list $\mathcal{E}$, $\mathcal{N}$ nodes coordinates $(\mathbb{N}_x, \mathbb{N}_y)$, $\mathcal{N} \times \mathcal{N}$ distance matrix $\mathcal{D}$ and the location of the waypoint α, (α_x, α_y) and the waypoint β, (β_x, β_y).
Output: The path length of the trajectory $\mathcal{L}_t$

$N_e = size(\mathcal{E})$; // Number of the edges in the workspace
$[\mathcal{E}_s, sortInd] = sort(\mathcal{E})$; // Sort the edge list from low to high
$N_s = \lceil \frac{N_e}{10} \rceil$; // Exclude 10% of extraneous edge distance
$\mathcal{E}_t = 0$;
for $i = N_s : N_e$ **do**
  $\mathcal{E}_t = \mathcal{E}_t + \mathcal{E}_s(i)$;
end
$\mathcal{R} = \frac{\mathcal{E}_t}{N_e - N_s}$; // The radius of the search range
for $j = 1 : \mathcal{N}$ **do**
  if $(\mathbb{N}_{j,x}, \mathbb{N}_{j,y}$ *in range of* $\mathcal{R}$ *from* $\alpha_x, \alpha_y)$ **then**
    $\mathcal{A}_\alpha = [\mathcal{A}_\alpha; \mathbb{N}_{j,x}, \mathbb{N}_{j,y}]$; // Add the potential adjacent nodes of waypoint α in the list
  end
  if $(\mathbb{N}_{j,x}, \mathbb{N}_{j,y}$ *in range of* $\mathcal{R}$ *from* $\beta_x, \beta_y)$ **then**
    $\mathcal{A}_\beta = [\mathcal{A}_\beta; \mathbb{N}_{j,x}, \mathbb{N}_{j,y}]$; // Add the potential adjacent nodes of waypoint β in the list
  end
end
$N_\alpha = size(\mathcal{A}_\alpha)$; $N_\beta = size(\mathcal{A}_\beta)$; // Number of the points in the search range
Apply IPSO-based path planning algorithm;
Obtain the length of the connection path $\mathcal{L}_\alpha$ and $\mathcal{L}_\beta$ in the search range;
$\mathcal{L}_t = \infty$;
for $a = 1 : N_\alpha$ **do**
  for $b = 1 : N_\beta$ **do**
    $\mathcal{L}_{temp} = \mathcal{L}_\alpha(a) + \mathcal{D}(\mathbb{N}_{\alpha,a}, \mathbb{N}_{\beta,b}) + \mathcal{L}_\beta(b)$; // Calculate the total path
  end
  if $\mathcal{L}_t > \mathcal{L}_{temp}$ **then**
    $\mathcal{L}_t = \mathcal{L}_{temp}$; // Achieve the minimum path length
  end
end

5. REACTIVE LOCAL NAVIGATION

A crucial aspect in developing a multi-waypoint model is accounting for moving and unknown obstacles [39,40]. In a real-world setting, not all objects are static and known. To develop a more efficient model, we propose the use of a local navigator to remedy this issue.

In order to avoid dynamic and unknown obstacles, the proposed model employs the Vector Field Histogram

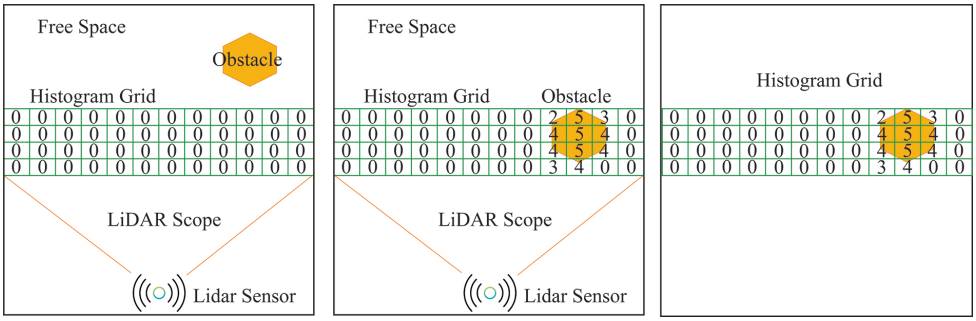

Figure 8. Illustration of how the VHF uses a probability along with histogram-based grid to detect and build a map simultaneously.

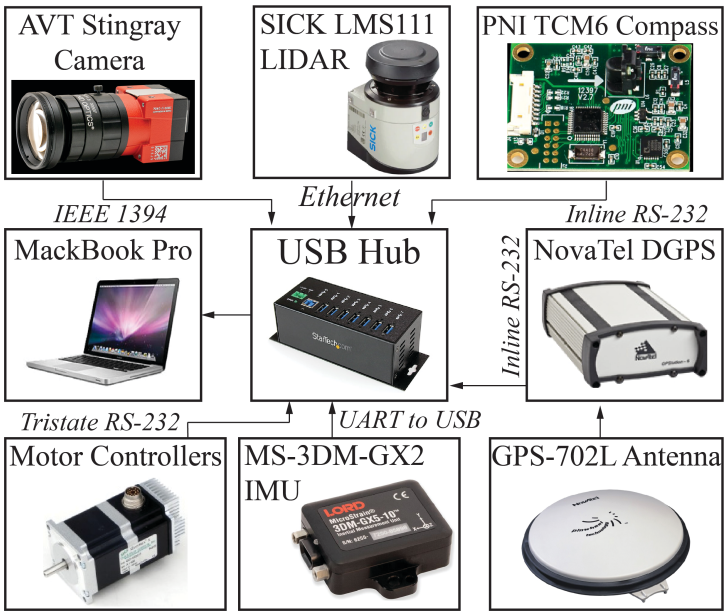

Figure 9. Robot sensor configuration for multi-waypoint navigation and mapping.

(VFH) model as a reactive local navigator. An autonomous robot uses a velocity command to and from each waypoint, provided by the local navigator[41]. By applying the VFH to the overall global trajectory with a sequence of markers, the path can be broken down into various segments to improve the efficiency in obstacle-populated workspaces. The local navigator builds a map depicting the free space and obstacles in the map by utilizing a 2D histogram grid with equally sized cells[42]. As the robot follows the generated trajectory within the workspace, the map is simultaneously built, shown in Figure 8. In developing an autonomous obstacle avoidance model, concurrent map building and navigation are crucial. The robot pose (X, Y, Yaw) is used to determine the map building. Thus, the precise registration of the built local map as a part of the global map can be carried out. This map building aims to construct an occupancy-cell-based map. The values for each cell in the map vary over the range [-127, 128][42]. The initial value is zero, which indicates that the cell is neither occupied nor unoccupied. The value is 128 if one cell is occupied with certainty and -127 if one cell is unoccupied with certainty. The values falling into (-127, 128) express contain a level of certainty in the range. When the VFH model is employed in conjunction with the GVD and IPSO algorithm, the robot can be successfully navigated through our built map with obstacle avoidance. In combination with our local navigator, a sensor configuration can be developed for the local navigator to perform it. In Figure 9 one can see the overview of our sensor configuration. The proposed configuration utilizes a 270-degree SICK LMS LiDAR sensor to detect obstacles within a range of 20 m @ 0.25-degree resolution. The LiDAR sensor scans at a rate of 25Hz. Then, it needs a method of finding our current position and the waypoints within the map. A

Table 1. Comparison of minimum path length, average path length, STD of path length, minimum time, average time and STD of time with other models. The parameter for the test of each model was: 100 initialized particles, 10 runs per data set, and a maximum of 10 minutes per run

Datasets	Model	Min length (m)	Average length (m)	Length STD (m)	Min time (s)	Average time (s)	Time STD (s)
	Proposed model	1.67E+04	1.77E+04	5.99E+02	1.75E+04	1.31E+01	6.09E-02
	ACO	1.84E+04	2.23E+04	4.40E+03	1.67E+04	1.76E+02	1.32E+00
	GA	4.22E+04	5.04E+04	5.38E+03	1.79E+04	1.39E-02	1.25E-03
Ch150	SA	2.47E+04	3.05E+04	4.11E+03	1.75E+04	6.51E+00	7.25E-01
	GWO	3.23E+04	3.66E+04	2.64E+03	5.78E-01	9.39E-01	1.73E-01
	SOM	4.26E+04	4.70E+04	2.932E+03	1.84E+03	2.26E+03	1.77E+02
	ICA	3.29E+04	3.50E+04	9.34E+02	1.55E+03	2.04E+03	1.79E+02
	Proposed model	1.09E+05	1.17E+05	5.50E+03	2.15E+01	2.15E+01	9.73E-02
	ACO	1.30E+05	2.81E+05	4.09E+05	2.44E+02	5.17E+02	8.36E+02
	GA	2.39E+05	2.57E+05	1.15E+04	1.21E-02	1.54E-02	4.45E-03
KroA200	SA	1.96E+05	2.13E+05	1.18E+04	6.27E+00	6.62E+00	8.70E-01
	GWO	2.17E+05	2.40E+05	1.24E+04	1.12E+00	1.45E+00	3.68E-01
	SOM	2.13E+05	2.60E+05	2.192E+04	5.49E+03	2.60E+05	2.31E+04
	ICA	2.12E+05	2.60E+05	6.671E+03	3.22E+02	6.81E+02	1.38E+02
	Proposed model	2.77E+05	2.89E+05	5.92E+03	4.28E+01	4.29E+01	6.06E-02
	ACO	3.37E+05	4.33E+05	4.82E+04	2.09E+02	2.37E+02	1.41E+01
	GA	3.19E+05	3.44E+05	1.17E+04	3.24E-02	3.38E-02	8.43E-04
PR299	SA	5.26E+05	5.59E+05	1.94E+04	6.27E+00	6.52E+00	6.68E-01
	GWO	2.90E+05	3.90E+05	8.15E+04	6.71E+01	8.00E+01	7.51E+00
	SOM	2.72E+05	3.15E+05	6.34E+04	4.25E+03	4.75E+03	3.45E+02
	ICA	4.81E+05	4.96E+05	1.34E+04	2.70E+03	2.81E+03	7.60E+01
	Proposed model	1.11E+05	1.14E+05	1.60E+03	1.41E+02	1.42E+02	3.65E-01
	ACO	—	—	—	—	—	—
	GA	1.37E+05	1.93E+05	6.30E+04	9.36E-02	9.57E-02	2.19E-03
PA561	SA	1.88E+05	1.92E+05	2.07E+03	6.27E+00	6.42E+00	4.29E-01
	GWO	3.02E+05	4.21E+05	5.94E+04	7.64E+01	8.26E+01	2.21E+00
	SOM	1.01E+05	1.21E+05	1.84E+04	1.1E+01	8.19E+02	3.94E+02
	ICA	1.48E+05	1.51E+05	2.43E+03	1.22E+03	2.04E+03	1.79E+02

Novatel's ProPak-LB Plus DGPS sensor is utilized to obtain our current position and how it correlates to the coordinates of each waypoint. Next, a PNI TCM6 digital compass is employed to establish our heading with an accuracy of 0.5 degrees. The sensor updates at 20Hz, which allows the robot to operate efficiently. Lastly, the configuration utilizes an AVT Stingray F-080C 1/3" CCD camera, which enables our robot to sense obstacles of various heights, shapes and sizes. The stingray camera is perfect for robot vision because it uses the IIDC IEEE 1394B protocol to transfer images. The system needs a computer system to house our operating system, sensor data, and programs for the robot. In this portion of the sensor configuration, a MackBook Pro i s equipped to suit our needs. The last step in the process is to establish a method of communication from the sensors to the computer systems. A sort of UART to USB hub is utilized for this purpose and fuses the sensor data together without losing any sensor information. The type of sensor confusion can be used on most ground-based robot systems for indoor and outdoor use.

6. SIMULATION AND COMPARISON STUDIES

In this section, simulation and comparison studies are performed to illustrate the value and vitality of the proposed model. In the first experiment, simulations are conducted using a well-known Traveling Salesman Problem (TSP) based data set, and results are compared with other heuristic-based algorithms. The proposed model is thoroughly evaluated in the second experiment through a comparison study using a similar model proven to work effectively for multi-waypoint navigation.

6.1. Comparison studies with benchmark datasets

To show the effectiveness of our IPSO waypoint sequencing model, a comparison study was conducted with well-known TSP data sets and various heuristic-based algorithms. The employed datasets and algorithms are as follows: (a) 561-city problem by Kleinschmidt (pa561); (b) 299-city problem by Patberg/Rinaldi (pr299); (c) 200-city problem A, by Krolik/Felts/Nelson (kroA200); and (d) 150-city problem by Chur Ritz (ch150). The selected datasets have been verified and widely used to prove the validity of multi-waypoint sequencing

Table 2. An illustration of the number of nodes, distance, and time spent traversing with the map to each waypoint

Model	Nodes	Distance	Time spent (s)
Zhang's model before node reduction	242	271.1	2.25
Zhang's model after node reduction	24	253.4	0.66
Proposed model	38	277.7	0.40

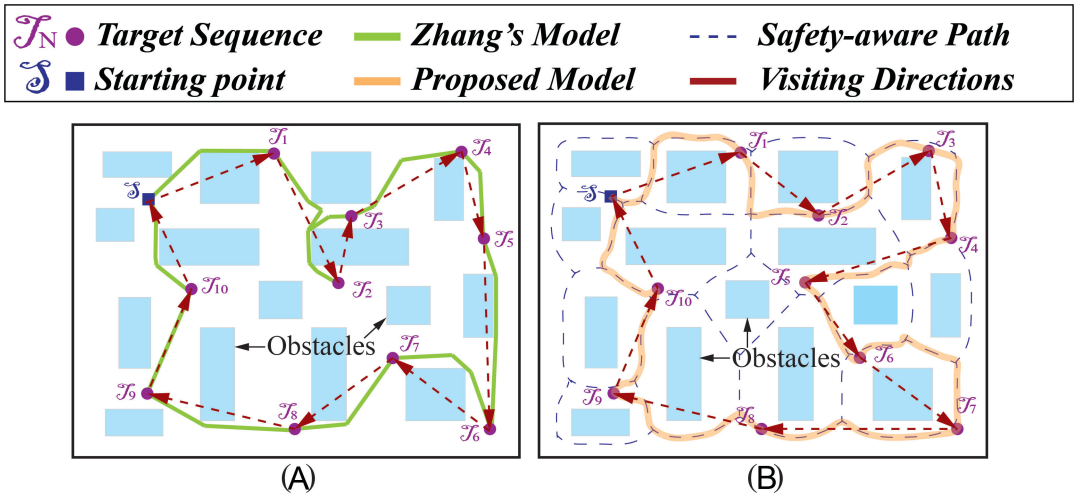

Figure 10. Illustration of the path created from the other models [43]. (A) It depicts the path created by Zhang *et al.*'s model by the green lines (redrawn by Zhang *et al.*, 2021 [43]). (B) It represents the proposed method point order and traversed path. The point order is illustrated by the violet arrows, while the orange path represents the robot path. Safety-aware roads are depicted by the blue dashed lines. The waypoints are illustrated by the violet circles.

models. The Simulated Annealing (SA) algorithm, Grey Wolf Optimization (GWO) algorithm, Ant Colony Optimization (ACO) algorithm, Genetic Algorithms (GA), Imperialist Competitive Algorithm (ICA), and Self-Organizing Maps (SOM) were chosen as the heuristic-based algorithms used in the comparison studies. The ICA algorithm is a biologically inspired algorithm by the human, which simulates the social-political process of imperialism and imperialistic competition. The SOM algorithm is similar to a typical artificial neural network algorithm, except it utilizes a competitive learning process instead of backpropagation that utilizes gradient descent.

Heuristic-based algorithms have similar attributes; due to this feature, the same parameters can be used to construct a stable comparison study for our proposed IPSO algorithm. The conducted comparison studies focus on six key attributes such as: min length (m), average length (m), length standard deviation (m), min time (s), average time (s), and time standard deviation (s). The variance between each algorithm can be seen by assessing each parameter. The above analyses show how effective the IPSO model can generate the minimum overall global trajectory in Table 1. The global trajectory generated by the compared algorithms is notably larger than the IPSO model. However, regarding the time aspect, the IPSO model was unable to achieve the shortest time. The significance of the proposed model can be seen in the STD evaluation parameter. The results of the comparison studies more than show the validity and performance of the proposed model to discover the optimal waypoint visiting sequence.

6.2. Model comparison studies

The compared models were developed to address the issues of multi-waypoint navigation and mapping in various applications. Each model uses some variation of a global navigation system in combination with an obstacle avoidance technique. The models were selected based on their map configuration and overall efficiency in solving the multi-waypoint navigation problem. Our comparison studies analyze the number of nodes, the trajectories produced, and the total time to fulfill the fastest route.

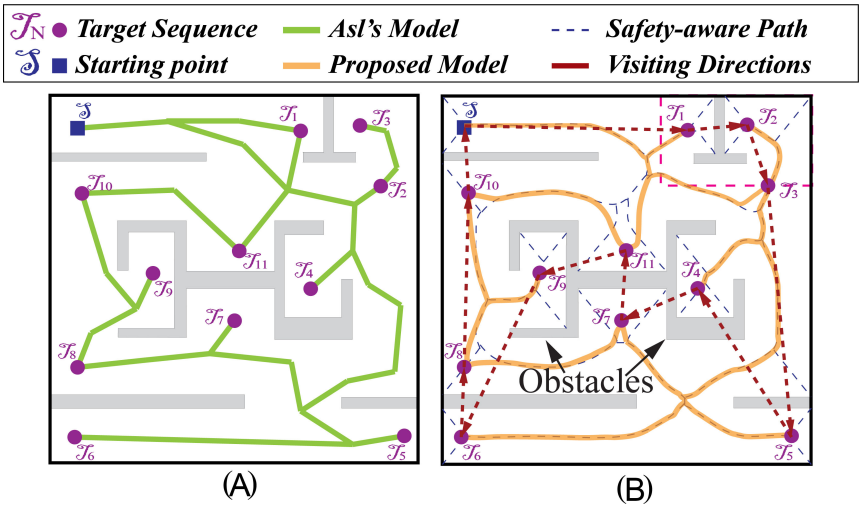

Figure 11. Illustration of the path created from the other models[44]. (A) It depicts the path created by Asl and Taghirad model by the green lines (redrawn by Asl and Taghirad, 2019[44]). (B) It represents the proposed method point order and traversed path. The point order is illustrated by the violet arrows, while the orange path represents the robot path. Safety-aware roads are depicted by the blue dashed lines. The waypoints are illustrated by the violet circles.

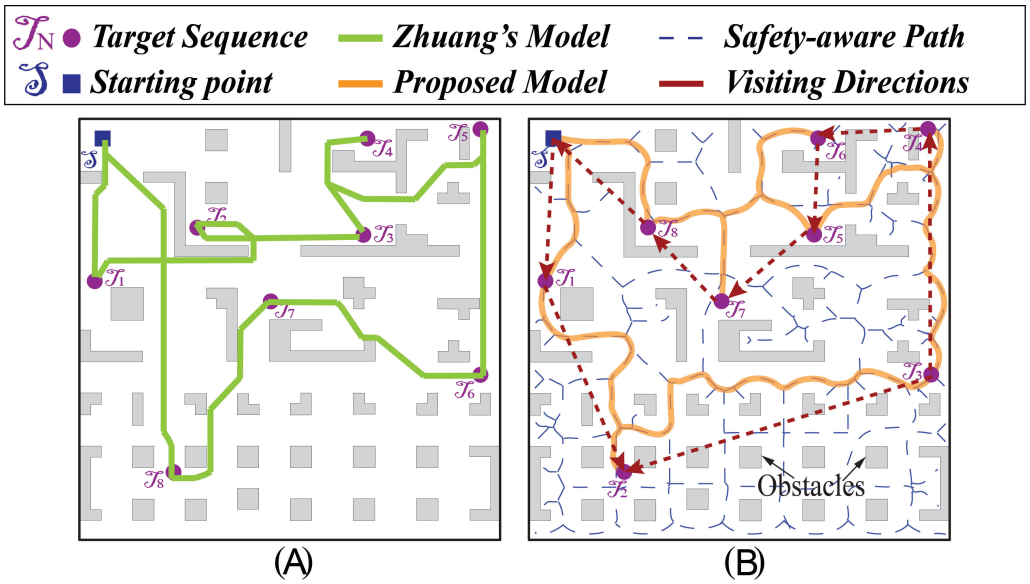

Figure 12. Illustration of the path created from the compared models[45]. (A) It depicts the path created by Zhuang *et al.*'s model by the green lines (redrawn from Zhuang *et al.*, 2021[45]). (B) It represents the proposed method point order and traversed path. The point order is illustrated by the violet arrows, while the orange path represents the robot path. Safety-aware roads are depicted by the blue dashed lines. The waypoints are illustrated by the violet circles.

It is clear that the waypoint order and paths obtained by each model are created in an obstacle-free environment, as illustrated in Figure 10A. The length created by the Zhang's model was 240.84 *m*, while the proposed model produced a shorter trajectory of 219.99 *m*. This is due to the founded waypoint orders in the environment. In Zhang's comparison study, the proposed model establishes more nodes, and the overall path is expanded by 1.09%, but the proposed model generates a solution 6.1% faster than the compared model. Zhang's proposed model has to utilize a node selection algorithm to establish its shortest path, while the proposed model does not. Due to this feature, the compared model was evaluated before this crucial step and discovered that the nodes established were vastly greater than the proposed model, as seen in Table 2. Considering this factor, the proposed model can surpass and outperform Zhang's model. Asl and Taghirad aimed to solve the multi-goal

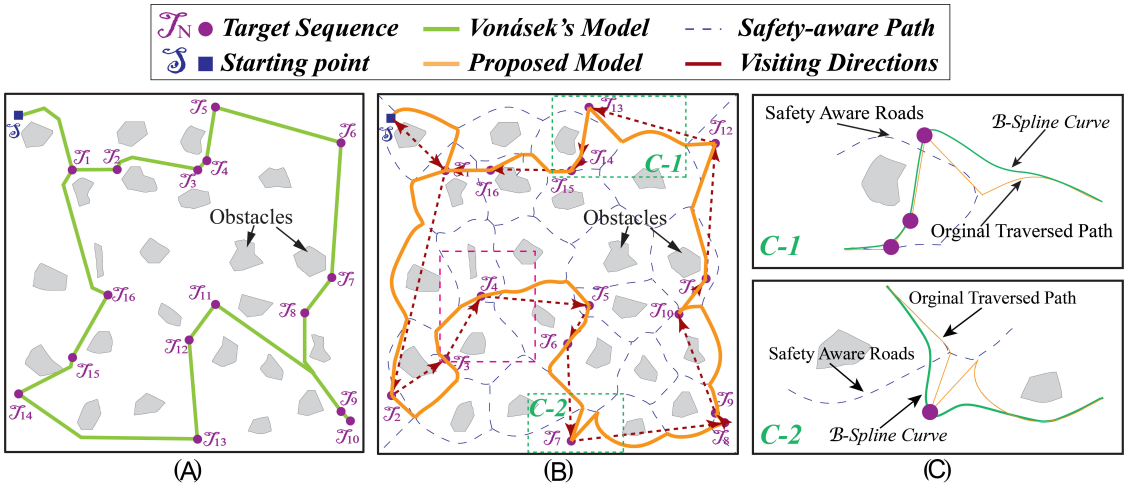

Figure 13. Illustration of the path created from the compared models[46]. (A) It depicts the path created by Vonásek's model shown by the green lines (redrawn from Vonásek and Penicka, 2019[46]). (B) It represents the proposed method point order and traversed path. The point order is illustrated by the violet arrows, while the orange path represents the robot path. Safety-aware roads are depicted by the blue dashed lines. The waypoints are illustrated by the violet circles. (C) It depicts how the $\mathcal{B}$-spline curve is applied to the known path, which smooths and reduces the path for a local navigator to traverse.

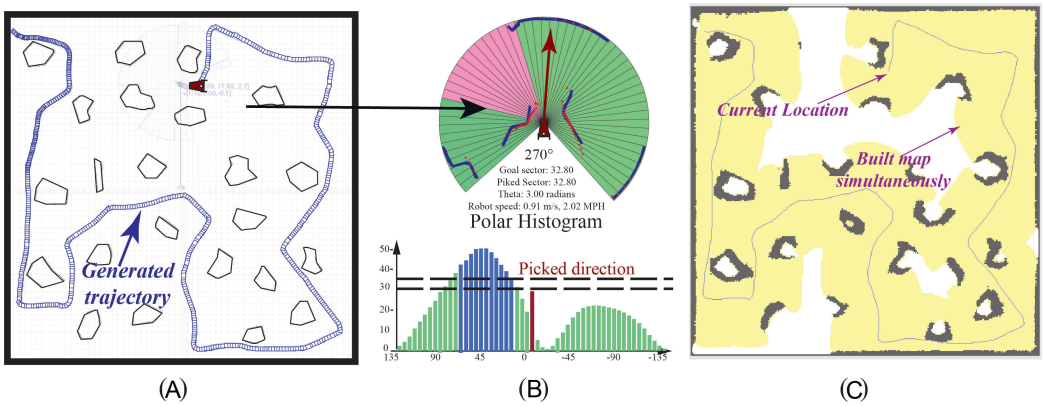

Figure 14. Illustration of the scenario in Figure 13 navigation and mapping simulation. (A) It depicts the robot traversing a majority of the map, while avoiding obstacles in the environment. (B) It illustrates a polar histogram and how the obstacles are viewed while the robot is in motion, as well as points of high impact. The obstacles are viewed as lines since the LiDAR sensor can only see the part of the object that faces the LiDAR sensor. The picked direction portion of part (B) depicts the probability of colliding with obstacles while also selecting the best direction to move the robot. (C) It demonstrates the map being simultaneously built as the the robot traverses the established trajectory.

navigation problem by developing a traveling salesman problem in the belief space[44].

From Figure 11, one can see the established path using both Asl's method as well as the method proposed in this paper. The method proposed by Asl and Taghirad has the advantage of creating a shorter path but requires a greater number of nodes than the proposed method. Figure 12 depicts the model comparison between Zhuang *et al.*'s model and the proposed method[45]. The simulation studies reveal that the proposed model had an increased length of approximately 0.05% over Zhuang *et al.*'s model. Once the compared model requires a greater number of nodes to complete its multi-waypoint navigation, another key point from this comparison is the path created from Zhuang *et al.*'s model and the proximity to the obstacles in the map. In a real-world environment, the robot could obtain server damage or cause an accident if it is too close to the surrounding obstacles[45]. The proposed method established an effective path without risking the robots well being. Vonásek and Penicka[46] models had similar results to the previous models, with an increased length

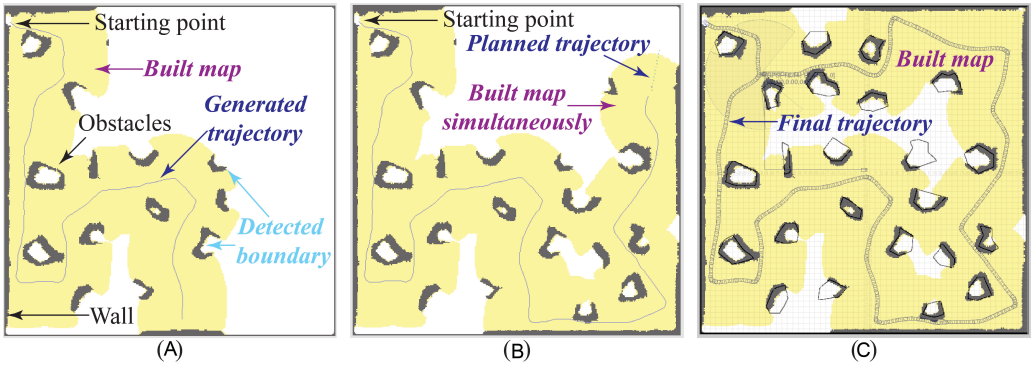

Figure 15. Illustration of the navigation and mapping ability of the proposed model. (A) The robot follows the generated trajectory and detects obstacle boundaries by the LiDAR sensor. (B) The simultaneous map building and navigation capabilities of the proposed model. (C) The fully generated trajectory and established map.

of approximately 0.05%, as seen in Figure 13. The two compared models have the same problem as Zhuang *et al.*' model [45]. The paths are excessively close to obstacles in the map and thus are not efficient for real-world implementation.

In such an environment, it is very important to consider the robot safety because of the narrow paths created being tightly packed with triangular shaped obstacles. Although most of our model comparison results showed that the path constructed with the proposed model increased from the compared models, we achieved our goal of constructing safety-aware roads for robot safety and establishing an obstacle-free path.

From Figure 14, it is observed how the local navigator establishes a map through vision sensors such as LiDAR. In Figure 14, it is obvious that the map in various stages is shown as the robot traverses along the generated trajectory found in the Vonásek's simulation [Figure 13] [46].

The robot is able to reconstruct the outer boundary of the obstacles through the LiDAR scan. These are depicted as the poly-shaped figures with a rough background and a white center.

In Figure 15A, it is clear to see the original starting position as well as the planned trajectory, which was found utilizing our proposed IPSO model. From the figures, one could observe fully and partly detected obstacles as well as the outer boundary being detected. The map depicted in Figure 15 has a height and width of 60 m. The dimensions of the robot are approximately 0.82 m long and 0.68 m wide. In Figure 15A, the robot has successfully traversed one third of the map, while simultaneously avoiding the obstacles. In Figure 15B, it illustrates the robot's planned trajectory and the map being simultaneously constructed along the path. The portions of the figure depicted in a yellow field are the built map sensed by the onboard sensors. Finally, in Figure 15C, the robot has successfully visited each waypoint and reached its final destination, and it shows the complete depiction of the map along the projected path.

7. CONCLUSION

We proposed an adjacent node selection (ANS) algorithm to find a node in the graph to connect waypoints. This algorithm is utilized in the safety-aware multi-waypoint navigation and mapping by an improved PSO and GVD model.An IPSO-based multi-waypoint algorithm has been developed to define an order for waypoint navigation. Through our proposed ANS algorithm, connections among the waypoints and the safety-aware routes to reach multi-objective optimization can be created. The feasibility and effectiveness of our model by conducting a benchmark test and model comparison studies and analyses have been demonstrated.

DECLARATIONS

Acknowledgments
The authors would like to thank the editor-in-chief, the associate editor, and the anonymous reviewers for their valuable comments.

Authors' contributions
Wrote and reviewed the manuscript: Sellers T, Lei T, Luo C, Jan GE, Ma J
All authors contributed equally.

Financial support and sponsorship
None.

Availability of data and materials
Not applicable.

Conflicts of interest
All authors declared that there are no conflicts of interest.

Ethical approval and consent to participate
Not applicable.

Consent for publication
Not applicable.

REFERENCES

1. Chu Z, Wang F, Lei T, Luo C. Path planning based on deep reinforcement learning for autonomous underwater vehicles under ocean current disturbance. *IEEE Trans Intell Veh* 2022:1–1. DOI
2. Zhao W, Lun R, Gordon C, et al. A privacy-aware Kinect-based system for healthcare professionals. In: IEEE International Conference on Electro Information Technology. Grand Forks, USA; 2016. pp. 205–10. DOI
3. Zhao W, Lun R, Gordon C, et al. Liftingdoneright: a privacy-aware human motion tracking system for healthcare professionals. *Int J Handheld Comput Res* 2016;7:1–15. DOI
4. Lei T, Luo C, Jan GE, Bi Z. Deep learning-based complete coverage path planning with re-joint and obstacle fusion paradigm. *Front Robot AI* 2022;9. DOI
5. Li X, Luo C, Xu Y, Li P. A Fuzzy PID controller applied in AGV control system. In: International Conference on Advanced Robotics and Mechatronics. Macau, China; 2016. pp. 555–60. DOI
6. Lei T, Luo C, Ball JE, Bi Z. A hybrid fireworks algorithm to navigation and mapping. In: Handbook of Research on Fireworks Algorithms and Swarm Intelligence. IGI Global; 2020. pp. 213–32. DOI
7. Jayaraman E, Lei T, Rahimi S, Cheng S, Luo C. Immune system algorithms to environmental exploration of robot navigation and mapping. In: International Conference on Swarm Intelligence. Qindao, China: Springer; 2021. pp. 73–84. DOI
8. Yang J, Chai T, Luo C, Yu W. Intelligent demand forecasting of smelting process using data-driven and mechanism model. *IEEE Trans Ind Electron* 2018;66:9745–55. DOI
9. Zhu D, Tian C, Jiang X, Luo C. Multi-AUVs cooperative complete coverage path planning based on GBNN algorithm. In: Chinese Control and Decision Conference. Chongqing, China; 2017. pp. 6761–66. DOI
10. Luo C, Yang SX, Mo H, Li X. Safety aware robot coverage motion planning with virtual-obstacle-based navigation. In: IEEE International Conference on Information and Automation. Lijiang, China; 2015. pp. 2110–15. DOI
11. Wang L, Luo C. A hybrid genetic tabu search algorithm for mobile robot to solve AS/RS path planning. *Int J Rob Autom* 2018;33:161–68. DOI
12. Wang L, Luo C, Cai J. A variable interval rescheduling strategy for dynamic flexible job shop scheduling problem by improved genetic algorithm. *J Adv Transp* 2017;2017. DOI
13. Qu Q, Zhang H, Luo C, Yu R. Robust control design for multi-player nonlinear systems with input disturbances via adaptive dynamic programming. *Neurocomputing* 2019;334:1–10. DOI
14. Penicka R, Scaramuzza D. Minimum-time quadrotor waypoint flight in cluttered environments. *IEEE Rob Autom Lett* 2022;7:5719–26.

DOI

15. Jan GE, Luo C, Lin HT, Fung K. Complete area coverage path-planning with arbitrary shape obstacles. *J Autom Contr Eng* 2019;7. Available from: https://d1wqtxts1xzle7.cloudfront.net/79144324/20191218032728291-with-cover-page-v2.pdf?Expires=1661938236&Signature=F9H9SowZfl7P9v74Xs1quZpkYuja0eBkKJxIC--LkgBppman~V~hvtZqk1Z-ChAOsmQM1p2471dlhAmBjm8EsjnfvOqvVrjjfLCVHUK-opgkdCHuQgdFors7oKBCBkgHI0tg9tVHAND8hqgv0izfLx3YKuQeNidjvTlfXT66CbSDDtsfuZUe6wTnKYrVIq993iBCwGpQmWZ8nhQGPYqiw-fC06aBPWusmC9jCpidVZpb6R0IvlZ~ii7gnj1~rdOG6AgaIqUlSEPR7csU~9-oPDnZ2FZbXqcvlcuge75e4JhqmG3sMdzLIfOSJofxK-3Ff1NLakRVxpWYA20EbJTviA__&Key-Pair-Id=APKAJLOHF5GGSLRBV4ZA [Last accessed on 31 Aug 2022].
16. Lei T, Sellers T, Rahimi S, Cheng S, Luo C. A nature-inspired algorithm to adaptively safe navigation of a Covid-19 disinfection robot. In: International Conference on Intelligent Robotics and Applications. Cham: Springer; 2021. pp. 123–34. DOI
17. Lei T, Luo C, Sellers T, Wang Y, Liu L. Multi-task allocation framework with spatial dislocation collision avoidance for multiple aerial robots. *IEEE Trans Aerosp Electron Syst* 2022. DOI
18. Chen Y, Liu C, Shi BE, Liu M. Robot navigation in crowds by graph convolutional networks with attention learned from human gaze. *IEEE Rob Autom Lett* 2020;5:2754–61. DOI
19. Chen J, Luo C, Krishnan M, Paulik M, Tang Y. An enhanced dynamic Delaunay triangulation-based path planning algorithm for autonomous mobile robot navigation. In: Intelligent Robots and Computer Vision XXVII: Algorithms and Techniques. vol. 7539. California, USA: SPIE; 2010. pp. 253–64. DOI
20. Luo C, Xiao Y, Yang SX, Jan GE. Improving vehicle navigation by a heading-enabled ACO approach. In: *World Automation Congress*. Rio Grande, USA: IEEE; 2016. pp. 1–6. DOI
21. Lei T, Luo C, Jan GE, Fung K. Variable speed robot navigation by an ACO approach. In: *International Conference on Swarm Intelligence*. Cham: Springer; 2019. pp. 232–42. DOI
22. Wang L, Luo C, Li M, Cai J. Trajectory planning of an autonomous mobile robot by evolving ant colony system. *Int J Rob Autom* 2017;32:406–13. DOI
23. Lei T, Luo C, Sellers T, Rahimi S. A bat-pigeon algorithm to crack detection-enabled autonomous vehicle navigation and mapping. *Intell Syst Appl* 2021;12:200053. DOI
24. Luo C, Yang SX, Krishnan M, Paulik M. An effective vector-driven biologically-motivated neural network algorithm to real-time autonomous robot navigation. In: IEEE International Conference on Robotics and Automation. Hong Kong, China; 2014. pp. 4094–99. DOI
25. Na YK, Oh SY. Hybrid control for autonomous mobile robot navigation using neural network based behavior modules and environment classification. *Auton* 2003;15:193–206. DOI
26. Zhong C, Luo C, Chu Z, Gan W. A continuous hopfield neural network based on dynamic step for the traveling salesman problem. In: International Joint Conference on Neural Network. Anchorage, USA: IEEE; 2017. pp. 3318–23. DOI
27. Lazreg M, Benamrane N. Hybrid system for optimizing the robot mobile navigation using ANFIS and PSO. *Rob Auton Syst* 2022;153:104114. DOI
28. Jensen-Nau KR, Hermans T, Leang KK. Near-optimal area-coverage path planning of energy-constrained aerial robots with application in autonomous environmental monitoring. *IEEE Trans Autom Sci Eng* 2021;18:1453–68. DOI
29. Janoš J, Vonásek V, Pěnička R. Multi-goal path planning using multiple random trees. *IEEE Rob Autom Lett* 2021;6:4201–8. DOI
30. Ortiz S, Yu W. Autonomous navigation in unknown environment using sliding mode SLAM and genetic algorithm. *Intell Robot* ;1:131–50. DOI
31. Bernardo R, Sousa J, Gonçalves PJ. Planning robotic agent actions using semantic knowledge for a home environment. *Intell Robot* 2021;1:101–15. DOI
32. Luo C, Yang SX. A bioinspired neural network for real-time concurrent map building and complete coverage robot navigation in unknown environments. *IEEE Trans Neural Netw* 2008;19:1279–98. DOI
33. Shair S, Chandler JH, GonzÁlez-Villela VJ, Parkin RM, Jackson MR. The use of aerial images and GPS for mobile robot waypoint navigation. *IEEE/ASME Trans Mechatron* 2008;13:692–99. DOI
34. Yang Y, Khalife J, Morales JJ, Kassas ZM. UAV waypoint opportunistic navigation in GNSS-denied environments. *IEEE Trans Aerosp Electron Syst* 2022;58:663–78. DOI
35. Teng F, Zhang H, Luo C, Shan Q. Delay tolerant containment control for second-order multi-agent systems based on communication topology design. *Neurocomputing* 2020;380:11–19. DOI
36. Lee DT, Drysdale RL III. Generalization of Voronoi diagrams in the plane. *SIAM J Comput* 1981;10:73–87. DOI
37. Takahashi O, Schilling RJ. Motion planning in a plane using generalized Voronoi diagrams. *IEEE Trans Robot* 1989;5:143–50. DOI
38. Lei T, Luo C, Ball JE, Rahimi S. A graph-based ant-like approach to optimal path planning. In: *IEEE Congress on Evolutionary Computation*. Glasgow, UK; 2020. pp. 1–6. DOI
39. Li X, Li X, Khyam MO, Luo C, Tan Y. Visual navigation method for indoor mobile robot based on extended BoW model. *CAAI Trans Intell Tech* 2017;2:142–47. Available from: https://ietresearch.onlinelibrary.wiley.com/doi/full/10.1049/trit.2017.0020 [Last accessed on 31 Aug 2022].
40. Yang Y, Deng Q, Shen F, Zhao J, Luo C. A shapelet learning method for time series classification. In: IEEE International Conference on Tools with Artificial Intelligence. San Jose, USA; 2016. pp. 423–30. DOI
41. Liu L, Luo C, Shen F. Multi-agent formation control with target tracking and navigation. In: IEEE International Conference on Information and Automation. Macao, China; 2017. pp. 98–103. DOI

42. Babinec A, Duchoň F, Dekan M, Pásztó P, Kelemen M. VFH*TDT (VFH* with time dependent tree): A new laser rangefinder based obstacle avoidance method designed for environment with non-static obstacles. *Rob Auton Syst* 2014;62:1098–115. DOI
43. Zhang B, Jin W, Gao X, Chen W. A multi-goal global dynamic path planning method for indoor mobile robot. In: International Symposium on Robotics Intelligent Manufacturing Technology. Changzhou, China; 2021. pp. 97–103. DOI
44. Noormohammadi-Asl A, Taghirad HD. Multi-goal motion planning using traveling salesman problem in belief space. *Inf Sci* 2019;471:164–84. DOI
45. Zhuang H, Dong K, Qi Y, Wang N, Dong L. Multi-destination path planning method research of mobile robots based on goal of passing through the fewest obstacles. *Appl Sci* 2021;11:7378. DOI
46. Vonásek V, Pěnička R. Space-filling forest for multi-goal path planning. In: IEEE International Conference on Emerging Technologies and Factory Automation. Zaragoza, Spain; 2019. pp. 1587–90. DOI

Sun *et al. Intell Robot* 2022;2(4):355-70
DOI: 10.20517/ir.2022.23

Intelligence & Robotics

Research Article

Open Access

Development and experimental verification of search and rescue ROV

Bing Sun[1], Wen Pang[1], Mingzhi Chen[1], Daqi Zhu[2]

[1]Shanghai Engineering Technology Research Center of Intelligent Maritime Search & Rescue and Underwater Vehicles, Shanghai Maritime University, Shanghai 201306, China.
[2]School of Mechanical Engineering, University of Shanghai for Science and Technology, Shanghai 200093, China.

Correspondence to: Prof. Bing Sun, Shanghai Engineering Technology Research Center of Intelligent Maritime Search & Rescue and Underwater Vehicles, Shanghai Maritime University,No.1550 Haigang Avenue, Pudong New Area, Shanghai 201306, China. E-mail: hmsunbing@163.com; ORCID: 0000-0002-1432-6349

How to cite this article: Sun B, Pang W, Chen M, Zhu D. Development and experimental verification of search and rescue ROV. *Intell Robot* 2022;2(4):355-70. http://dx.doi.org/10.20517/ir.2022.23.

Received: 30 Jul 2022 **First Decision:** 24 Aug 2022 **Revised:** 29 Aug 2022 **Accepted:** 5 Sep 2022 **Published:** 12 Oct 2022

Academic Editor: Simon X. Yang **Copy Editor:** Jia-Xin Zhang **Production Editor:** Jia-Xin Zhang

Abstract

This paper presents the design of a new type of search and rescue remotely operated vehicle (ROV) system. The goal is to achieve the underwater target search and detection and small target capture and rescue operation requirements. First, the overall design of the whole underwater surface system and the layout design of the propulsion system are given. On this basis, the ROV frame structure, electronic cabin, and power cabin are designed and analyzed. To accomplish the grasping task, a grasping hand is designed based on a multifunctional manipulator to achieve underwater grasping. To make the ROV more intelligent, different kinds of underwater object detection and tracking methods are adopted and analyzed. Finally, it was tested in a pool and the sea to verify the reliability and stability of the designed search and rescue ROV.

Keywords: Remotely operated vehicle, search and rescue, underwater object detection and tracking, underwater grasping

1. INTRODUCTION

Underwater search and rescue is one of the important tasks of intelligent maritime search and rescue[1,2]. It is an important application field for underwater vehicles, artificial intelligent information processing, and under-

water acoustic communication, as well as a multidisciplinary field for new technology. With the development of the marine economy, human activity in the ocean is increasing, which is also accompanied by more and more marine accidents, resulting in huge loss of life and property. Every year, hundreds of ships sink globally, with occasional submarine sinking and aircraft crashing into the sea, among other events. However, high seabed pressures, poor visibility and complex environments make it difficult for general equipment to complete underwater emergency search and rescue. Due to the large water area, extensive searches are extremely difficult, and only professional divers can dive to a certain depth. Professional divers' underwater vision and the ability to search for a fixed location are slightly better than that of current underwater robots. However, the particularity of such search and rescue and the complexity of underwater environment are great psychological tests for divers. Employing divers as the main search force is time-consuming, high-risk and laborious, and requires a large number of divers to work alternately in pairs or teams. In the complex and changeable ocean environment, how to reduce accidents and ensure the safety of people's lives and property are some of the key issues. Feasible and effective underwater search and rescue technology requires the development of intelligent robot system with precise control performance and full functions that can quickly search salvageable equipment to determine the cause of the accident. Joochim *et al.* described the design and development of a small unmanned submarine designed to explore the underwater alternative to human work[3]. The vehicle is equipped with powerful underwater probe sensors to collect underwater data, brushless DC motors for controlling direction, and real-time camera monitoring. Choi *et al.* designed a remote control vehicle (ROV) for visual inspection of harbor structures[4]. The ROV is equipped with a vision system, a navigation system, and a propeller for inspection tasks. The ROV can be operated manually to approach the target structure and obtain high-quality images for inspection, which provides much help for underwater harbor safety. Underwater robots are important carriers for deep-sea exploration resources and equipment, often equipped with different detection sensors for compex and dangerous underwater environments. Zhang *et al.* developed a 6000-meter depth rating ROV for marine scientific research[5]. With advanced technology, this ROV demonstrates the development of modern ROV equipment, making the exploration and development of deep-sea resources a reality.

Figure 1 presents the schematic diagram of an ROV searching and salvaging the target, which can be quickly deployed and recovered. The underwater robot can be continuously powered by a small generator. The operator can conduct a continuous search at a certain area from the surface, which is safe and reliable. If the ROV is entangled in rope, the diver can dive along the umbilical cord for rescue, which relieves the diver's pressure. Yue *et al.* put forward a new navigation and positioning system, which measures the distance through underwater acoustic communication and USBL[6]. It can be used for remote positioning and guidance of AUV to exchange information. Additionally, according to the successful experience of relevant rescue, it is preliminarily considered that it is feasible to use towed sonar to detect the range and find the suspected locations, and then use the underwater vehicle equipped with front sonar and ultra-short baseline to conduct a targeted investigation on these locations. Finally, the professional divers salvage the target.

The cabled ROV designed in this project for maritime search and rescue is a new generation of micro-sized cabled ROV. The ROV features a frame structure and modular design, offering several high- and low-speed expansion interfaces. Additionally, it can be equipped with auxiliary cameras according to different demands, sonar, single function or multifunctional manipulators, underwater positioning systems, altimeters, and other sensors and tools to meet different tasks that are suitable for a variety of water environments. Figure 2 shows the 3D rendering of the small search and rescue ROV designed for this project.

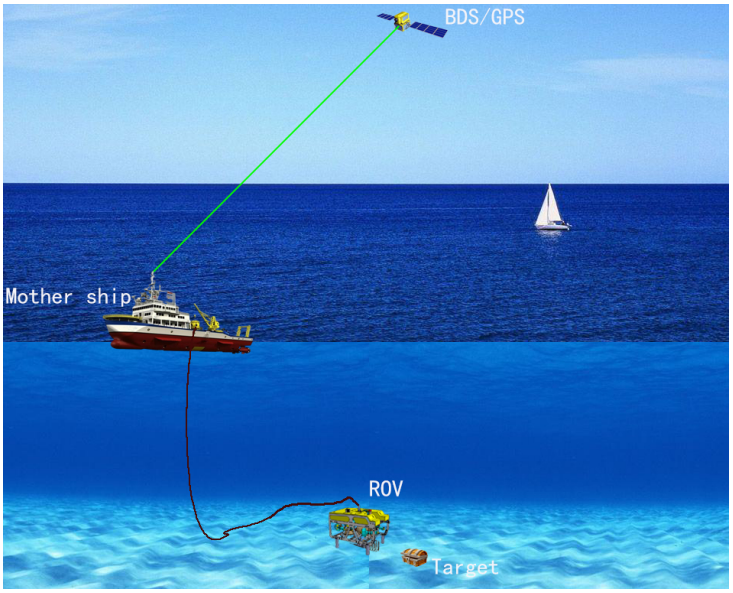

Figure 1. ROV searching and salvaging a target.

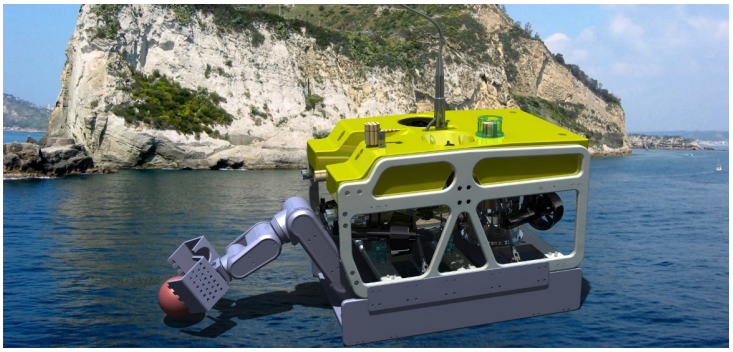

Figure 2. 3D effect diagram of search and rescue ROV.

2. DESIGN OF ROV SYSTEM FOR OFFSHORE UNDERWATER SEARCH AND RESCUE

2.1. Main specifications

The ROV system dimensions are 900 mm × 600 mm × 600 mm. It is a small search and rescue ROV capable of exploration, detection, and grasping operations. Its main technical specifications are shown in Table 1.

2.2. ROV surface operation box design

The surface operation part is the shore-based display. The shore-based display and control system belongs to the user interaction part. It is the core part to realize ROV information collection, display, and control. ROV communication and control [7,8] is a key step in the design process of an ROV. Ghilezan [9] proposed a remotely controlled ROV (remotely controlled vehicle) based on the Arduino Mega 2560 microcontroller, which acquires sensor data and controls direction and acceleration. It can directly control the ROV system and display the target search and rescue scene in real time. The hardware is PC-104 (see Figure 3), and the software is a display and control system independently developed based on the C# platform. The shore-based display and control system communicates with the ROV body through the load-bearing photoelectric composite cable and directly displays the underwater camera information, the current state of the ROV body, and the underwater acoustic detection-related control and measurement data through the display and control software. In addition, it can remotely control the ROV body. The display and control software in the system integrates many functions such as comprehensive ROV control, video monitoring, remote control, and underwater acoustic

Table 1. Main technical specifications of the ROV system

No	Item	Main specifications
1	Size/weight	900 mm × 600 mm × 600 mm/90 kg
2	Working depth	200m
3	Thrust	Forward thrust > 48 kgf/lateral thrust > 30 kgf/vertical thrust > 30 kgf
4	Speed	Forward speed ≥ 4 knots, lateral speed ≥ 1.5 knots, vertical speed ≥ 2 knots
5	Camera related	2 CCD high-definition cameras, 4 30W positive LED lights
6	Sensors	Sonar, depth gauge, altimeter, electronic compass, ultra-short baseline positioning
7	Thrusters	6 thrusters, DC150V power supply, thrust size: 17 kg/10 kg (forward/reverse)
8	Umbilical cable	300 m
9	Power supply	8 KW(max)
10	Control method	remotely control

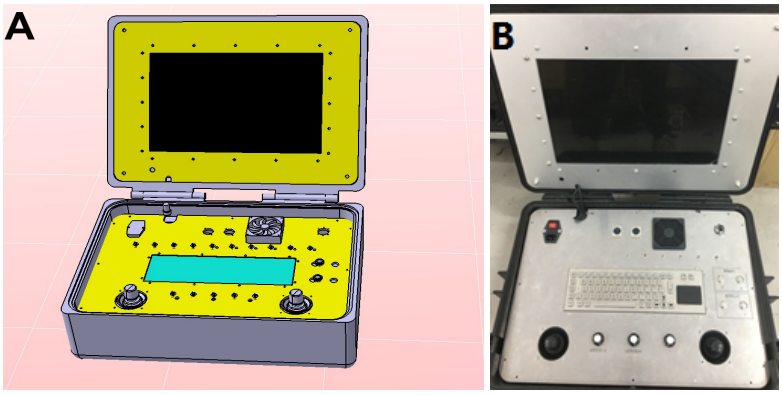

Figure 3. Design and physical drawing of the water surface control box: (A) design drawing of water surface control box; and (B) water surface control box.

positioning and tracking, with complex functions and strong pertinence, many of which are planned using label pages, with the characteristics of simple interface and convenience.

2.3. Composition and principle

The ROV system consists of the ROV body, the winch (with umbilical cable system), and the surface console. Zuluaga *et al.* developed and implemented the low-level control system of the underwater vehicle Visor3, which is an observation ROV used to monitor and inspect port facilities and underwater structures and has been used as a test platform for developing the underwater exploration robot technology in Colombia[10]. Control and navigation algorithms are all implemented in the onboard processor (BeagleBone embedded computer). The ROV body and the surface console are important components. The ROV body and the surface console are connected by zero buoyancy bearing photoelectric composite cable, which is retracted by a hand winch. The surface console adopts the hardware architecture of an industrial computer, PLC system, manual operator, image acquisition card, industrial display, three-way switching power supply, optical terminal, switch knob, keyboard and mouse, and self-developed display and control software, which mainly performs ROV control and search and rescue capturing operations. The ROV body mainly includes an ultra-high molecular weight polyethylene (UPE) frame, upper load-bearing plate, propeller, equipment cabin (control cabin and power cabin mainly composed of PC104 system and high-power power conversion module), grab mounting and fixing mechanism, buoyancy material, acoustic detection system, sensor, sonar, camera, LED lamp, counterweight, *etc.*, which are used to navigate and carry the detection equipment. Data communication between the above part and the underwater ROV body is realized by the optical transmitter and receiver. The system principle is shown in Figure 4.

The ROV system uses underwater thrusters to generate thrust, which can achieve both propulsion and steering. The layout structure of the six thrusters is shown in Figure 5, with two ascending and descending thrusters and

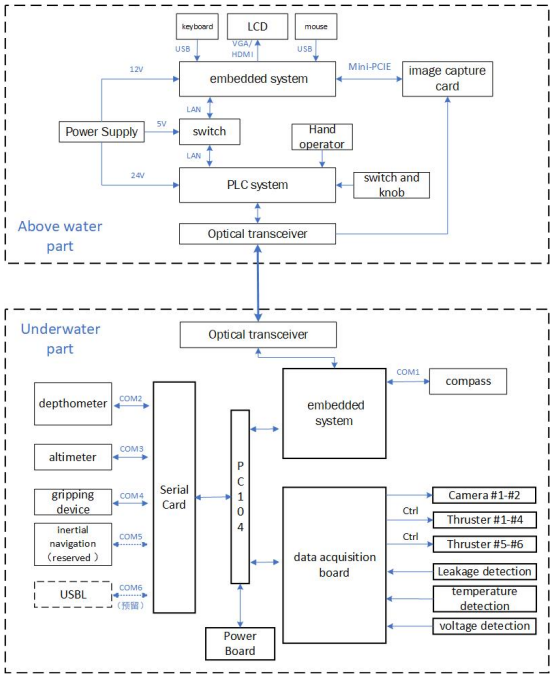

Figure 4. Display and control software interface.

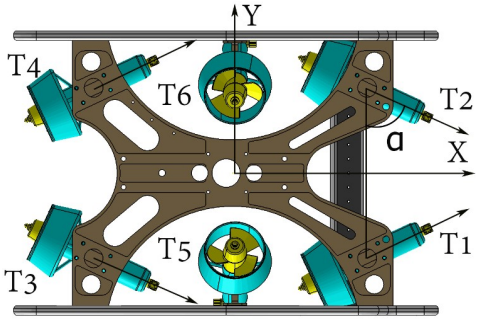

Figure 5. ROV thruster layout.

four horizontal thrusters (the two front parts are arranged at an angle of 30° with the center line and the two rear parts are arranged at an angle of 30° with the center line). With the thruster arrangement, the search and rescue ROV can mainly achieve five-degree-of-freedom movement (without pitch motion control). The ROV controller inside the control cabin collects sensor information, such as compass, attitude, depth, and height, in real time, and controls the rotation speed and direction of six thrusters in real time through the attitude balance algorithm, to realize the smooth movement of ROV diving, forward and backward motion, moving horizontally, turning, and depth orientation.

The ROV controller collects the information of peripherals (such as depth, height, attitude, compass, camera, and lighting) in real time, performs adaptive control according to the working mode, and transmits the processed relevant information to the PC-104. The PC-104 system adopts the UDP protocol and uses the optical transceiver to transmit the information in real time through the photoelectric composite cable. The ROV controller is connected to the acoustic detection system through a watertight connector. The acoustic detection system can control the working mode of the ROV (such as sink silently or fixed depth hover), cut off the power supply of the ROV, reduce the self-noise of the whole ROV system, and improve the measurement accuracy of

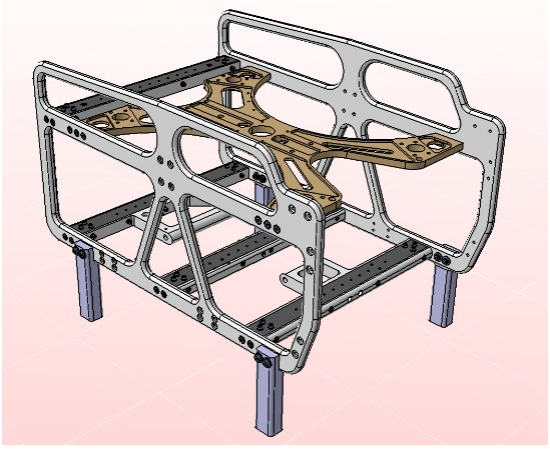

Figure 6. Frame structure diagram of the rescue ROV.

the acoustic detection system. Photoelectric conversion is adopted between the shore-based control part and the ROV body, and reliable communication is carried out through wired photoelectric composite cable.

3. HARDWARE DESIGN OF OFFSHORE UNDERWATER SEARCH AND RESCUE ROV

The hardware part of the ROV mainly includes UPE frame, upper shell, thruster, integrated control cabin, power supply cabin, floating material, counterweight, load-bearing photoelectric composite cable (including cable retracting and releasing disc device), *etc.* The UPE frame is the load-bearing support of the whole ROV body, connecting and fixing each module together. The vertical thruster is mainly used to complete the diving and floating movement of the equipment, and the horizontal thruster is mainly used to complete the forward and lateral movement of the equipment. The integrated control cabin is mainly equipped with ROV control-related equipment. The power cabin mainly supplies power to each module of the equipment and has the function of independent ROV power switching to reduce the self-noise of acoustic detection. The counterweight and floating material are mainly used to adjust equipment balance and stability. The load-bearing photoelectric composite cable adopts the marine cable standard and belongs to the photoelectric composite structure, with load-bearing and tensile capacity of more than 400 kg.

3.1. ROV body framework design

h For the ROV design, structural analysis on the frame-cover structure of ROV should be carried out[11]. The overall frame of the ROV body is made of UPE with a thickness of 20 mm. The relative density of this material is lower than that of water (0.923 g/cm^3), with good heat and cold resistance, good chemical stability, high rigidity and toughness, and good mechanical strength. This solution adopts UPE material, which can not only improve the total buoyancy of the whole robot but also ensure its stiffness stability. At the same time, the high toughness of the material can provide a certain anti-collision ability. Its structural design is shown in Figure 6.

Since the force of the search and rescue ROV mainly acts on the main bearing plate, especially when the robot is hoisted, here, only the relevant finite element stress analysis of the upper bearing plate is carried out, and the static analysis software built in CATIA is used for analysis (see Figure 7). Figure 7 shows an example of the tensile force on the upper shell when the robot is hoisted. Figure 8 shows the stress–strain diagram of the frame structure. It can be seen in the figure that the design meets the allowable deformation requirements.

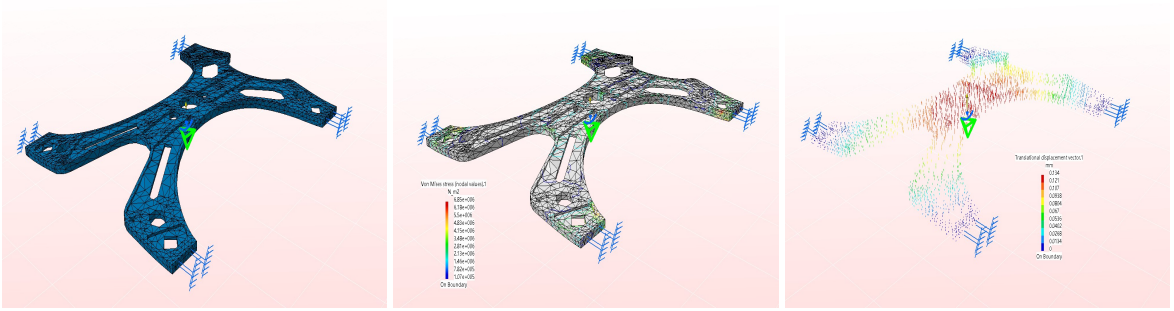

Figure 7. Static analysis of the main bearing plate.

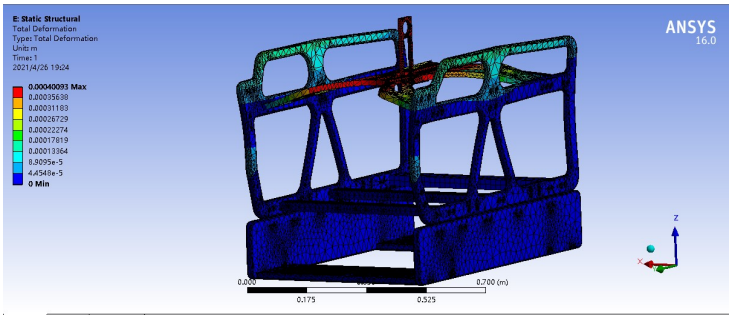

Figure 8. Analysis of ROV border deformation.

3.2. ROV electronic cabin design

This section presents the shell structure and internal support structure of the search and rescue ROV control cabin for this 200 m water depth operation, and the theoretical calculation and ANSYS finite element analysis of the strength and stability of the shell structure are carried out. This design aims to make the control cabin lighter and more compact under the constraint that it meets the safety requirements as well as lay the foundation for the actual processing and manufacturing of the ROV.

The structure of the search and rescue ROV electronic cabin is shown in Figure 9. Because the ROV electronic cabin and the power cabin are designed separately, the control cabin is mainly used to place the circuit board, which is fixed on the inner wall of the cylinder by the support rod. The separation of the electronic cabin and power cabin can better avoid the problem of strong and weak current interference. The pressing plates on both sides of the control cabin are connected with one end of the threaded flange through screws. The threaded flange is connected with the cylinder through threads, and the axial seal is realized by using double O-ring seals. The cover is integrated with the threaded flange, which is good for sealing. There is a plurality of internally threaded holes on the cover at both ends, which are used to install the propeller watertight joint, umbilical cord watertight joint, platform watertight joint, *etc.*

The static strength analysis of the electronic cabin was analyzed by CATIA's own static analysis. The displacement and equivalent stress nephograms are shown in Figure 10.

The solid model established in CATIA was imported into ANSYS. The material properties of the model are set according to the parameters of 7075 aluminum alloy, and the solid model is modeled by the finite element method. Since there are covers at both ends of the shell, fixed constraints are imposed on both sides of the shell model and pressure is applied to the outer surface of the shell. The calculated pressure is $P = 2.018 \times 2 = 4.036$ MPa, and the safety factor is 2. Figure 11 shows the displacement and equivalent stress nephograms in the 200 m water depth environment.

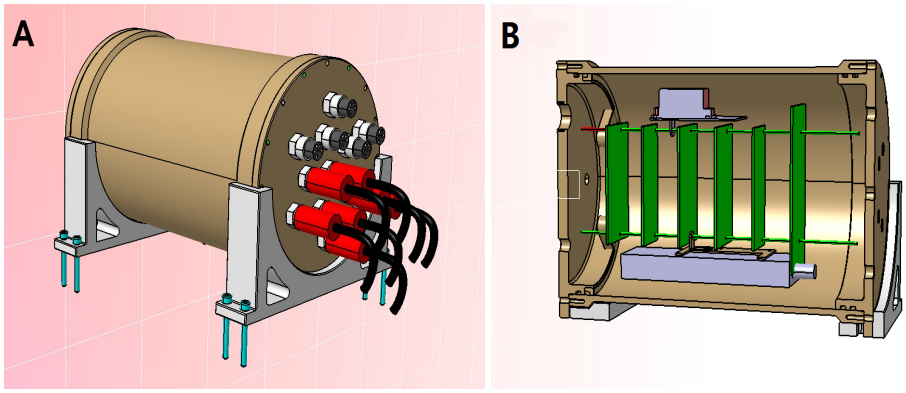

Figure 9. Electronic cabin structure design: (A) overall structure of control cabin; and (B) profile of control cabin overall structure.

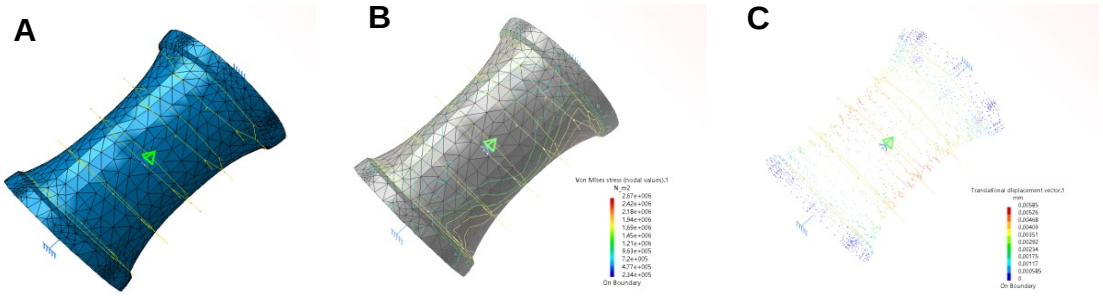

Figure 10. Static analysis of electronic cabin shell: (A) shell deformation diagram; (B) shell stress diagram; and (C) diagram of shell displacement vector.

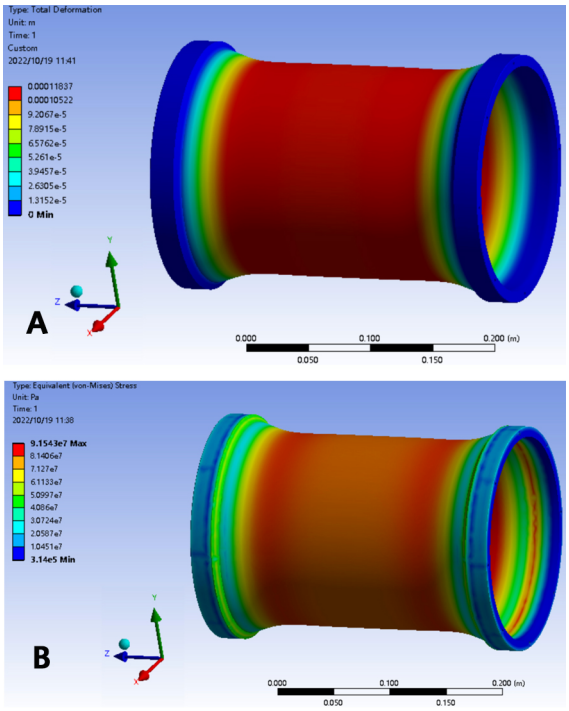

Figure 11. ANSYS static analysis of electronic cabin shell in Figure 15A and B: (A) displacement nephogram of shell static analysis; and (B) stress nephogram of shell static analysis.

3.3. ROV power cabin design

This section presents the shell structure and internal support structure of the search and rescue ROV control cabin and power cabin for the 200 m water depth operation, and the theoretical calculation and ANSYS finite element analysis of the strength and stability of the shell structure are carried out.

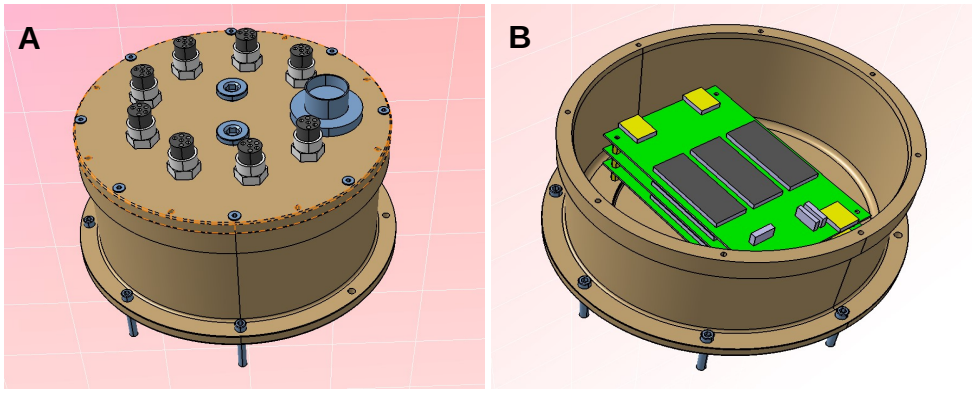

Figure 12. Design of power cabin: (A) overall structure of power cabin; and (B) internal structure of power cabin.

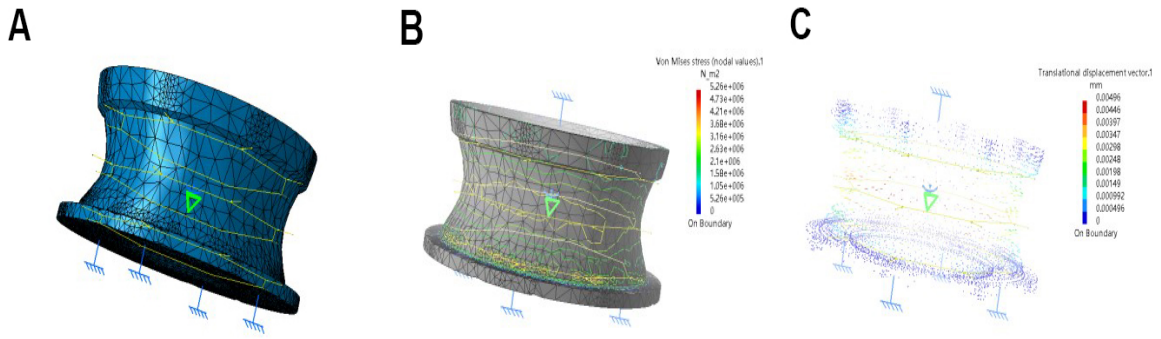

Figure 13. Static analysis of power cabin shell: (A) shell deformation diagram; (B) shell stress diagram; and (C) diagram of shell displacement vector.

3.3.1 Structure design of power cabin

The power cabin (see Figure 12) is also fixed on the frame structure of the underwater vehicle through clamps. Its main function is to provide support, heat dissipation, and protection for the power distribution management module inside the cabin. Therefore, it is required that the power cabin has excellent sealing and pressure resistance, good heat dissipation design, simple structure, and easy maintenance.

3.3.2 Strength and stress check of power cabin

Here, static analysis for the power cabin is conducted, and the analysis results are shown in Figure 13. Through analysis, it can be found that the designed power cabin can meet the requirement.

3.4. ROV buoyancy material design

An underwater vehicle is a weight-sensitive structure because it requires a balance between buoyancy and gravity in the water. Composite materials with excellent specific strength and rigidity are chemically stable. In addition, the composite structure has excellent sound absorption performance. Yang *et al.* studied the optimal calculation process for reducing the structural weight of an autonomous underwater vehicle with an integral carbon fiber structure under prescribed conditions[12]. The buoyant material needs to work in a harsh environment of high pressure and high corrosion in the ocean for a long time. Based on its different specific working occasions, various performance index requirements are considered in the design of this article. According to the selection principle and development requirements, the high-performance sandwich material Divinycell HCP50 is selected, which features excellent buoyancy performance, high impact resistance, low water absorption, thermoformability, excellent damage tolerance, simple and fast processing, good chemical

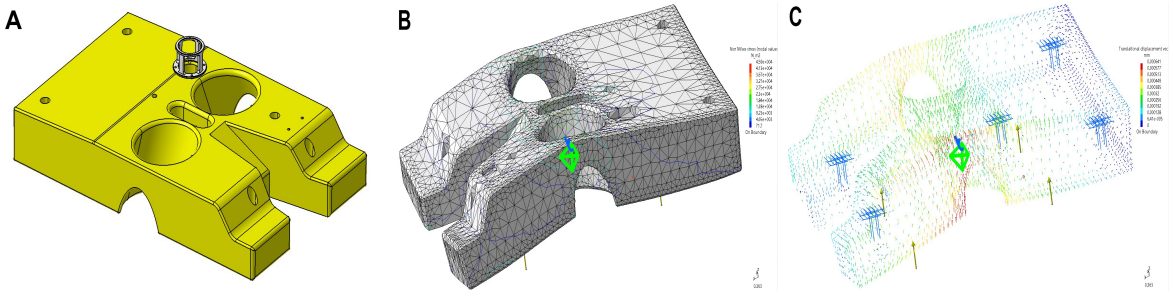

Figure 14. Design and static analysis of ROV buoyancy material: (A) design of ROV buoyancy material; (B) structure stress analysis; and (C) structural strain analysis.

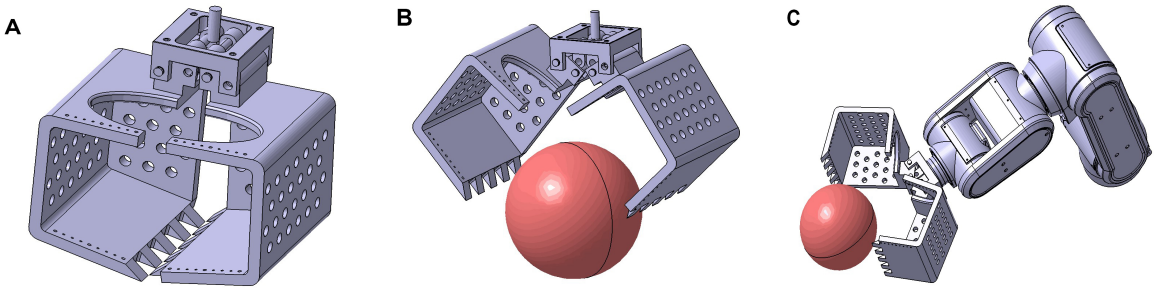

Figure 15. ROV Multifunctional Manipulator: (A) design of multifunctional manipulator gripper; (B) multifunctional manipulator grasping instructions; and (C) multifunctional manipulator grasping schematic.

corrosion resistance, high-temperature resistance, and other characteristics. The density is 250 kg/m^3, the buoyancy can be provided at 775 kg/m^3, and the working depth is 300 m, which meets the design requirements. Figure 14 shows the shape design and static analysis of buoyant materials.

3.5. ROV multifunctional manipulator grip design

The driving modes of an underwater manipulator are mainly divided into two types: hydraulic drive and motor drive. At present, most of the mature operational ROVs use hydraulic-driven underwater manipulators[13]. The main feature of the hydraulic drive is high power density, which can easily realize linear motion and rotation. However, its shortcomings are also obvious. Due to the limitation of the underwater operating environment, its dynamic control performance is not good, the control accuracy is poor, and it can easily leak oil and cause environmental pollution. Therefore, for this search and rescue ROV design, the electric manipulator mode is selected[14] considering its functionality.

Although the single-function mechanical gripper can meet simple search and rescue tasks, it is difficult to achieve some complex search and rescue tasks because there is only a single degree of freedom in opening and closing. Therefore, this design further considers a grasping scheme based on the multi-function manipulator. The mechanical gripper is the end effector of the multifunctional manipulator, which is used to complete the docking with the grasping target. The gripper is designed with a wrapping type. Figure 15 presents the design drawings of the multifunctional robotic arm gripper.

3.6. ROV hardware assembly design

When the design of each part of the ROV is completed, the overall assembly design of the robot is carried out. 3D assembly design is an important part of ROV design, which can truly reflect the final product effect of ROV, simulate the assembly process, test the process matching parameters of each component, *etc.* Figure 16 is a schematic diagram of target grasping by a multifunctional robotic arm.

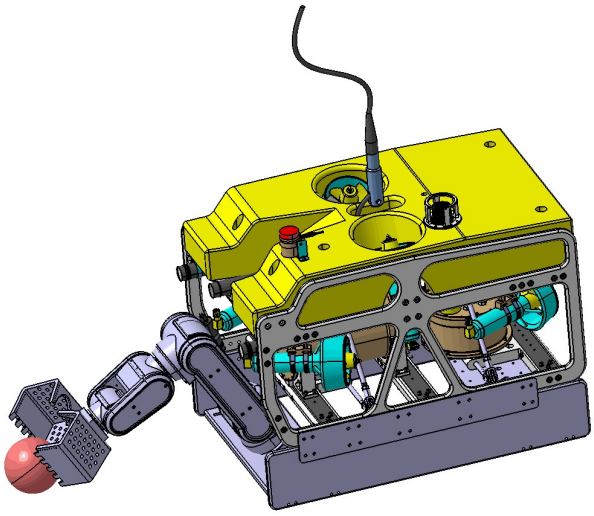

Figure 16. Grasping structure diagram of an ROV multifunctional manipulator.

4. ROV POOL TEST IN OFFSHORE UNDERWATER RESCUE

After the underwater machine prototype is assembled, a series of tests are required, which are mainly divided into indoor and outdoor tests. The indoor test mainly focuses on the power-on test of the sealed cabin to check whether the electronic components in the cabin operate normally and whether there is an alarm sound, so as to ensure the normal use of the system and test whether a single motor can operate normally and whether the overall operation can operate normally. The control board circuit in the electronic cabin was powered on to test whether the indicator light was normal to ensure that the underwater robot could move normally. Through the external frames and bottom plates on both sides, the assembly was completed with M6 screws, six thrusters, and four LED lights. The control board, processor, and power module were fixed in the electronic sealed cabin, and the expansion layer was equipped with a multifunctional manipulator.

4.1. Search and rescue ROV motion performance pool test

The premise of realizing the grasping function of an underwater robot is to test the basic functions of six degrees of freedom. It mainly tests the underwater mobility and flexibility of the underwater robot, and whether it can complete the mechanical grasping of the underwater vehicle.

The following tests were carried out: (1) The air tightness test of the manual vacuum pump was performed before launching under indoor observation for 24 h to check whether there was water accumulation in the sealed cabin and its sealing performance. (2) Switch lamp experiments were performed to check the underwater waterproofing and other functions. (3) The PTZ camera was debugged to test the stability of the platform camera and the ability to perform the up and down flip angles. (4) Whether the image transmission is normal and whether the image information can be transmitted were tested. (5) We verified the basic motion functions of the underwater vehicle in water, such as forward, backward, steering, diving, *etc.* (6) We verified the functions of controlling navigation and target searching and grabbing, as well as the key technical indicators, such as ROV speed, underwater search and rescue, and other specific indicators on the lake. The crane was used to lift and release the ROV, and the ROV positioning point was controlled to conduct high-speed navigation on the water surface corresponding to the location, straight driving, curved driving, turning in place, diving and floating, and directional and fixed depth navigation. The real object and test experiment of the ROV system are shown in Figure 17.

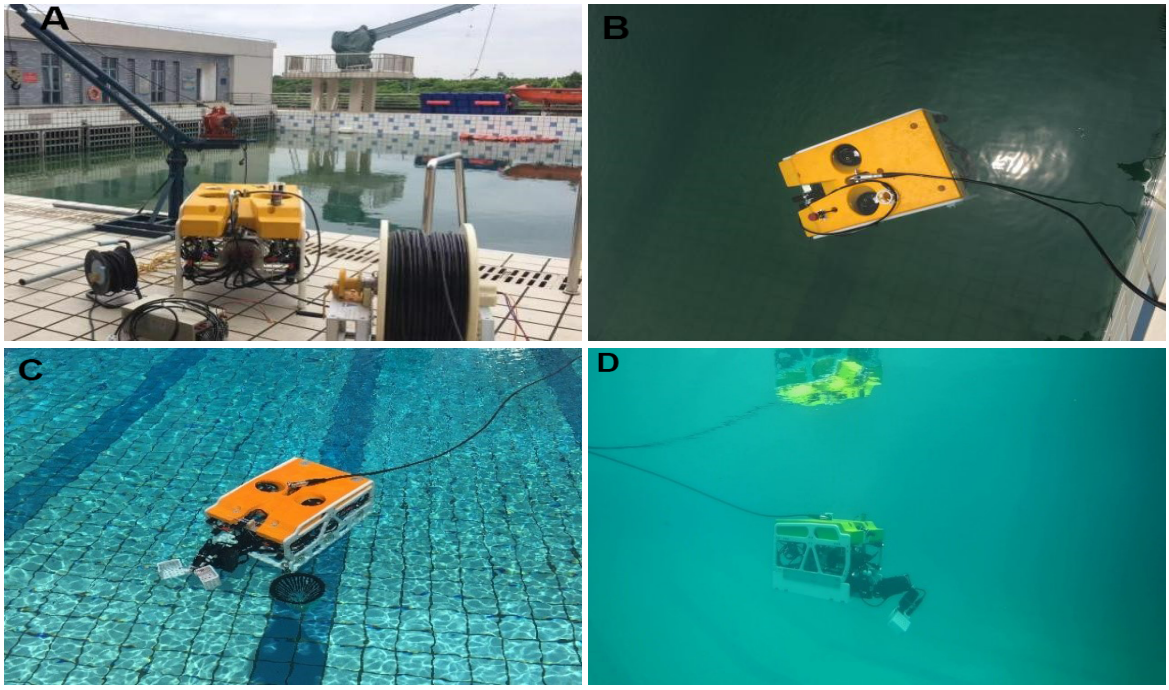

Figure 17. ROV motion performance test: (A) rescue ROV hanging; (B) ROV buoyancy and balance adjustment; (C) ROV buoyancy state test; and (D) underwater hovering state of ROV multifunctional manipulator.

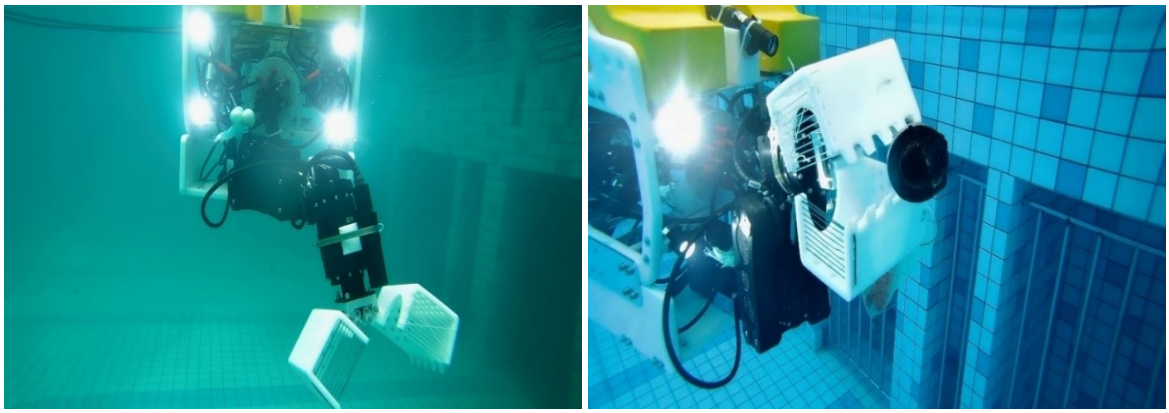

Figure 18. Underwater small target search and grasping test of ROV multifunctional manipulator.

4.2. Pool target search and rescue test of ROV multifunctional manipulator

Figure 18 shows the multifunctional search and rescue ROV carrying a multifunctional manipulator to search and grab underwater targets. It should be noted that, due to the limited number and placement of thrusters, pitch motion cannot be fully controlled. In the case where the ROV is used to grip a small object in this scenario, the jaw (garb system presented in Figure 15) mounted in front of the ROV will open and close, causing instability in the system, and the pitch motion cannot be fully compensated. Our solution is to retract the manipulator to run stably around the target, and then grasp it through the open manipulator. Because the manipulator actuator is electric, the center of gravity changes only slightly, and the improved PID controller can achieve a more stable control.

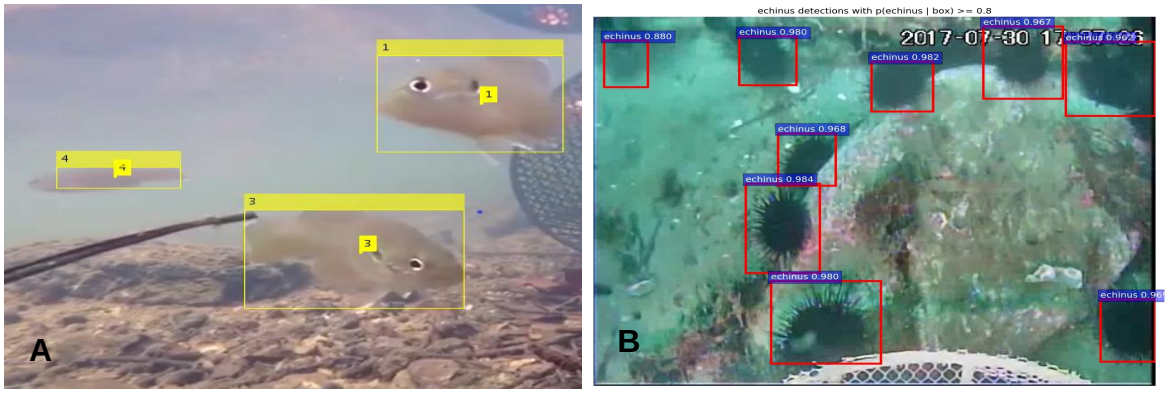

Figure 19. Detection result for fishes and seafood. A: detection result with particle filter and Hungarian method, B: detection result with Fast RCNN method.

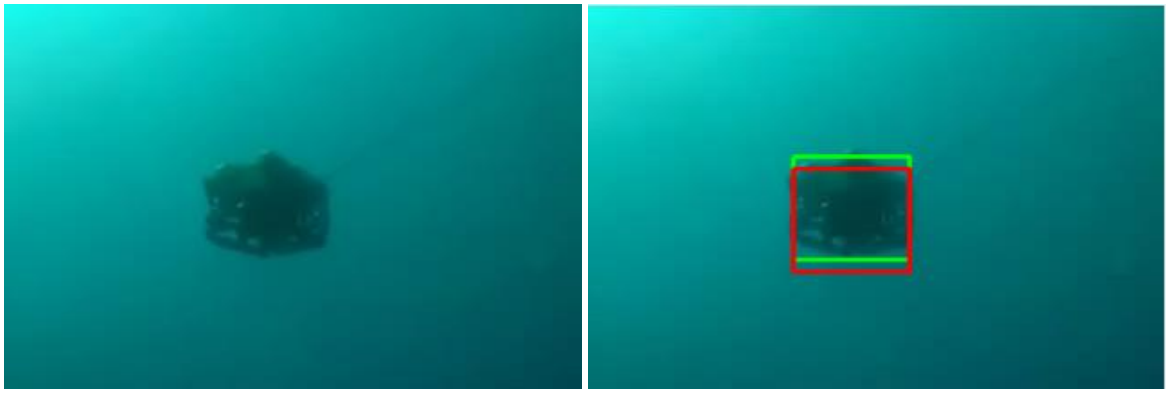

Figure 20. Tracking result of an underwater vehicle.

4.3. Intelligent underwater target detection and tracking

For underwater object search and rescue, how to make the designed ROV more intelligent is an important question, and the key point is intelligent underwater target detection and tracking. For the underwater environment, there are basically two target acquisition options: optical images and sonar images. Sonar images are suitable for searching large areas, while optical images are more suitable for close-range high-precision operation scenes. Therefore, optical images acquired by underwater cameras have become the main acquisition means for underwater search and rescue. Some intelligent methods[15,16] are applied for more intelligent underwater target detection and tracking using images. Different methods are adopted for possible object detection and tracking. Figure 19A shows the detection result with particle filter and the Hungarian algorithm method for fishes, while Figure 19B presents the detection result with the Fast RCNN method for seafood. Figure 20 presents the tracking result of an underwater vehicle, while Figure 21 shows the tracking result of moving fishes.

5. ROV OFFSHORE TEST (TARGET SEARCH AND RESCUE)

To further verify the performance of various indexes of the developed search and rescue ROV, the research group jointly cooperated with the East China Sea Rescue Bureau to conduct the sea trial experiment. The test location was selected near the Chicken Bone Reef (122°23' E, 31°11' N) in the Yangtze Estuary. This experimental ROV was carried on the test mother ship Donghai Rescue 118. The lifting and releasing of the whole ROV were completed by the crew of the Rescue Bureau. The members of our research group were mainly responsible for the laying and control of ROV cables. Figure 22 presents the search and rescue of ROV

Figure 21. Tracking result of moving fishes.

Figure 22. Search and rescue ROV is dropped into water.

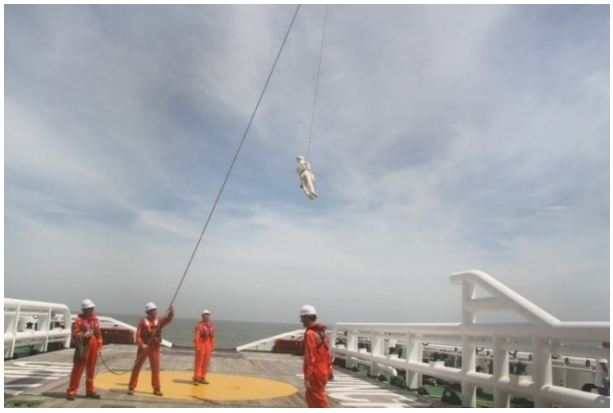

Figure 23. Search and rescue dummy hanging in the air.

offshore lifting and launching test. When the state was stable, sailing and diving tests were performed.

When the sea condition was good (Level 2–3 sea state), the search and rescue test was carried out. The search and rescue dummy (1.1 m) was hoisted from the deck position, as shown in Figure 23. The ROV was launched to search for underwater targets. It was found that the water was turbid, as shown in Figure 24, so we changed to a surface search and rescue grab test. In this case, the target dummy was still successfully approached and grabbed, and the search and rescue task was completed, as shown in Figure 25. In the process of the sea test,

Figure 24. Underwater target search.

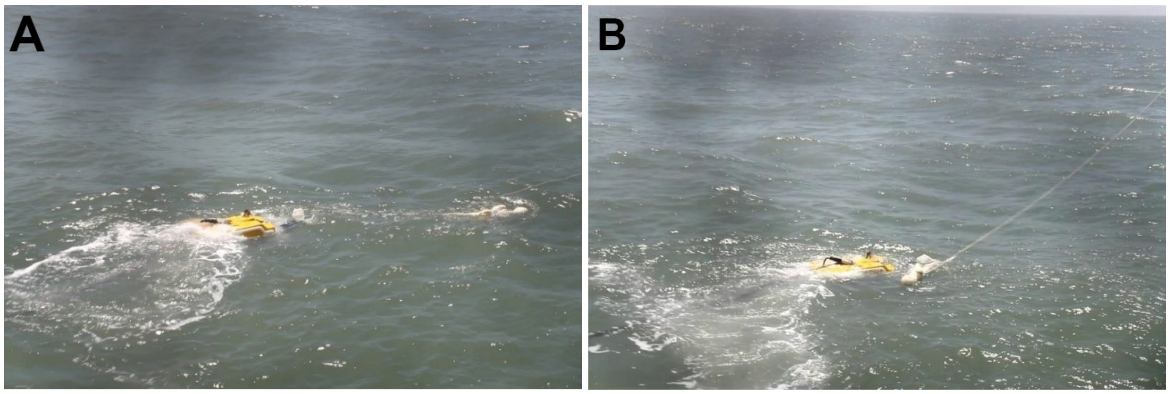

Figure 25. Underwater target search: (A) target search and rescue; and (B) ROV successfully captures the falling target for rescue.

it was found that the performance may degrade even when the current speed is not very high because of eddy currents and other conditions.

6. SUMMARY

Based on the overall structure and frame design of the search and rescue ROV, the effectiveness of the scheme was verified. At the same time, a large margin is reserved for scenarios such as maritime search and rescue. Underwater target capture and search and rescue tests were carried out through the pool and sea test, which further verified the reliability and effectiveness of the designed ROV. To better improve the intelligence of the search and rescue ROV and reliable control in a complex environment, intelligent detection and control algorithms need further research and experimental verification in the future.

DECLARATIONS

Authors' contributions

Made substantial contributions to conception, design and experiment of the study: Sun B, Pang W, Chen M
Performed oversight and leadership responsibility for the research activity planning and execution: Zhu D

Availability of data and materials

Not applicable.

Financial support and sponsorship
This work was supported in part by the National Natural Science Foundation of China under Grant 61873161, 52271321, 62033009, U1706224, Shanghai Rising-Star Program under Grant 20QA1404200 and Natural Science Foundation of Shanghai under Grant 22ZR1426700.

Conflicts of interest
All authors declared that there are no conflicts of interest.

Ethical approval and consent to participate
Not applicable.

Consent for publication
Not applicable.

REFERENCES

1. Cai L, Wu Y, Zhu S, Tan Z, Yi W. Bi-level programming enabled design of an intelligent maritime search and rescue system. *Adv Engineer Inform* 2020;46:101194. DOI
2. Ai B, Jia M, Xu H, et al. Coverage path planning for maritime search and rescue using reinforcement learning. *Ocean Engine* 2021;241:110098. DOI
3. Joochim C, Phadungthin R, Srikitsuwan S. Design and development of a remotely operated underwater vehicle. *2015 16th Int Confer Res Educ in Mechatronics (REM)* 2015:148-53. DOI
4. Choi J, Lee Y, Kim T, Jung J, Choi H. Development of a ROV for visual inspection of harbor structures. *2017 IEEE Underwater Technology (UT)* 2017:1-4. DOI
5. Zhang Q, Wang H, Li B, et al. Development and sea trials of a 6000m class ROV for marine scientific research. *2018 OCEANS - MTS/IEEE Kobe Techno-Oceans (OTO)* 2018:1-6. DOI
6. Yue Z, Wang T. Navigation and positioning system design of an AUV underwater docking. *2016 IEEE/OES China Ocean Acoustics (COA)* 2016:1-6. DOI
7. Yu C, Zhong Y, Lian L, Xiang X. An experimental study of adaptive bounded depth control for underwater vehicles subject to thruster's dead-zone and saturation. *Appl Ocean Res* 2021;117:102947. DOI
8. Yu Z, Li K, Ji Y, Yang SX. Designs, motion mechanism, motion coordination, and communication of bionic robot fishes: a survey. *Intell Robot* 2022;2:180-99. DOI
9. A. Ghilezan and M. Hnatiuc. The ROV communication and control. *2017 IEEE 23rd Int Symp Design Techn in Electr Pack (SIITME)* 2017:336-9. DOI
10. Zuluaga SA, Rúa S, Vásquez RE, Zuluaga CA, Correa JC. Development and implementation of a low-level control system for the underwater remotely operated vehicle Visor3. *OCEANS 2016 MTS/IEEE Monter* 2016:1-9. DOI
11. Park MW, Kang JI. Structural analysis on frame-cover of USV robot. *2021 21st Int Confer Control, Autom Syst (ICCAS)* 2021:1649-52. DOI
12. Yang Z, Shen H, Su Y, Liao Y. Structure design of an autonomous underwater vehicle made of composite material. *OCEANS 2014 - TAIPEI* 2014:1-4. DOI
13. X Li, H Xu, C Yang, H Wang, F Yu. Study on an underwater flexible manipulator based on hydraulic drive. *BATH/ASME 2020 Symp Fluid Power Motion Contr* 2020:Virtual, Online. DOI
14. Sivčev S, Coleman J, Omerdić E, Dooly G, Toal D. Underwater manipulators: a revi ew. *Ocean engine* 2018;163:431-50. DOI
15. Aminuddin NF, Tukiran Z, Joret A, et al. Hungarian-particle filtering based segmentation for on-road visual vehicle detection and tracking. *2022 IEEE 4th Global Confer Life Sci Technol (LifeTech)* 2022:00-3. DOI
16. Girshick R. Fast R-CNN *2015 IEEE Int Confer Comp Vis (ICCV)* 2015:1440-8. DOI

Zhang *et al*. *Intell Robot* 2022;2(4):371-90
DOI: 10.20517/ir.2022.26

Intelligence & Robotics

Research Article

Open Access

T-S fuzzy-model-based adaptive cruise control for longitudinal car-following considering vehicle lateral stability

Changzhu Zhang, Xiaoyu Wei, Zhuping Wang, Hao Zhang, Xuyang Guo

Department of Control Science and Engineering, Tongji University, Shanghai 200092, China.

Correspondence to: Prof. Hao Zhang, Department of Control Science and Engineering, Tongji University, Shanghai 200092, China. E-mail: zhang_hao@tongji.edu.cn; ORCID: 0000-0002-4527-9610

How to cite this article: Zhang C, Wei X, Wang Z, Zhang H, Guo X. T-S fuzzy-model-based adaptive cruise control for longitudinal car-following considering vehicle lateral stability. *Intell Robot* 2022;2(4):371-90.http://dx.doi.org/10.20517/ir.2022.26

Received: 13 Aug 2022 **First Decision:** 29 Aug 2022 **Revised:** 27 Sep 2022 **Accepted:** 30 Sep 2022 **Published:** 7 Nov 2022

Academic Editor: Simon X. Yang **Copy Editor:** Jia-Xin Zhang **Production Editor:** Jia-Xin Zhang

Abstract

Adaptive cruise control is one of the essential technologies of advanced driver assistance systems, which is used to maintain a safe distance between an ego vehicle and a preceding vehicle and has been extensively applied in the automotive industry and control community. Note that some vehicle manoeuvres may approach handling limits to prevent collisions under complex road conditions, which often leads to vehicle lateral instability while cruising. In this study, a T-S fuzzy model predictive control framework is applied to the problem of adaptive cruise control. Variations in the preceding vehicle velocity and road surface conditions are considered to formulate adaptive cruise control as a tracking control problem of a T-S fuzzy system subject to parameter uncertainties and external persistent perturbations. Then, a robust positively invariant set is introduced to derive an admissible T-S fuzzy controller by solving a min-max optimization problem under a series of linear matrix inequality constraints. Finally, a CarSim/MATLAB joint simulation is conducted to illustrate the effectiveness of the proposed method, which ensures longitudinal adaptive cruise control for a car-following scenario with lateral vehicle stability.

Keywords: Adaptive cruise control, T-S fuzzy model predictive control, robust positively invariant set, lateral stability

1. INTRODUCTION

Advanced driver assistance systems (ADASs) play a critical role in the automobile industry[1] by significantly decreasing drivers' workload while considerably improving driving safety and comfort[2–5]. A few examples of common applications of ADASs in automobiles in recent years are lane-keeping assist (LKA), adaptive cruise control (ACC), electronic stability control (ESC), and the precrash system (PCS)[6]. The ACC system is one of the first ADAS technologies for maintaining a safe distance between an ego car and a preceding vehicle[7]. Radar sensors detect the velocity of the preceding vehicle, which the ACC system uses to automatically modify the speed of the driving vehicle by managing the throttle opening or brake pedal levels[8].

Many adaptive cruise control strategies can be found in the literature to achieve longitudinal car-following and enhance driving performance . A fuzzy logic control technique is described in Ref.[9] that executes the ACC function on an AIT intelligent vehicle using the distance error and relative velocity information. In Ref.[10], a control system is presented that decreases vehicle waiting time at stop lights, as well as fuel consumption, by utilizing upcoming traffic signal information and short-range radar for optimal velocity trajectory planning. In Ref.[11], a safe and comfortable longitudinal automation system with a human-in-the-loop strategy is integrated into an ACC system. In Ref.[12], the use of a longitudinal controller for a smart and green ACC system is investigated to minimize energy expenditure and maximize energy regeneration.

Model predictive control (MPC) is a traditional control approach with demonstrated utility for solving multiobjective optimization problems under a variety of system constraints[13,14]. In the past few years, MPC has been widely applied to the design of ACC systems. A few examples are presented here: in Ref.[15], MPC is applied to the design of spacing-control laws for transitional vehicle manoeuvres. A fuel economy-oriented ACC system is developed in Ref.[16] to minimize vehicle fuel consumption, and a generic scale reduction framework is formulated to alleviate computational loads induced by the MPC optimization solution. In Ref.[17], a benchmark setting for the MPC on a piecewise affine system is presented for the design of ACC algorithms, and different methods are implemented and evaluated to assess their main attributes, characteristics, and strong/weak points. A stochastic MPC approach for minimizing vehicle fuel consumption is investigated in Ref.[18]. An MPC method for increasing vehicle tracking accuracy and reducing fuel consumption is developed[19] by taking into account external road information, spatiotemporal constraints and nonlinear powertrain dynamics. In Ref.[20], a personalized ACC system based on driving style identification is proposed to accommodate various driving types within an MPC framework.

The Takagi-Sugeno (T-S) fuzzy system consists of a cluster of linear subsystems as an approximation for a nonlinear system. Extensive studies have been performed on this system in recent decades[21–24]. In vehicle control, vehicle dynamics are typically regarded as linear parameter varying (LPV) systems because of inevitable variations in parameters, such as longitudinal and lateral velocities. T-S fuzzy systems are constructed to model the vehicle dynamics and address parameter variations in the system. For example, in Ref.[25], a fuzzy path-tracking controller is designed considering uncertain lateral tire forces, a time-varying vehicle speed, steering-input saturation and vehicle state conditions. In Ref.[26], a fuzzy-model-based $\mathcal{H}_\infty$ control algorithm is proposed considering constraints on the amplitude and rate of steering. In Ref.[27], a path tracking controller based on output feedback is developed considering the transient behaviour of the system. However, few studies have been performed on integrating T-S fuzzy modelling into ACC systems, and this subject requires further investigation.

The aforementioned literature review shows that substantial progress has been made in both theoretical formulations and practical applications of ACC design for car-following within the model-based predictive control framework. Notably, cars may lose lateral stability when employing a cruise controller in some emergency situations, such as rapid braking on roads with low friction coefficients. Thus, vehicle lateral stability needs to be considered when developing ACC strategies. In some studies, a linear force relationship is utilized between

tires and roads, which does not precisely describe the lateral dynamical characteristics involved, leading to severe degradation or even instability of a closed-loop system, especially when a vehicle travels at high acceleration. The longitudinal velocity is intrinsically time-varying but is regarded as a constant in a few studies, which should also be addressed. The present study has been motivated by all these considerations.

The problem of adaptive cruise control design for longitudinal car-following considering vehicle lateral stability is investigated in this study. Vehicle longitudinal car-following kinematics are used in conjunction with two degrees-of-freedom vehicle lateral dynamics to formulate an adaptive cruise control system as a robust tracking control problem of a T-S fuzzy system by considering real-time variations of the velocity of the preceding vehicle. The corresponding control problem is then transformed into a min-max optimization problem within the T-S fuzzy control framework. The concept of robust positively invariant sets is introduced to effectively address some external norm-bounded disturbances, such as the steering angle of the front wheel and the acceleration of the preceding vehicle, to ensure that the states of the closed-loop tracking dynamics converge to a compact set. Finally, results of simulations using the CarSim/MATLAB joint platform are presented to demonstrate the effectiveness of using the proposed adaptive cruise controller to realize longitudinal car-following while ensuring vehicle lateral stability.

The main contributions of this study are as follows:

(1) a T-S fuzzy control framework is used to first establish a unified T-S fuzzy dynamical model for car-following based on a combination of longitudinal kinematics, lateral dynamics, time-varying vehicle velocity, and nonlinear lateral tire/road forces as a basis for designing adaptive cruise control;

(2) a method is proposed for designing a coordinated controller of an adaptive cruise control system and a direct yaw moment control system that ensures simultaneous vehicle longitudinal car-following and lateral stability;

(3) the developed controller design method is validated by tests in a high-fidelity CarSim/Simulink joint simulation environment, and the results clearly show the effectiveness of the T-S fuzzy model predictive controller and its superiority over a conventional controller design process that does not consider vehicle lateral stabilization.

The remainder of this paper is organized as follows. A mathematical model for a vehicle is presented in Section II, which includes longitudinal kinematics, lateral dynamics, and a tire/road force model. A design for a robust T-S fuzzy model predictive controller is presented in Section III. In Section IV, the lower layer of the designed adaptive cruise control algorithm is described. The CarSim/Simulink joint simulation results are presented in Section V. Finally, we conclude the paper in Section VI.

Notations and definitions: The notations used throughout this paper are quite standard. For any x in $\mathbb{R}^n$, x^T is its transpose and $|x|$ its Euclidean norm. For a $n \times m$ matrix A, $||A||$ stands for its induced matrix norm. $\mathbb{Z}_+$ denotes the set of all nonnegative integers. We use an asterisk "$*$" to represent a term that is induced by symmetry in symmetric matrices. A real-value function $\Phi : \mathbb{R}_{\geq 0} \to \mathbb{R}_{\geq 0}$ is a $\mathcal{K}$-function if it is continuous, strictly increasing, and $\Phi(0) = 0$; it is a $\mathcal{K}_\infty$-function if it is a $\mathcal{K}$-function and when $s \to \infty$, $\Phi(s) \to \infty$. A function $\beta : \mathbb{R}_{\geq 0} \times \mathbb{R}_{\geq 0} \to \mathbb{R}_{\geq 0}$ is a $\mathcal{KL}$-function if, for each fixed $k \geq 0$, $\Phi(\cdot, k)$ is a $\mathcal{K}$-function, and for each fixed $s \geq 0$, $\Phi(s, \cdot)$ is decreasing and $\Phi(s, k) \to 0$ as $k \to \infty$.

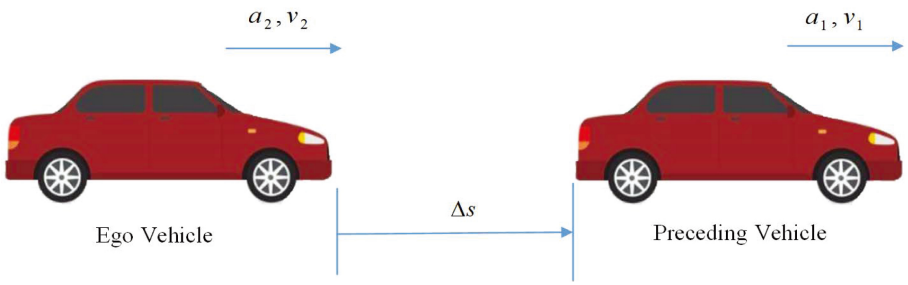

Figure 1. Vehicle longitudinal kinematics.

2. METHODS

2.1. Vehicle longitudinal kinematic model

The following symbols are used in the car-following situation shown in Figure 1: Δs is the distance between the preceding and ego vehicles; v_1 and v_2 are the longitudinal velocities of the preceding and ego vehicles, respectively; and a_1 and a_2 are the corresponding longitudinal accelerations.

The desired spacing distance between the preceding and ego vehicles is given as follows[28]:

$$d_{\text{des}} = d_0 + t_0 v_2, \tag{1}$$

where d_0 is vehicle desired distance at standstill and t_0 is the constant headway time.

The difference in the desired and actual distances between the vehicles is defined as Δd, and the relative velocity between the preceding and ego vehicles is defined as Δv; then,

$$\Delta d = \Delta s - d_{\text{des}}, \tag{2}$$

$$\Delta v = v_1 - v_2. \tag{3}$$

Considering the time delay of the engine in the driving system, we employ a first-order system to relate the actual vehicle longitudinal acceleration a_2 and the desired acceleration a_{des} as follows[29]:

$$a_2 = \frac{1}{1 + \tau_0 s} a_{\text{des}}, \tag{4}$$

where τ_0 is the engine time constant, and a_{des} is the acceleration to be determined.

The definitions given above are used to express the vehicle longitudinal kinematic model as follows:

$$\begin{cases} \dot{\Delta d} = \Delta v - t_0 a_2 \\ \dot{\Delta v} = -a_2 + a_1 \\ \dot{a_2} = \frac{-a_2 + a_{\text{des}}}{\tau_0} \end{cases}. \tag{5}$$

2.2. Vehicle lateral dynamics

Figure 2 shows the classical two-degree-of-freedom (2-DOF) bicycle model of vehicle dynamics, which is simplified in this study by collapsing each axle to a single tire to reflect the fundamental features of lateral motions.

The mass of the ego vehicle is m. I_z is the moment of inertia about the yaw axis through the vehicle's centre of gravity (CG). l_f and l_r represent the distances from the vehicle centre to the front and rear axles of the vehicle, respectively. F_{yf} and F_{yr} denote the lateral forces on the vehicle front and rear tires, respectively. δ

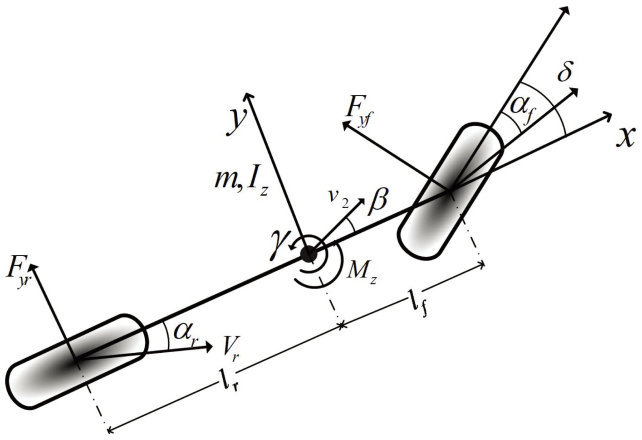

Figure 2. 2-DOF vehicle lateral dynamics.

is the steering angle for the front wheel of the vehicle. β, γ and v_x represent the sideslip angle, yaw rate, and longitudinal velocity of the ego vehicle, respectively. The vehicle lateral dynamics can be described in terms of the sideslip angle and yaw rate as follows:

$$\begin{cases} mv_2\dot{\beta}(t) = F_{yf}(t) + F_{yr}(t) - mv_2\gamma(t) \\ I_z\dot{\gamma}(t) = l_f F_{yf}(t) - l_r F_{yr}(t) + M_z(t) \end{cases} \tag{6}$$

where M_z is the external yaw moment generated by the differences in the longitudinal tire/road forces among the four tires of the vehicle.

2.3. Tire/road force model

The vehicle lateral tire/road force is generated by contact between the vehicle tires and the road surface[30]. A tire operates in the linear region for a small vehicle lateral acceleration, which can be characterized by the cornering stiffness of the front and rear tires C_f and C_r, respectively, and the corresponding sideslip angles. The relationship between the tire lateral force and sideslip angle is

$$\begin{cases} F_{yf}(t) = 2C_f\alpha_f(t) \\ F_{yr}(t) = 2C_r\alpha_r(t) \end{cases}$$

where α_f and α_r are the slip angles of front and rear tire and can be given by:

$$\begin{cases} \alpha_f(t) = \delta(t) - \frac{l_f\gamma(t)}{v_2} - \beta(t) \\ \alpha_r(t) = \frac{l_r\gamma(t)}{v_2} - \beta(t) \end{cases}.$$

However, at high lateral acceleration, the tire/road force may not be linearly proportional to the slip angle owing to differences in the road surface characteristics and cannot be simply expressed in terms of a constant cornering stiffness and sideslip angles. Therefore, we adopt an uncertain cornering stiffness, which varies over a range, to model the uncertainty in the tire/road force[31]:

$$\begin{cases} F_{yf}(t) = 2C_f + 2\Delta C_f(\bullet), \\ F_{yr}(t) = 2C_r + 2\Delta C_r(\bullet). \end{cases} \tag{7}$$

where $C_i = \frac{\max(C_i(\bullet))+\min(C_i(\bullet))}{2}$, $\Delta C_i(\bullet) \in [-\Delta C_i, \Delta C_i]$, $\Delta C_i = \frac{\max(C_i(\bullet))-\min(C_i(\bullet))}{2}(i = f, r)$, $C_i(\bullet)$ denotes the uncertain cornering stiffness, and $(\bullet)$ represents all possible variables causing variations in the cornering stiffness.

2.4. Vehicle-following system with lateral stability

Longitudinal kinematics, lateral dynamics, and an uncertain tire/road force model are integrated to formulate the following model for closed-loop car-following dynamics[32]:

$$\dot{x}(t) = (\tilde{A} + \Delta\tilde{A})x(t) + \tilde{B}_u u(t) + (\tilde{B}_d + \Delta\tilde{B}_d)d(t), \tag{8}$$

$$\tilde{A} = \begin{bmatrix} 0 & 1 & -t_0 & 0 & 0 \\ 0 & 0 & -1 & 0 & 0 \\ 0 & 0 & -\frac{1}{\tau_0} & 0 & 0 \\ 0 & 0 & 0 & -\frac{2C_f+2C_r}{mv_2} & \frac{2l_rC_r-2l_fC_f}{mv_2^2} - 1 \\ 0 & 0 & 0 & -\frac{2l_fC_f-2l_rC_r}{I_z} & -\frac{2l_f^2C_f+2l_r^2C_r}{I_zv_2} \end{bmatrix}$$

$$\tilde{B}_u = \begin{bmatrix} 0 & 0 \\ 0 & 0 \\ \frac{1}{\tau_0} & 0 \\ 0 & 0 \\ 0 & \frac{1}{I_z} \end{bmatrix}, \tilde{B}_d = \begin{bmatrix} 0 & 0 \\ 1 & 0 \\ 0 & 0 \\ 0 & \frac{2C_f}{mv_2} \\ 0 & \frac{2l_fC_f}{I_z} \end{bmatrix},$$

where $x(t) = [\Delta d, \Delta v, a_2, \beta, \gamma]^T$, $u(t) = [a_{\text{des}}, M_z]^T$, and the external disturbance $d(t) = [a_1, \delta]^T$.

The uncertain terms $\Delta\tilde{A}$ and $\Delta\tilde{B}_d$ are denoted as $\Delta\tilde{A} = \tilde{H}_1 F(t)\tilde{E}_1$ and $\Delta\tilde{B}_d = \tilde{H}_1 F(t)\tilde{E}_2$, respectively, where

$$\tilde{H}_1 = \begin{bmatrix} 0 & 0 \\ 0 & 0 \\ 0 & 0 \\ \frac{2\Delta C_f}{mv_2} & \frac{2\Delta C_r}{mv_2} \\ \frac{2l_f\Delta C_f}{I_z} & \frac{-2l_r\Delta C_r}{I_z} \end{bmatrix}, \tilde{E}_1 = \begin{bmatrix} 0 & 0 \\ 0 & 0 \\ 0 & 0 \\ -1 & -1 \\ \frac{-l_f}{v_x} & \frac{l_r}{v_x} \end{bmatrix}^T,$$

$$F(t) = \begin{bmatrix} N(t) & 0 \\ 0 & N(t) \end{bmatrix}, \tilde{E}_2 = \begin{bmatrix} 0 & 1 \\ 0 & 0 \end{bmatrix},$$

and $N(t) : R_{t\geq 0} \to [-1, 1]$ represents an unknown real-value function.

Note that in the car-following scenario, the velocity of the ego vehicle varies with that of the preceding vehicle to maintain a desired safe distance. In this study, we assume that the velocity of the preceding car varies within a bounded range $v_1 \in [v_{\min}, v_{\max}]$, where $v_{\min}$ and $v_{\max}$ represent the minimum and maximum velocities during vehicle adaptive cruising.

2.5. T-S fuzzy modeling for longitudinal car-following with vehicle lateral stability

For real-time implementation of the proposed T-S fuzzy model predictive controller in the discrete-time domain, we adopt Euler's discretization method with the sampling time T_s; then, the discrete-time model of System Equation (8) is given as

$$x(k+1) = (A + \Delta A)x(k) + B_u u(k) + (B_d + \Delta B_d)d(k), \tag{9}$$

where

$$\begin{aligned} A &= I + T_s\tilde{A}, \Delta A = I + T_s\Delta\tilde{A}, \\ B_u &= T_s\tilde{B}_u, B_d = T_s\tilde{B}_d, \Delta B_d = T_s\Delta\tilde{B}_d. \end{aligned}$$

As the velocity of the ego vehicle v_2 changes with the speed of the preceding vehicle v_1, Equation (9) is clearly a parameter-varying system.

The T-S fuzzy modelling approach is then employed to describe the time-varying car-following dynamics. We use the classical sector nonlinearity method to derive the discrete-time T-S fuzzy model given in Equation (9):

Fuzzy rule $\mathscr{R}^i$: if $\theta_1(k) \in \mathscr{F}_1^i$ and $\theta_2(k) \in \mathscr{F}_2^i$, then

$$x(k+1) = (A_i + \Delta A_i)x(k) + B_u u(k) + (B_{di} + \Delta B_{di})d(k), \tag{10}$$

where $i = 1, 2, \cdots, r$, $\theta_1(k) = \frac{1}{v_2}$ and $\theta_2(k) = \frac{1}{v_2^2}$ are premise variables, $\mathscr{F}_j^i$ is the fuzzy set, and A_i, B_{di}, ΔA_i and ΔB_{di} are the system matrices defined in Equation (9), with v_2 being replaced by $v_{\min}$ and $v_{\max}$. We use $\eta(\theta(k))$ to denote the normalized membership function of $\mathscr{F}^i$, where $\theta(k) = [\theta_1(k), \theta_2(k)]$ represents the premise variable vector, $\mathscr{F}^i = \mathscr{F}_1^i \mathscr{F}_2^i$ and $\sum_{i=1}^r \eta_i(\theta(k)) = 1$. For brevity, $\eta_i(\theta(k))$ is denoted as η_i. Considering the velocity restrictions enables us to easily derive the following weighting factors for the established T-S fuzzy system [Equation (10)]:

$$\mathscr{F}_{1\max} = \frac{\theta_{1\max} - \theta_1}{\theta_{1\max} - \theta_{1\min}} \quad , \quad \mathscr{F}_{1\min} = \frac{\theta_1 - \theta_{1\min}}{\theta_{1\max} - \theta_{1\min}}, \tag{11}$$

$$\mathscr{F}_{2\max} = \frac{\theta_{2\max} - \theta_2}{\theta_{2\max} - \theta_{2\min}} \quad , \quad \mathscr{F}_{2\min} = \frac{\theta_2 - \theta_{2\min}}{\theta_{2\max} - \theta_{2\min}}, \tag{12}$$

where $\theta_{1\max}$, $\theta_{2\max}$, $\theta_{1\min}$ and $\theta_{2\min}$ are the maximal and minimal values of θ_1 and θ_2, respectively, and $\mathscr{F}_j^i (i = 1, 2, 3, 4, j = 1, 2)$ can be obtained accordingly from Equation (11) and Equation (12). Therefore, $\mathscr{F}^i$ is derived from 2^2 combinations of $\mathscr{F}_1^i$ and $\mathscr{F}_2^i$. The following compact representation of Equation (9) is obtained by using a standard fuzzy inference approach:

$$x(k+1) = \mathscr{A}(\eta)x(k) + \mathscr{B}_u u(k) + \mathscr{B}_d(\eta)d(k), \tag{13}$$

where

$$\begin{cases} \mathscr{A}(\eta) = A(\eta) + \Delta A(\eta) = \sum_{i=1}^r \eta_i (A_i + \Delta A_i) \\ \mathscr{B}_u(\eta) = \sum_{i=1}^r \eta_i B_{ui} \\ \mathscr{B}_d(\eta) = B_d(\eta) + \Delta B_d(\eta) = \sum_{i=1}^r \eta_i (B_{di} + \Delta B_{di}) \\ \eta = \eta(k) = [\eta_1, \cdots, \eta_r]. \end{cases}$$

Note that using the sector nonlinearity modelling approach with the premise variables $\frac{1}{v_2}$ and $\frac{1}{v_2^2}$ yields a T-S fuzzy expression for the car-following system with lateral stability. The discretized form of the tracking system in Equation (9) is represented using $r = 2^2$ linear subsystems with the aforementioned membership functions. Inspired by[33], we further exploit the relationships among the premise variables to reduce the numerical computational complexity and conservativeness of the controller design. Here, we define

$$v_2 = \frac{\hat{v}_0 \hat{v}_1}{\hat{v}_1 + \hat{v}_0 \rho}, \tag{14}$$

where ρ is a scalar variable, $\hat{v}_0 = \frac{2v_{\min}v_{\max}}{v_{\min}+v_{\max}}$ and $\hat{v}_1 = \frac{2v_{\min}v_{\max}}{v_{\min}-v_{\max}}$. Therefore, we have

$$\frac{1}{v_2} = \frac{1}{\hat{v}_0} + \frac{1}{\hat{v}_1}\rho. \tag{15}$$

The new premise variable ρ is bounded as follows:

$$\rho \in [-1, 1], \tag{16}$$

where $v_2 = v_{\min}$ for $\rho = -1$ and $v_2 = v_{\max}$ for $\rho = 1$. Therefore, ρ can be used to describe the variation in v_2 from $v_{\min}$ to $v_{\max}$. In addition, the following equation can be obtained based on Taylor's approximation:

$$\frac{1}{v_2^2} \simeq \frac{1}{\hat{v}_0^2}(1 + 2\frac{\hat{v}_0}{\hat{v}_1}\rho). \tag{17}$$

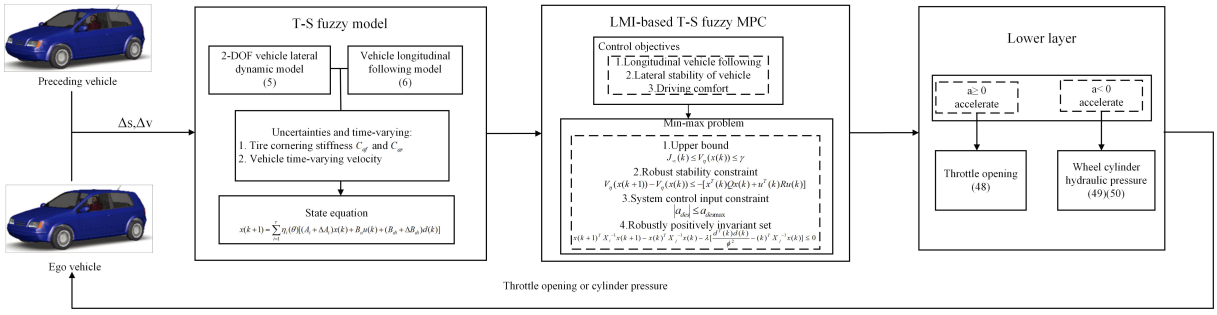

Figure 3. The whole algorithm framework.

The number of subsystems in the T-S fuzzy model Equation (10) is thus reduced from 4 to 2, which considerably decreases the computational burden associated with the controller parameters in each sampling period within the MPC framework, and facilitates real-time implementation of the model, as expected.

3. T-S FUZZY MODEL PREDICATIVE CONTROL DESIGN

In this section, we provide a detailed description of the design of an adaptive cruise controller with lateral stability based on the T-S fuzzy MPC framework. Figure 3 shows the proposed adaptive cruise control system divided into upper and lower layers. The upper layer calculates the required acceleration and direct yaw moment for vehicle-following control subject to various constraints, and the lower layer calculates the vehicle throttle opening or hydraulic cylinder pressure of the four wheels to generate control signals corresponding to the results provided by the upper layer. Before proceeding further, some definitions and lemmas are first stated.

3.1. Robust positively invariant set

Consider a discrete-time dynamical system

$$x(k+1) = f(x(k), d(k)), \tag{18}$$

where $f(0,0) = 0$, $x(k) \in \mathbb{R}^n$ is a state vector, and $d(k)$ is a control input or external disturbance that belongs to a compact set $\mathbb{D} \subset \mathbb{R}^m$ containing the origin. A robust positively invariant (RPI) set is defined below.

Definition 3.1: If $x(k) \in \Omega$ ($\Omega \subset \mathbb{R}^n$), it holds that $x(k+1) \in \Omega$ for all $d(k) \in \mathbb{D}$; then, Ω is called an RPI set for System [Equation (18)].

Lemma 3.1 [34]: The following two expressions are equivalent for System [Equation (18)] with $d^T d \le c^2$, where c is a positive constant:

- the ellipsoidal set $\Omega_p \triangleq \{x^T P x \le \gamma\}$, where $P > 0$, is a robust positively invariant set;
- the inequality $x(k+1)^T P x(k+1) \le x^T P x$ holds if the external disturbance satisfies $\frac{1}{c^2} d^T d \le \frac{1}{\gamma} x^T P x$.

3.2.Input-to-state stability

We define input-to-state stability (ISS) for use in the following sections.

Definition 3.2: A discrete-time system $x(k+1) = f(x(k), d(k))$ is ISS if there exist a $\mathcal{KL}$-function $\beta : \mathbb{R}_{\ge 0} \times \mathbb{Z}_+ \to \mathbb{R}_{\ge 0}$ and a $\mathcal{K}$-function ρ satisfying

$$||x(k, x_0, d(k))|| \le \beta(||x_0||, k) + \rho(\sup_{k \ge 0} ||d(k)||), \tag{19}$$

where x_0 is the initial state, $d(k)$ is the input sequence, and k is the sampling time instant.

Definition 3.3: A function $V : \mathbb{R}^n \to \mathbb{R}_{\geq 0}$ is called an ISS-Lyapunov function for the system $x(k+1) = f(x(k), d(k))$ if there exist $\mathcal{K}_\infty$-functions α_1, α_2, α_3 and a $\mathcal{K}$-function ρ satisfying

$$\alpha_1(||x(k)||) \leq V(x(k)) \leq \alpha_2(||x(k)||),$$
$$V(x(k+1)) - V(x(k)) \leq -\alpha_3(||x(k)||) + \rho(\sup_{k\geq 0}||d(k)||).$$

Lemma 3.2[35]: A system is said to have ISS if it admits a continuous ISS-Lyapunov function.

3.3. T-S fuzzy model-based predictive control

We adopt the following model within the framework of predictive control to represent the future dynamics of the T-S fuzzy system for vehicle-following considering lateral stability:

$$x(k+i+1|k) = \mathscr{A}(\eta)x(k+i|k) + \mathscr{B}_u u(k+i|k) + \mathscr{B}_d(\eta)d(k+i|k), \tag{20}$$

where $x(k+i|k)$, $u(k+i|k)$ and $d(k+i|k)$ represent the predicted state, control input and external disturbances at the $(k+i)$th time instant, respectively, and $i \in \{1, 2, \cdots\}$. The stage cost $\ell(k+i|k)$ can be represented as

$$\ell(k+i|k) = x(k+i|k)^T Q x(k+i|k) + u(k+i|k)^T R u(k+i|k) - \tau d(k+i|k)^T d(k+i|k) \tag{21}$$

where Q and R are the weighting matrices of the state variables of the system and control inputs, respectively. τ is the weight related to the external disturbance. We simplify this notation by using $x(k+i)$, $u(k+i)$ and $d(k+i)$ to denote $x(k+i|k)$, $u(k+i|k)$ and $d(k+i|k)$, respectively.

Consider the following objective function $\mathcal{J}_p$

$$\mathcal{J}_p(k) = \sum_{i=0}^{p-1} \ell(k+i|k) + V(x(k+p|k)), \tag{22}$$

where $\ell(k+i|k)$ is the stage cost at the predicated time instant, and the positive-definite function $V(x(k+p|k))$ is called the terminal cost. This type of cost function was proposed in Ref.[36] to develop a novel synthesis method with enhanced robustness.

As the cost function cannot be optimized in real time due to the unknown external disturbance, the upper limit of the cost function is minimized here. We define the following fuzzy quadratic Lyapunov function:

$$V(x(k)) = \sum_{i=1}^{2} \eta_i(\theta) x(k)^T P_i x(k) = x(k)^T P(\eta) x(k) \tag{23}$$

where P_j is a positive definite matrix. Let the Lyapunov function satisfy the following inequality constraint:

$$V(x(k+i+1)) - V(x(k+i)) \leq [x(k+i)^T Q x(k+i) + u(k+i)^T R u(k+i) - \tau d(k+i)^T d(k+i)]. \tag{24}$$

Add both sides of the inequality from $i = 0$ to ∞, then we get

$$\mathcal{J}_\infty(k) \leq V(x(k)) - V(x(\infty)),$$

which implies that we can infer the upper bound of the objective function $\mathcal{J}_\infty$ from the positiveness property of the function $V(x(\infty))$. Assume a scalar γ exists that satisfies

$$V(x(k)) \leq \gamma. \tag{25}$$

Defining $X_j = \gamma P_j^{-1}$ and applying the Schur complement operation yields the following sufficient condition for Equation (24):

$$\begin{bmatrix} 1 & x(k)^T \\ x(k) & X_j \end{bmatrix} \geq 0. \tag{26}$$

Then, the aforementioned optimization problem is converted into the minimization of the upper bound of the infinite-horizon objective function:

$$\begin{aligned} &\min \gamma \\ &\text{s.t. } \textit{Equation (25)}. \end{aligned} \tag{27}$$

A state feedback law $u(k) = F_\eta x(k)$ is applied to minimize the upper bound of the performance functions $\mathcal{J}_p$ and $F_\eta = \sum_{j=1}^{n} \eta_i(\theta) F_j$, where $F_j = Y_j X_j$. Considering the inequality [Equation (24)] yields

$$\begin{aligned} &x(k)^T \left[\left(A(\eta) + \Delta A(\eta) + B_u(\eta) F_\eta\right)^T P_\eta * -P_\eta + Q + F_\eta^T R F_\eta \right] x(k) \\ &+x(k)^T \left(A(\eta) + \Delta A(\eta) + B_u(\eta) F_\eta\right)^T P_\eta \left(B_d(\eta) + \Delta B_d(\eta)\right) * d(k) \\ &+d(k)^T \left(B_d(\eta) + \Delta B_d(\eta)\right)^T P_\eta \left(A(\eta) + \Delta A(\eta) + B_u(\eta) F_\eta\right) x(k) \\ &+d(k)^T \left[\left(B_d(\eta) + \Delta B_d(\eta)\right)^T P_\eta * -\tau I \right] d(k) \le 0, \end{aligned} \tag{28}$$

which is equivalent to

$$\begin{bmatrix} x(k) \\ d(k) \end{bmatrix}^T \begin{bmatrix} \Pi_1 & \Pi_2 \\ * & \Pi_3 \end{bmatrix} \begin{bmatrix} x(k) \\ d(k) \end{bmatrix} \le 0, \tag{29}$$

$$\begin{aligned} \Pi_1 &= \left[A(\eta) + \Delta A(\eta) + B_u(\eta) Y_\eta\right]^T P_\eta * -P_\eta + Q + F_\eta^T R F_\eta \\ \Pi_2 &= \left[A(\eta) + \Delta A(\eta) + B_u(\eta) F_\eta\right]^T P_\eta \left[B_d(\eta) + \Delta B_d(\eta)\right] \\ \Pi_3 &= \left[B_d(\eta) + \Delta B_d(\eta)\right]^T P_\eta * -\tau I. \end{aligned} \tag{30}$$

I is an identity matrix with appropriate dimensions. The inequality [Equation (28)] can be guaranteed as long as

$$\begin{bmatrix} \Pi_1 & \Pi_2 \\ * & \Pi_3 \end{bmatrix} \le 0 \tag{31}$$

holds.

Here, we introduce a lemma for use in the following sections.

Lemma 3.3[37]: For matrices Γ, H and E with appropriate dimensions and $\Gamma^T = \Gamma$, the following inequality

$$\Gamma + HF(k)E + E^T F(k) H^T \le 0 \tag{32}$$

holds for all $F(k)^T F(k) \le 1$ if and only if there is a positive scalar ϵ such that

$$\Gamma + \epsilon E^T E + \frac{1}{\epsilon} H H^T \le 0. \tag{33}$$

By *Lemma* 3.3, the following sufficient condition can be derived to guarantee the inequality [Equation (31)]:

$$\begin{bmatrix} -X_i & 0 & \left(A_j X_j + B_{uj} Y_j\right)^T & (QX_j)^T & (RY_j)^T & (E_{j1} X_j)^T & 0 \\ * & -\zeta I & \gamma B_{dj}^T & 0 & 0 & 0 & (\gamma E_{j2})^T \\ * & * & \epsilon_j (H_{j1} H_{j1}^T + H_{j2} H_{j2}^T) - X_j & 0 & 0 & 0 & 0 \\ * & * & * & -\gamma Q & 0 & 0 & 0 \\ * & * & * & * & -\gamma R & 0 & 0 \\ * & * & * & * & * & -\epsilon_j I & 0 \\ * & * & * & * & * & * & -\epsilon_j I \end{bmatrix} \le 0, \; j = 1, 2, \tag{34}$$

where $\zeta = \gamma\tau$.

We also need to consider the control input constraints to ensure driving comfort:

$$|u_i(k)| \le u_{i,\max}, \quad i = 1, 2 \tag{35}$$

According to inequality [Equation (26)], we have:

$$x(k)^T X_j^{-1} x(k) \le 1. \tag{36}$$

Therefore, we have:

$$\begin{aligned} \max \|u(k)\|^2 &= \max \| \left(F(\eta)x(k)\right) \|^2 \\ &= \max \|(Y(\eta)X(\eta)^{-1}x(k))\|^2 \\ &= \max \|(Y(\eta)X(\eta)^{-\frac{1}{2}}X(\eta)^{-\frac{1}{2}}x(k))\|^2 \\ &\le \|(Y(\eta)X(\eta)^{-\frac{1}{2}})\|^2 \|X(\eta)^{-\frac{1}{2}}x(k)|^2 \\ &= (Y(\eta)X(\eta)^{-1}Y(\eta))[x(k)^T X(\eta)^{-1}x(k)] \\ &\le Y(\eta)X(\eta)^{-1}Y(\eta). \end{aligned} \tag{37}$$

Considering the Schur complement, the input constraint can be guaranteed by the following LMI if there exists a symmetric matrix U [38]

$$\begin{bmatrix} U & Y_j \\ * & X_j \end{bmatrix} \ge 0, \tag{38}$$

where $U_{ii} \le u_{i,\max}^2$.

To deal with the external disturbance, the concept of RPI is introduced to ensure the closed-loop stability of car-following system. According to the concept of RPI and quadratic boundedness as shown in *Lemma* 3.1, Ω_k is an RPI set if

$$x(k+1|k)^T P_i x(k+1|k) \le x(k|k)^T \mathrm{P}_j\, x(k|k)$$

holds under

$$\frac{d(k)^T d(k)}{\phi^2} \le x(k)^T Q_j^{-1} x(k),$$

where $d(k)^T d(k) \le \phi^2$.

The S-procedure is used to obtain a sufficient condition as follows:

$$x(k+1)^T X_i^{-1} x(k+1) - x(k)^T X_j^{-1} x(k) - \lambda \left[\frac{d(k)^T d(k)}{\phi^2} - x(k)^T X_j^{-1} x(k) \right] \le 0, \tag{39}$$

where λ is a positive scalar belonging to $(0, 1)$.

By *Lemma* 3.3, the above mentioned inequality can be guaranteed by the following matrix: inequality:

$$\begin{bmatrix} (-1+\lambda)X_i & 0 & \left(A_j X_j + B_{uj} Y_j\right)^T & \left(E_{j1} X\right)^T & 0 \\ * & -\frac{\lambda}{\phi^2} I & \left(B_{dj}\right)^T & 0 & \left(E_{j2}\right)^T \\ * & * & \epsilon_j \left(H_{j1} H_{j1}^T + H_{j2} H_{j2}^T\right) - X_j & 0 & 0 \\ * & * & * & -\epsilon_j I & 0 \\ * & * & * & * & -\epsilon_j I \end{bmatrix} \le 0, j = 1, 2. \tag{40}$$

Therefore, the controller design can be summarized as the following:

$$\begin{aligned} &\min_{X_j>0,\epsilon_j>0,Y_j} \zeta \\ &\text{s. t. } (26), (34), (38), (40), \text{and } 0<\lambda<1. \end{aligned} \tag{41}$$

The T-S fuzzy state feedback controller is derived by solving the optimization problem in Equation (40) under parameter uncertainties and external persistent perturbations. The inequality Equation (34) ensures that the cost function $\mathcal{J}_\infty(k)$ is upper-bounded by the Lyapunov function $V(x(k))$, the inequality Equation (38) guarantees that the input constraints are satisfied, and the inequality Equation (40) leads to $x(k) \in \Omega_k$, where Ω_k is an RPI set.

Remark 3.1: Note that ζ is minimized instead of γ in the abovementioned optimization problem. This approach is used because both γ and τ need to be minimized, and a smaller τ implies a higher system performance. We adopt the approach given in Ref.[23] to simultaneously optimize γ and τ by defining $\zeta = \gamma\tau$ in Equation (34). The introduction of the variable λ makes the constraint Equation (40) a bilinear matrix inequality, which can be handled with existing solvers, e.g., PENBMI. The computational load is reduced further by predefining a suboptimal value of λ by trial and error.

Theorem 3.1: The optimization problem Equation (40) has the property of recursive feasibility, that is, a solution will always exist once the problem is initially solvable.

Proof: Implementation of the predictive control strategy based on the T-S fuzzy model requires the constrained optimization problem Equation (40) to be solved at each time instant. Therefore, it is important to guarantee the recursive feasibility of the optimization problem. As an external disturbance is considered, the recursive feasibility is no longer a natural characteristic of the proposed controller. In this study, only the constraint Equation (26) depends on the time instant k, which involves $x(k)$. Therefore, we only need to ensure the feasibility of the constraint Equation (26).

Note that the inequality Equation (26) is equal to $x(k) \in \Omega_k$. The inequality Equation (40) ensures that the set Ω_k is an RPI set, which implies that the inequality Equation (26) is still feasible at the $(k+1)$ time instant. That is, $x(k+1) \in \Omega_{k+1} \in \Omega_k$ is still satisfied. Hence, recursive feasibility is guaranteed. Thus, the proof is completed. □

Theorem 3.2: The closed-loop system in this paper has ISS based on the proposed MPC strategy under an external disturbance.

Proof: It has been proven that the optimization problem Equation (41), once solvable, will always be solvable.

Define the optimal solution at time instant k as $\{\gamma^*, X_j^*, \epsilon_{1j}^*, \epsilon_{2j}^*, Y_j^*, \zeta^*\}$, and $V^*(x(k)) = \sum_{i=1}^2 \eta_i(\theta) x^T(k) P_i^* x(k)$, where $P^* = \gamma^* X_j^{*-1}$. We need to prove that the $V^*(x(k))$ is an ISS-Lyapunov function. Define $\bar{\lambda}$ as the upper bound of eigenvalue of P_η^*, and $\underline{\lambda}$ as the lower bound of the eigenvalue of P_η^*. We can obtain:

$$\underline{\lambda}\|x(k)\|^2 \le V^*(x(k)) \le \bar{\lambda}\|x(k)\|^2. \tag{42}$$

Furthermore, from inequality Equation (24), we can derive the following inequality:

$$V^*(x(k+1)) - V^*(x(k)) \le -x(k)^T Q x(k) - x(k)^T F^{*T} R F^* x(k) + \tau d(k)^T d(k), \tag{43}$$

where $F^* = \sum_{j=1}^2 \eta_i(\theta) Y_j X_j^{-1}$. Therefore, we get

$$V^*(x(k+1)) - V^*(x(k)) \le -x(k)^T Q x(k) + \tau d(k)^T d(k). \tag{44}$$

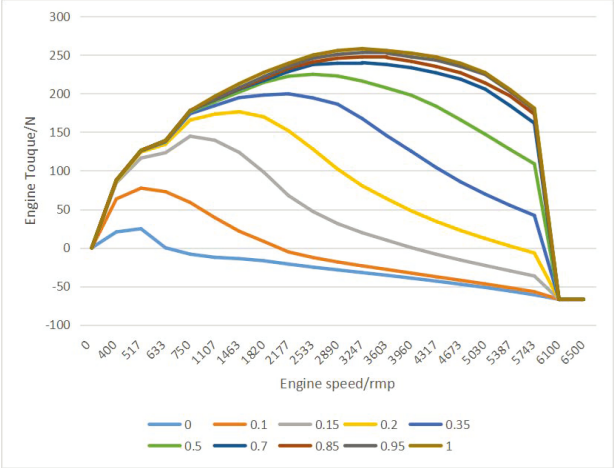

Figure 4. Engine model.

From the inequalities Equation (42), Equation (44) and *Lemma* 3.2, we can conclude that $V(x(k))$ is an ISS-Lyapunov function, and the closed-loop system is ISS. Thus the proof is completed. □

4. LOWER LAYER

According to the vehicle longitudinal motions in the car-following scenario, the lower layer is divided into two blocks for calculating the acceleration throttle opening and the brake pressure, which are designed to realize the desired longitudinal acceleration or deceleration and direct yaw moment. To this end, a logic switch in the lower layer is utilized to implement an accelerating or braking manoeuvre based on the desired longitudinal acceleration a_{des} and the direct yaw moment M_{des} calculated by the T-S fuzzy controller in the upper layer. The vehicle throttle opening or brake pressure on all four wheels can then be obtained.

4.1. Accelerating control

Figure 4 shows the engine speed versus the torque at different throttle openings, which are shown at the bottom. If the engine speed w_e and the desired torque $T_{\text{e,des}}$ are known, the corresponding expected throttle opening σ_{des} is obtained based on this look-up table:

$$\sigma_{\text{des}} = f\left(T_{\text{e,des}}, w_e\right). \tag{45}$$

The vehicle longitudinal dynamics are produced by the combined effect of vehicle traction, wind resistance, and ground resistance. Therefore, the vehicle state depends strongly on the road smoothness and the magnitude of the wind resistance coefficient during cruising. The equivalent air friction during longitudinal driving is

$$F_f = \frac{1}{2}\rho_a C_d A_F \left(r_{\text{eff}} R_p w_e\right)^2, \tag{46}$$

where ρ_a is the air mass density, C_d is the coefficient of air friction, A_F is the windward area of the ego vehicle, R_p is the ratio between the wheel speed w_w and engine speed w_e, and r_{eff} is the effective tire radius.

During vehicle acceleration, the engine torque $T_{\text{e,des}}$ is related to the expected acceleration a_{des} is [39] as

$$T_{\text{e,des}} = \frac{J_e}{R_p r_{\text{eff}}} a_{des} + \left[c_a R_p^3 r_{\text{eff}}^3 w_e^2 + R_p\left(r_{\text{eff}} R_x\right)\right], \tag{47}$$

where $J_e = I_e + I_t + (m r_{\text{eff}}^2 + I_w) R_p^2$ is the effective moment of inertia for the engine side, I_e is the moment of inertia of the engine, and R_x is the sum of all the rolling resistances related to the rolling damping coefficient

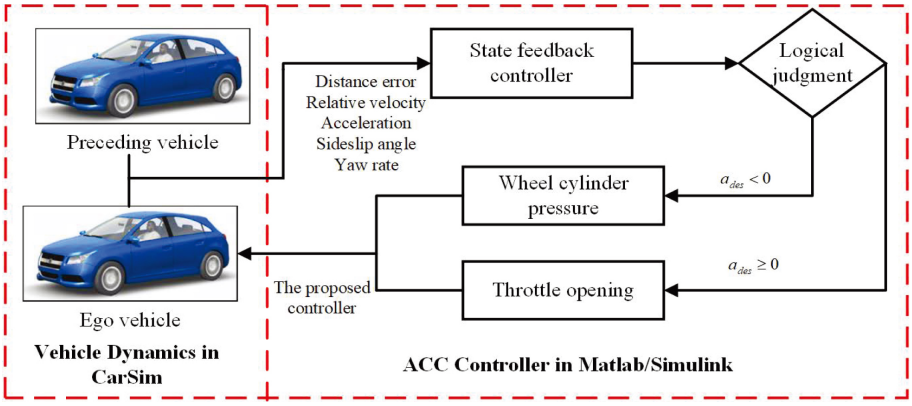

Figure 5. Structure of the car-following systems in Carsim/Simulink joint simulation environment.

f. As $f \in (0.01, 0.04)$, R_x is sufficiently small to be neglected in this study. The following exist:

$$m \gg \frac{I_e}{r_{\text{eff}}^2}, \quad m \gg \frac{I_t}{r_{\text{eff}}^2}, \quad m \gg \frac{I_w}{r_{\text{eff}}^2}. \tag{48}$$

Then, J_e can be rewritten as $J_e = mr_{\text{eff}}^2 R_p^2$. Therefore, Equation (47) can be rewritten as follows:

$$T_{\text{e,des}} = R_p r_{\text{eff}}(ma_{des} + F_f). \tag{49}$$

Thus, the corresponding expected throttle opening σ_{des} can be obtained from the inverse dynamic relation.

4.2. Braking control

During vehicle braking, the desired acceleration a_{des} and the yaw moment M_{des} given by the upper controller can be used to determine the longitudinal tire force from the following equation[40]:

$$\begin{cases} -ma_{des} = F_{fl} + F_{fr} + F_{rl} + F_{rr} \\ M_{des} = \left(F_{fr} + F_{rr} - F_{fl} - F_{rr}\right) b \\ F_{rl} = \frac{l_f g + a_2 h}{l_r g - a_2 h} F_{fl} \\ F_{rr} = \frac{l_f g + a_2 h}{l_r g - a_2 h} F_{fr} \end{cases}, \tag{50}$$

where b is the distance between the right and left wheels and h is the height of the centre of mass of the vehicle.

Equation (50) can be solved for the longitudinal force on the four wheels. Then, we can calculate the hydraulic pressure wheel cylinder from the following equation:

$$P_{B,ij} = \frac{r_w}{K_B} F_{ij}, \tag{51}$$

where r_w denotes the efficient wheel radius and K_B represents the pressure constant of a single wheel.

5. SIMULATION VALIDATIONS

CarSim/Simulink joint simulations are conducted to verify the effectiveness of the proposed predictive control based on the T-S fuzzy model. The structure of the car-following system is shown inFigure 5. The proposed controller is derived by solving the optimization problem in Equation (41) with the YALMIP toolbox introduced in[41] within the MATLAB/Simulink environment, where the vehicle model and road conditions are provided by the CarSim platform. We simulate a severe riding condition by considering a road with snow cover on the left-hand side of the vehicle. The test scenario is shown in Figure 6.

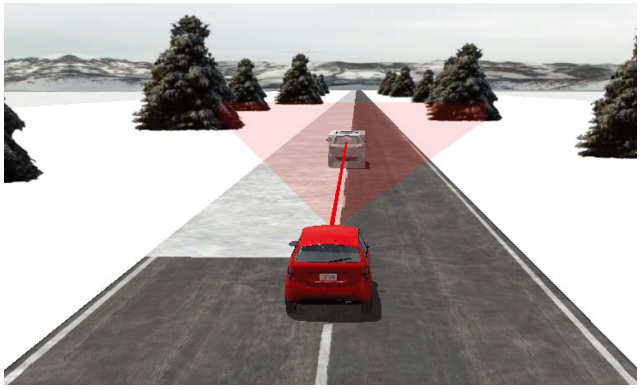

Figure 6. The scenario setting in Carsim platform.

Table 1. Parameters in the simulation model

Parameters	Values
m(kg)	1110
I_z (kg/m^2)	1343.1
τ_0(s)	0.25
b(mm)	1480
h(mm)	350
r_{eff} (mm)	298
t_0(s)	2
$C_{\alpha f}$ (N/rad)	66900
$C_{\alpha f}$ (N/rad)	62700

The B-Class Hatchback car is selected as the ego vehicle to be controlled, and its physical parameters are given in Table 1. We illustrate the advantages of the methods developed in this study by comparison against a conventional controller design without vehicle lateral stabilization.

The preceding vehicle is set to be 60m ahead of the ego vehicle at the start of the simulation. We compare the simulation results for two different speed profiles: (1) a ramp speed profile and (2) a *cosine* speed profile.

5.1. Case I: ramp speed profile

The initial condition in this case is a zero relative velocity between vehicles: we assume $v_1 = v_2 = 25$ m/s and a desired distance between vehicles at standstill $d_0 = 10$ m. Considering the nonlinearity of the lateral forces between the tires and the road surface, the cornering stiffness for the front and rear tires is set to (66900 ± 10000) N/rad and (62700 ± 10000) N/rad, respectively. The upper bound on the control input for the vehicle acceleration is set to 2 m^2/s. Substituting the corresponding parameters into the system model Equations 8-17 easily yields the system matrices. According to *Remark 3.1*, λ is selected as 0.01 in this study.

The optimization problem given by Equation (41) is solved recursively to yield the closed-loop system responses in the CarSim/Simulink joint simulation environment, which are shown in Figure 7. In Figure 7A, the blue and red curves represent the speeds of the preceding and ego vehicles, respectively. Figure 7B and Figure 7C show the errors in the longitudinal velocity and between the desired and actual longitudinal distances, respectively, where the maximum velocity error is 5.9 m/s at 4.5 s and the maximum distance error is 3.8 m at 19.7 s. Figure 7 shows that although the preceding vehicle velocities vary in the range [10, 25] m/s, the predictive controller based on the T-S fuzzy model guarantees the velocity and the desired safe following distance for the ego vehicle under the considered extreme road conditions.

To further demonstrate the advantages of the proposed car-following controller design, Figure 8 shows the

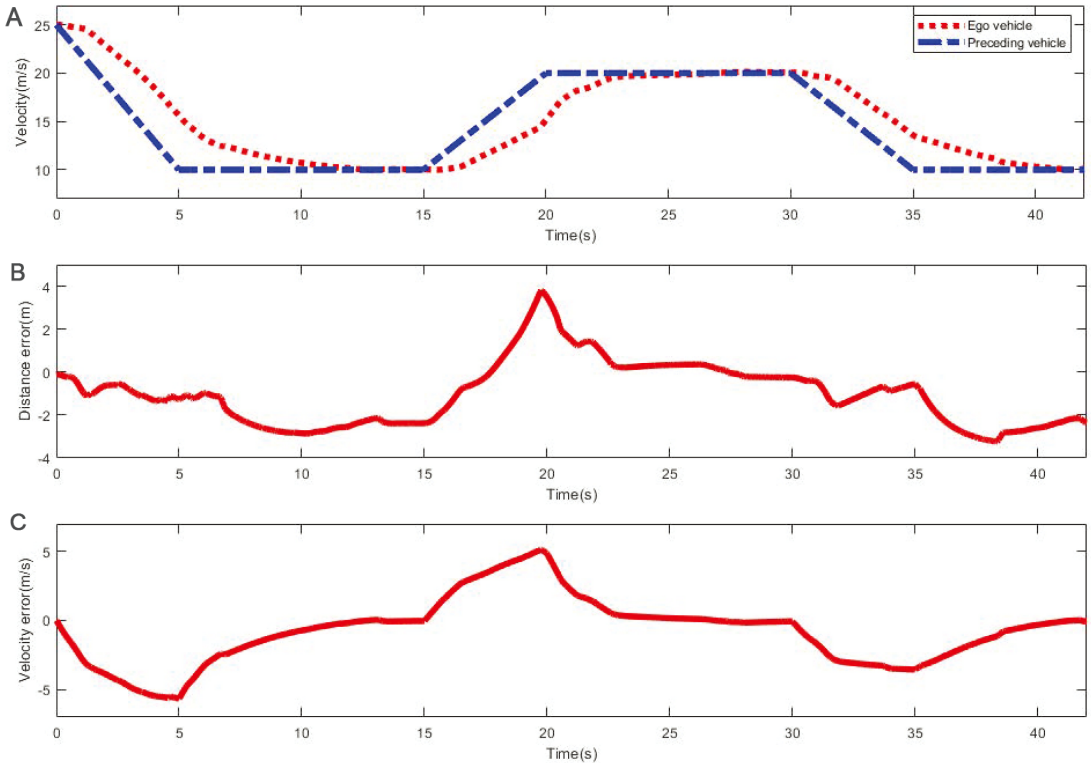

Figure 7. (A) Velocity of the preceding and ego vehicle; (B) Relative velocity; (C) Relative distance.

responses of sideslip angles and yaw rate (which reflect the lateral stability of the vehicle) obtained using the conventional controller (without consideration of the lateral stability) and the controller developed in this study. Figure 8 shows that compared to the results obtained using the conventional controller, the sideslip angle and yaw rate obtained using the proposed controller are smaller in magnitude, indicating improved vehicle stability.

5.2. Case II: *cosine* speed profile

In this case, the initial velocities of the preceding and ego vehicles and the relative distance are set to 25 m/s and 50 m, respectively. Figure 9A shows the *cosine*-function speed profile of the preceding vehicle and the simulation results as a blue dash-dotted curve. In Figure 9A, the red curve represents the closed-loop response for the speed of the ego vehicle. Figure 9B and Figure 9C show the errors in the longitudinal velocity and between the desired and actual distances, respectively. Figure 9D shows the acceleration of the ego vehicle, which satisfies the input constraint given by $|a_{des}| \leq 2\,\mathrm{m}^2/\mathrm{s}$.

It can be concluded from Figure 9 that the proposed method completes the car-following task with satisfactory performance for a time-varying velocity. Figure 10 shows the dynamics of the sideslip angle, yaw rate, and vehicle lateral offset. Figure 10C clearly shows that the lateral offset increases when the car-following manoeuvre is conducted under the conventional MPC without lateral stabilization. These three aspects of the results show that the proposed car-following controller outperforms the conventional controller in terms of guaranteeing both satisfactory tracking performance and lateral stability of the vehicle in emergency scenarios.

6. CONCLUSION

In this paper, a T-S fuzzy model-based predictive adaptive cruise controller is designed while ensuring vehicle lateral stability by integrating the ACC system with a direct yaw moment control system. To consider varia-

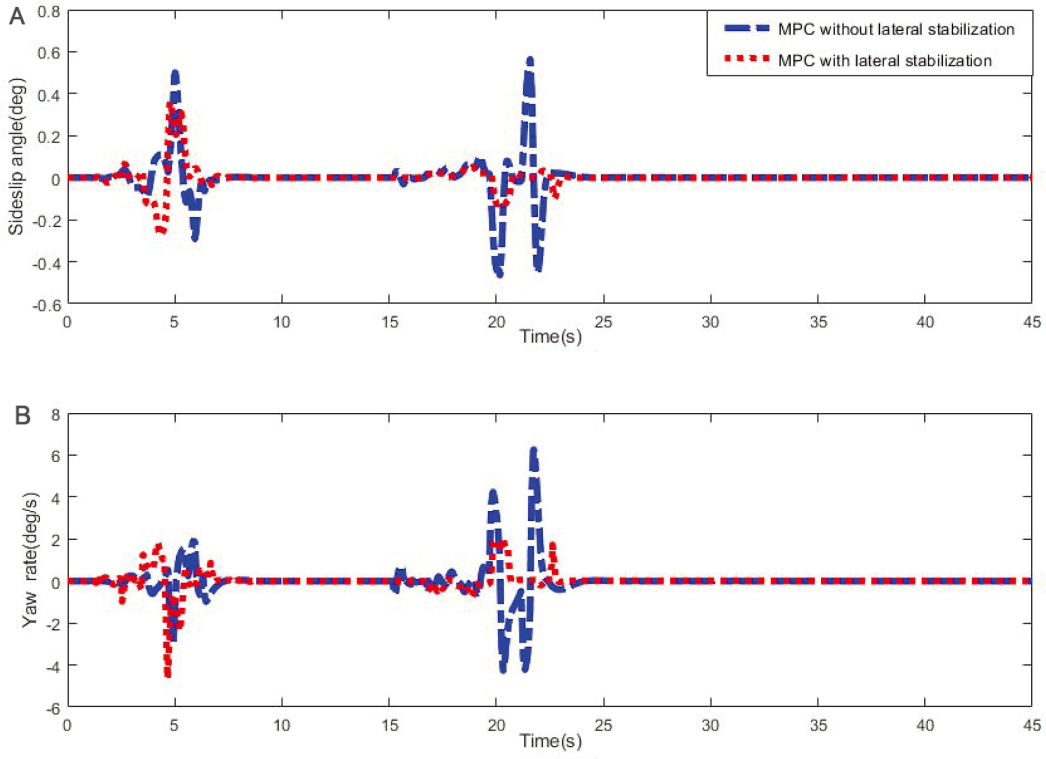

Figure 8. (A) Vehicle sideslip angle of the ego vehicle in Case I. (B) Vehicle yaw rate of the ego vehicle in Case I.

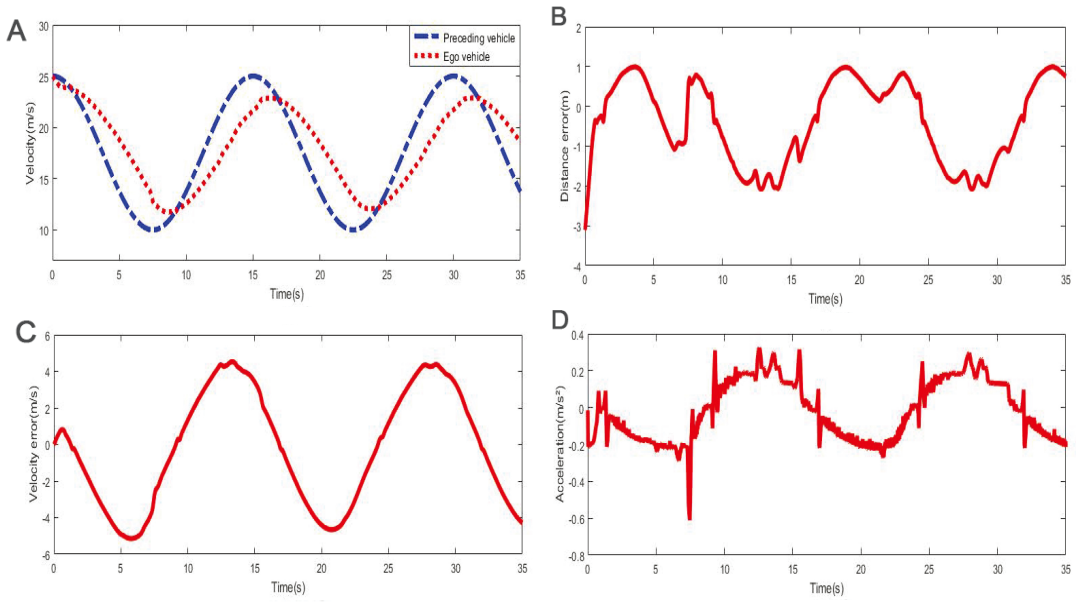

Figure 9. (A) Velocity of preceding and ego vehicle; (B)Relative velocity; (C) Relative distance; (D)Ego vehicle acceleration.

tions in the preceding vehicle velocity and road surface conditions, the adaptive cruise control is formulated as a tracking control problem of a T-S fuzzy system subject to parameter uncertainties and external persistent perturbations. Then, a robust positively invariant set is introduced to develop an admissible T-S fuzzy controller by solving a min-max optimization problem under a series of linear matrix inequality constraints.

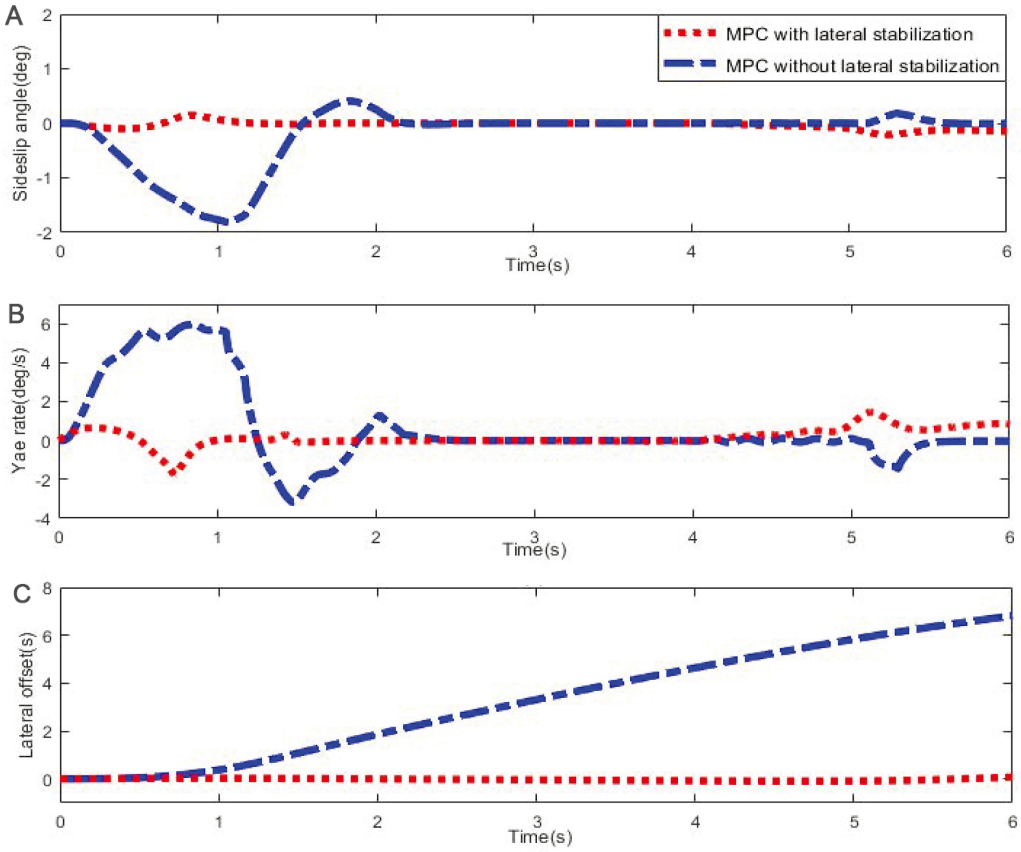

Figure 10. (A) Sideslip angle in Case II; (B) Yaw rate in Case II; (C) Vehicle lateral offset in Case II.

CarSim/Simulink joint simulation results verify that the developed method exhibits good performance for vehicle tracking and ensures vehicle lateral stability.

DECLARATIONS

Authors' contributions

Made substantial contributions to conception and design of the study and performed data analysis and interpretation: Zhang C, Wei X

Performed data acquisition, as well as provided administrative, technical, and material support: Wang Z, Zhang H, Guo X

Availability of data and materials

In this paper, we have detailed a modelling procedure and the construction of an optimization problem with linear matrix inequality constraints to design a T-S fuzzy model predictive controller. The physical parameters of the vehicle are provided in the section on the simulations. The effectiveness of the developed method has been demonstrated using the MATLAB/CarSim joint simulation platform. There are no additional data or materials associated with this study.

Financial support and sponsorship

This work was supported in part by National Key R&D Program of China under Grant No: 2020AAA0108100; in part by Shanghai Natural Science Foundation under Grant No: 21ZR1482300 and 19ZR1461400; and in part by the Fundamental Research Funds for the Central Universities.

Conflicts of interest

All authors declared that there are no conflicts of interest.

Ethical approval and consent to participate

Not applicable.

Consent for publication

All the authors have consented to the publication of this manuscript.

Copyright

REFERENCES

1. Hasenjäger M, Heckmann M, Wersing H. A survey of personalization for advanced driver assistance systems. *IEEE Trans Intell Veh* 2020;5:335–44. DOI
2. Li L, Wen D, Zheng N, Shen L. Cognitive cars: a new frontier for ADAS research. *IEEE Trans Intell Trans Syst* 2012;13:395–407. DOI
3. Muresan MP, Nedevschi S. Multimodal sparse LIDAR object tracking in clutter. In: 2018 IEEE 14th International Conference on Intelligent Computer Communication and Processing (ICCP); 2018. pp. 215–21. DOI
4. Cheng J, Ju M, Zhou M, Liu C, Gao S, et al. A dynamic evolution method for autonomous vehicle groups in a highway scene. *IEEE Int Things J* 2022;9:1445–57. DOI
5. Yuan T, Krishnan K, Duraisamy B, Maile M, Schwarz T. Extended object tracking using IMM approach for a real-world vehicle sensor fusion system. In: 2017 IEEE International Conference on Multisensor Fusion and Integration for Intelligent Systems (MFI); 2017. pp. 638–43. DOI
6. Guo C, Meguro J, Kojima Y, Naito T. A multimodal ADAS system for unmarked urban scenarios based on road context understanding. *IEEE Trans Intell Transp Syst* 2015;16:1690–704. DOI
7. Hosseinnia SH, Tejado I, Milanés V, Villagrá J, Vinagre BM. Experimental application of hybrid fractional-order adaptive cruise control at low speed. *IEEE Trans Contr Syst Techn* 2014;22:2329–36. DOI
8. Wang X, Chen M, Zhu M, Tremont P. Development of a kinematic-based forward collision warning algorithm using an advanced driving simulator. *IEEE Trans Intell Trans Syst* 2016;17:2583–91. DOI
9. Pananurak W, Thanok S, Parnichkun M. Adaptive cruise control for an intelligent vehicle. In: 2008 IEEE International Conference on Robotics and Biomimetics; 2009. pp. 1794–99. DOI
10. Asadi B, Vahidi A. Predictive cruise control: utilizing upcoming traffic signal information for improving fuel economy and reducing trip time. *IEEE Trans Contr Syst Techn* 2011;19:707–14. DOI
11. Chiang HH, Wu SJ, Perng JW, Wu BF, Lee TT. The human-in-the-loop design approach to the longitudinal automation system for an intelligent vehicle. *IEEE Trans Syst, Man, Cybern - Part A: Syst Humans* 2010;40:708–20. DOI
12. Akhegaonkar S, Nouvelière L, Glaser S, Holzmann F. Smart and green ACC: energy and safety optimization strategies for EVs. *IEEE Trans Syst, Man, Cybern: Syst* 2018;48:142–53. DOI
13. Li S, Li K, Rajamani R, Wang J. Model Predictive Multi-Objective Vehicular Adaptive Cruise Control. *IEEE Trans Contr Syst Technol* 2011;19:556–66. DOI
14. Hu J, Zhu J, Lei G, Platt G, Dorrell DG. Multi-objective model-predictive control for high-power converters. *IEEE Trans Energy Conv* 2013;28:652–63. DOI
15. Bageshwar VL, Garrard WL, Rajamani R. Model predictive control of transitional maneuvers for adaptive cruise control vehicles. *IEEE Trans Veh Technol* 2004;53:1573–85. DOI
16. Li SE, Jia Z, Li K, Cheng B. Fast online computation of a model predictive controller and its application to fuel economy–oriented adaptive cruise control. *IEEE Trans Intell Trans Syst* 2015;16:1199–209. DOI
17. Corona D, De Schutter B. Adaptive cruise control for a SMART car: a comparison benchmark for MPC-PWA control methods. *IEEE Trans Contr Syst Techn* 2008;16:365–72. DOI
18. Moser D, Schmied R, Waschl H, del Re L. Flexible spacing adaptive cruise control using stochastic model predictive control. *IEEE Trans Contr Syst Techn* 2018;26:114–27. DOI
19. Li SE, Guo Q, Xu S, Duan J, Li S, et al. Performance enhanced predictive control for adaptive cruise control system considering road elevation information. *IEEE Trans Intell Veh* 2017;2:150–60. DOI
20. Gao B, Cai K, Qu T, Hu Y, Chen H. Personalized adaptive cruise control based on online driving style recognition technology and model predictive control. *IEEE Trans Veh Techn* 2020;69:12482–96. DOI
21. Yang D, Zong G, Su SF. $\mathcal{H}_\infty$ tracking control of uncertain Markovian hybrid switching systems: a fuzzy switching dynamic adaptive control approach. *IEEE Trans Cybern* 2022;52:3111–22. DOI
22. Xie X, Wei C, Gu Z, Shi K. Relaxed resilient fuzzy stabilization of discrete-time Takagi-Sugeno systems via a higher order time-variant balanced matrix method. *IEEE Trans Fuzzy Syst* 2022:1–1. DOI

23. Yang W, Feng G, Zhang T. Robust model predictive control for discrete-time Takagi–sugeno fuzzy systems with structured uncertainties and persistent disturbances. *IEEE Trans Fuzzy Syst* 2014;22:1213–28. DOI
24. Nguyen AT, Taniguchi T, Eciolaza L, Campos V, Palhares R, et al. Fuzzy control systems: past, present and future. *IEEE Comput Intell Mag* 2019;14:56–68. DOI
25. Nguyen AT, Rath J, Guerra TM, Palhares R, Zhang H. Robust set-invariance based fuzzy output tracking control for vehicle autonomous driving under uncertain lateral forces and steering constraints. *IEEE Trans Intell Transp Syst* 2021;22:5849–60. DOI
26. Zhang C, Lam HK, Qiu J, Qi P, Chen Q. Fuzzy-model-based output feedback steering control in autonomous driving subject to actuator constraints. *IEEE Trans Fuzzy Syst* 2021;29:457–70. DOI
27. Nguyen AT, Sentouh C, Zhang H, Popieul JC. Fuzzy static output feedback control for path following of autonomous vehicles with transient performance improvements. *IEEE Trans Intell Transp Syst* 2020;21:3069–79. DOI
28. Zhang D, Wang J. A curving ACC system with coordination control of longitudinal car-following and lateral stability. *Veh Syst Dyn* 2012;50:1085–102. DOI
29. Liu F, Chen Y. Improved model predictive control for cooperative adaptive cruise control subject to actuator delay. In: 2017 Chinese Automation Congress (CAC); 2017. pp. 4747–22. DOI
30. Zhang H, Zhang X, Wang J. Robust gain-scheduling energy-to-peak control of vehicle lateral dynamics stabilisation. *Veh Syst Dyn* 2014;52:309–40. DOI
31. Baffet G, Charara A, Dherbomez G. An observer of tire–road forces and friction for active security vehicle systems. *IEEE/ASME Trans Mechatr* 2007;12:651–61. DOI
32. Rajamani R. Vehicle dynamics and control. Springer Science & Business Media; 2011.
33. Nguyen A, Sentouh C, Zhang H, Popieul J. Fuzzy static output feedback control for path following of autonomous vehicles with transient performance improvements. *IEEE Trans Intell Transp Syst* 2020;21:3069–79. DOI
34. Yang W, Gao J, Feng G, Zhang TJ. An optimal approach to output-feedback robust model predictive control of LPV systems with disturbances. *Int J Rob Nonl Contr* 2016;26. DOI
35. Jiang ZP, Wang Y. Input-to-state stability for discrete-time nonlinear systems. *Automatica* 2001;37:857–69. DOI
36. Magni L, Raimondo DM, Scattolini R. Regional input-to-state stability for nonlinear model predictive control. *IEEE Trans Autom Contr* 2006;51:1548–53. DOI
37. Xie L, Fu M, de Souza CE. H/sub infinity/control and quadratic stabilization of systems with parameter uncertainty via output feedback. *IEEE Trans Autom Contr* 1992;37:1253–56. DOI
38. Kothare MV, Balakrishnan V, Morari M. Robust constrained model predictive control using linear matrix inequalities. *Automatica* 1996;32:1361–79. DOI
39. Costello GA. Theory of wire rope. New York, NY: Springer New York; 1997. DOI
40. Cheng S, Li L, Guo H, Chen Z, Song P. Longitudinal collision avoidance and lateral stability adaptive control system based on MPC of autonomous vehicles. *IEEE Trans Intell Trans Syst* 2020;21:2376–85. DOI
41. Lofberg J. YALMIP : a toolbox for modeling and optimization in MATLAB. In: 2004 IEEE International Conference on Robotics and Automation (IEEE Cat. No.04CH37508); 2004. pp. 284–89. DOI

Wang *et al. Intell Robot* 2022;2(4):391-406
DOI: 10.20517/ir.2022.25

Intelligence & Robotics

Review

Open Access

Intelligent feature extraction, data fusion and detection of concrete bridge cracks: current development and challenges

Di Wang[1], Simon X. Yang[2]

[1]School of Information Science and Engineering, Chongqing Jiaotong University, Chongqing 400074, China.
[2]Advanced Robotics and Intelligent Systems (ARIS) Lab School of Engineering, University of Guelph, Guelph ON N1G 2W1, Canada.

Correspondence to: Dr. Di Wang, School of Information Science and Engineering, Chongqing Jiaotong University, No. 66, Xuefu Avenue, Nan'an District, Chongqing 400074, China. E-mail: diwang@cqjtu.edu.cn

How to cite this article: Wang D, Yang SX. Intelligent feature extraction, data fusion and detection of concrete bridge cracks: current development and challenges. *Intell Robot* 2022;2(4):391-406. https://dx.doi.org/10.20517/ir.2022.25

Received: 10 Aug 2022 **First Decision:** 3 Oct 2022 **Revised:** 30 Oct 2022 **Accepted:** 8 Dec 2022 **Published:** 23 Dec 2022

Academic Editor: Guang Chen **Copy Editor:** Ying Han **Production Editor:** Ying Han

Abstract

As a common appearance defect of concrete bridges, cracks are important indices for bridge structure health assessment. Although there has been much research on crack identification, research on the evolution mechanism of bridge cracks is still far from practical applications. In this paper, the state-of-the-art research on intelligent theories and methodologies for intelligent feature extraction, data fusion and crack detection based on data-driven approaches is comprehensively reviewed. The research is discussed from three aspects: the feature extraction level of the multimodal parameters of bridge cracks, the description level and the diagnosis level of the bridge crack damage states. We focus on previous research concerning the quantitative characterization problems of multimodal parameters of bridge cracks and their implementation in crack identification, while highlighting some of their major drawbacks. In addition, the current challenges and potential future research directions are discussed.

Keywords: Intelligent detection, crack detection, deep learning, data fusion, feature extraction

1. INTRODUCTION

As a pivotal project for economic development and residents' lives and travel, bridges have an irreplaceable role in modern transportation. Bridge structures inevitably incur defects such as pores and cracks when they

are affected by overload, temperature change, reinforcement corrosion, construction defects and other factors[1]. If cracks cannot be detected and maintained in a timely manner, traffic safety will gradually be affected, with the potential for bridge collapse and related accidents. Once bridge collapse occurs, it will reduce its structural bearing capacity, which will affect the reliability and safety of the structure, causing immense social repercussions[2-4].

In engineering practice, the health monitoring of bridge cracks has attracted the attention of relevant national departments and research institutions[5,6], corresponding norms and standards have been issued, and the monitoring methods and monitoring parameters for bridge deformation and cracks have been clearly specified.

In recent years, there have been many significant developments in research on the detection of concrete bridge cracks[7-15]. It has been shown that the applications of machine learning in bridge cracks have achieved good results[16-18]. Some studies utilize convolutional neural networks (CNNs) to detect and segment cracks in civil infrastructure with multiple objects[19-23]. It is significant to carry out data-driven research on feature extraction, data fusion and intelligent detection of concrete bridge cracks, which could provide not only a scientific basis for intelligent maintenance of bridges but also data support and a theoretical basis for bridge defect detection, which could have an important role in improving social and economic benefits.

After more than 20 years of scientific research and practice, health monitoring systems have been installed on at least 300 bridges in China. The health monitoring system of a long-span bridge is composed of at least dozens or even hundreds of sensor measuring points. Therefore, numerous monitoring data have been accumulated.

As crack evolution is a gradual and multiscale dynamic process, research is challenging to some extent. There are some common technical difficulties, which will be described from the following three levels:

(1) Feature extraction of multimodal parameters

The characterization information related to bridge cracks includes bridge crack shape information, structural mechanics index information, and crack environment information. Bridge crack shape information comprises the multimodal parameters of bridge cracks, such as the length, width and depth of cracks. Structural mechanics index information consists of the dynamic and static elastic modulus, compressive strength, and stress distribution. Crack environment information includes the load, temperature, humidity, and foundation settlement.

From the level of feature extraction for multimodal parameters of bridge cracks, the characterization information of bridge cracks has multiscale and diversity, which makes it difficult to extract multimodal parameter characteristics. The bridge service environment is complex and changeable, and the crack formation mechanism of concrete bridges varies, which generates multiscale and diverse characterization information. The large amount of information hinders feature extraction.

Due to the influence of background interference information, equipment accuracy, data acquisition mode, signal propagation path and propagation medium, there is considerable redundancy in the data, resulting in a weak effective signal in the monitored multimodal data and difficulty in extracting its sensitive features.

(2) Multisource heterogeneous data fusion representation of bridge cracks

Different kinds of data, such as the length of a bridge crack, the load, and the environmental humidity, belong to multisource heterogeneous data.

From the level of description for the bridge crack damage state, it is difficult to describe the damage evolution state of bridge cracks due to the large amount of multisource heterogeneous data. When bridge cracks are initially generated, the impact on the bridge is small, and the state change of each indicator is not obvious under the same conditions.

Due to the large variety, quantity, variation in sampling methods and many random interference factors of the sensors, the quality of the acquired data is reduced, and the monitoring data are uncertain and low-density, which makes it difficult for the collected data to accurately and pertinently reflect the evolution of the bridge crack.

(3) Intelligent detection methods of bridge cracks

From the level of diagnosis for the bridge crack damage state, the characterization information of bridge cracks is mixed and weak, so it is difficult to scientifically diagnose them. Due to the diversity of monitoring equipment, the diversity of monitoring methods and the variability of monitoring locations, the monitoring data show the characteristics of multimodal, strong correlation and high dimension, which makes the crack information extremely complex, highly mixed and weak separability. It is difficult to analyze the monitoring data and to scientifically describe and diagnose the cracks of concrete bridges. Additionally, the deterioration trend of cracks cannot be scientifically predicted.

By analyzing the feature extraction method of crack multimodal data, the problem of difficult multimodal parameter feature extraction due to the multiscale and diversity of characterization information can be solved. By investigating the multisource heterogeneous data fusion representation of cracks, the difficulty in describing the damage evolution state due to the large amount of multisource heterogeneous data can be addressed. By examining the intelligent prediction model of crack deterioration trends, the problem of difficult scientific diagnosis due to the overlapping and weak separability of bridge crack characterization information can be solved.

The remainder of the article is organized as follows: Section 2 describes the common difficulties in research on feature extraction, data fusion and the detection of concrete bridge cracks. The global research status from three aspects is elaborated and analyzed in Section 3. Section 4 summarizes the principal concluding remarks of the current research with a statement about its strengths and limitations. Figure 1 shows the research framework.

2. RESEARCH STATUS

Research on concrete bridges mainly includes three key aspects: feature extraction of multimodal data, fusion representation of multisource heterogeneous data, and intelligent detection models of bridge cracks. The review of the global research status and development trends mainly focuses on these three aspects.

2.1. Research status of multimodal data feature extraction of bridge cracks

Although some nondestructive methods, including the ultrasonic pulse[24,25] and elastic wave[26-28], have achieved good results for bridge crack detection, feature extraction from the multimodal data of bridge cracks remains challenging.

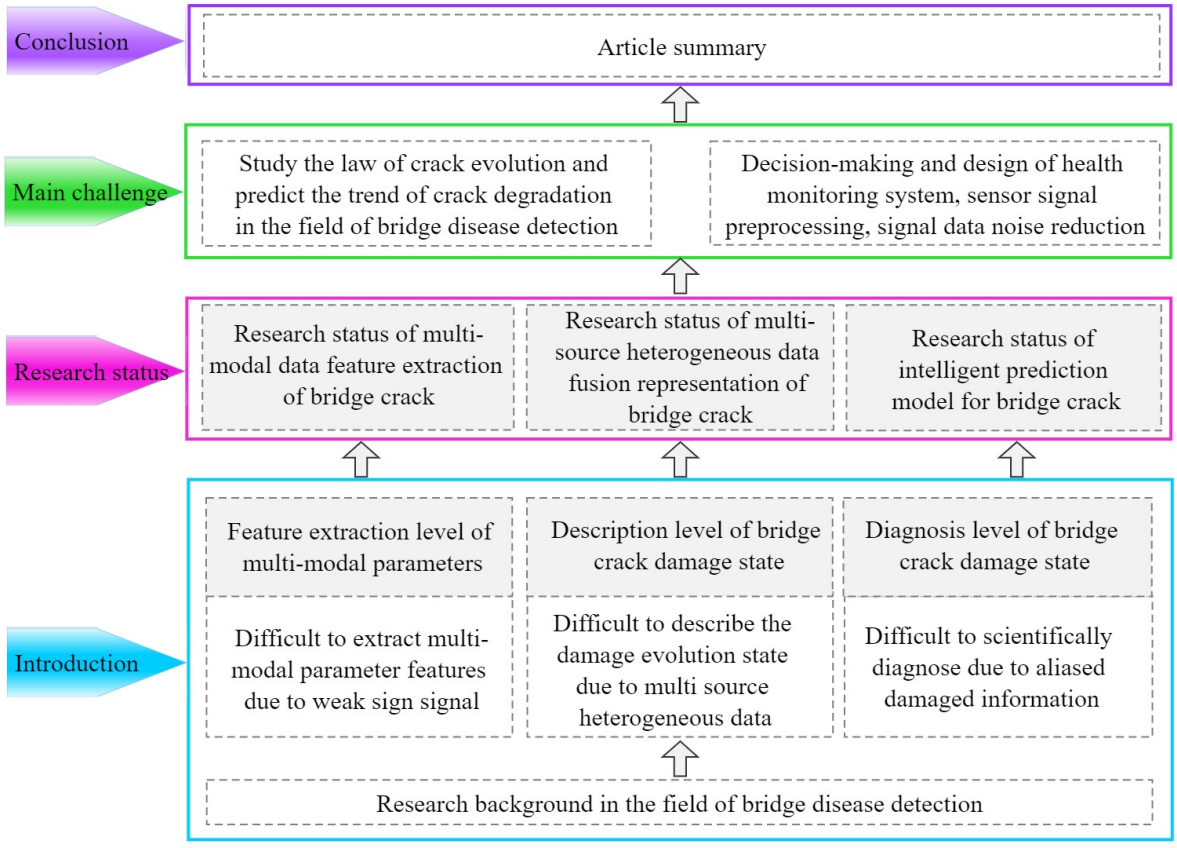

Figure 1. Research framework.

The use of intelligent information processing methods to remove background noise, capture multiscale and diverse representation information, and extract its related sensitive features is the basis for detecting concrete bridge cracks.

In the aspect of feature extraction for concrete bridge cracks, the traditional classical methods include principal component analysis (PCA), sparse decomposition, wavelet transform (WT), and adaptive neural fuzzy inference system (ANFIS).

PCA obtains different principal components via the matrix transformation of signals, arranges the sizes of the principal components according to the variance, and compares the contribution rate of each component with the threshold value, thus realizing effective feature extraction[29,30]. In the research on concrete structure crack recognition based on multiple image features, Yu *et al.* collected 1200 bridge crack images and employed integral projection and PCA to extract effective features sensitive to the crack for crack edge detection[31]. Mei *et al.* collected acceleration data from all the vehicles within a certain period and extracted the transformed features that are related to bridge damage with Mel-frequency cepstral coefficients and PCA to identify the damage by comparing the distributions of these transformed features[32]. PCA is a widely utilized method to remove noise and extract effective features, but it cannot accurately analyze the real subspace structure of data.

Sparse decomposition[33] is different from the traditional feature extraction method. Sparse decomposition decomposes noisy signals on redundant dictionaries to achieve feature extraction. In the research of bridge crack identification, Li *et al.* adopted a self-learning algorithm to extract scale invariant features from 27,471 unlabeled bridge pavement crack images, adopted an improved sparse coding representation to obtain a feature dictionary, adopted a spatial pyramid pooling method for feature extraction, and then employed a linear support vector machine (SVM) classifier for crack identification[34]. Wang *et al.* collected hundreds of concrete crack images and proposed a fast detection method for concrete cracks based on L2 sparse representation[35]. To suppress the noise disturbances, discrete cosine transformation is applied to extract the frequency-domain characteristics of the crack and non-crack image regions. The established complete dictionary was used to quickly calculate its sparse coefficient and effectively select candidate cracks via a pooling operation. Sparse decomposition can be succinctly expressed as a linear combination of several bases, more comprehensively and carefully characterize some features covered by a signal and more effectively separate the signal and noise. However, sparse decomposition involves a vast amount of computation and computational complexity.

The WT is mainly based on the different distributions in the frequency domain of the noise and signals and decomposes a noisy signal into multiple scales. Then, the wavelet coefficients belonging to the noise are removed at each scale, while the wavelet coefficients belonging to the signal are retained and enhanced. After wavelet denoising, the signal is reconstructed to achieve effective feature extraction[36]. Nguyen *et al.* measured displacement signals with four separate measurement channels through a sensor system, where the displacement signals were simultaneously transmitted at a sampling speed of 100 samples per second[37]. Then, the WT method was applied to the original deflection signals to decompose the signals into elements and to eliminate interference signals, which extracts the features of multiple cracks under the action of moving loads and improves the sensitivity and accuracy in the identification process. In the study of the finite element model of a simply supported beam with a transverse crack, Nigam *et al.* employed the WT, which uses the deflected edge as input for identifying the crack location in the beam, and obtained a good detection effect[38]. Because WT retains most of the wavelet coefficients of the signal, the image details can be well preserved after noise reduction. As the abrupt part of the signal will not be damaged during noise reduction, it has a good denoising effect. However, since different signals are applicable to different wavelet bases, it is difficult to identify the optimal wavelet base.

The ANFIS[39,40] organically combines fuzzy logic inference and neural networks and performs self-adaptive learning on fuzzy experience and knowledge while applying reasoning similar to the human brain to eliminate noise and interference and to extract feature information[41,42]. Bilir *et al.* applied the results of free shrinkage tests conducted to determine the length changes and ring tests performed to determine the restrained drying shrinkage cracks for predicting the crack widths of granulated blast furnace slag fine aggregate mortars with ANFIS on 456 data and used the replacement ratios, drying time and free shrinkage length changes as inputs and crack width as output to predict the shrinkage cracking of the mortar types[43]. The ANFIS uses the neural network self-learning ability and fuzzy logic reasoning ability to extract fuzzy rules from the dataset and calculates the optimal parameters of the membership function to adaptively mine the sensitive features in the data.

With the rapid development and wide application of artificial intelligence and deep learning, an increasing number of deep learning methods have been applied to concrete bridge crack detection, especially in crack feature extraction[44,45]. In research on the automatic classification of concrete structure crack damage based on cascade generalized neural networks, Guo *et al.* employed 10,000 cracked and uncracked images from wall images and pavement images with a splitting ratio for datasets of 8:2 and proposed a cascade broad

neural network for concrete structural crack damage classification, where the multilevel cascade classifier was utilized to extract the characteristics of concrete cracks and achieved an accuracy of 97.9%[15]. Zheng *et al.* adopted a model based on a CNN to amplify and extract the features for 5000 concrete crack images and analyzed the morphological and geometric indices of cracks through the training of building surface data such as roads, bridges, houses and dams, while achieving the highest crack detection accuracy of 98% and the average detection accuracy of 87%[46]. Xu *et al.* proposed an end-to-end crack detection model based on a CNN for 2068 bridge crack images using only images and image labels as input and extracted multiscale crack feature information by using cavity convolution and pooling methods, thus reducing the computational complexity and achieving a high recognition rate (96.37%)[47]. Teng *et al.* applied 11 well-known CNN models as the feature extractor of YOLOv2 for crack detection with 990 RGB bridge crack images, providing a basis for rapid and accurate crack detection of concrete structures, and achieved a high precision of 0.89 and a fast computing speed[48].

The self-attention mechanism is a model in deep learning that has been widely applied in natural language processing tasks in recent years. The idea of attention is to filter out a small amount of important information from a large amount of information and focus on this important information, disregarding most of the unimportant information. The larger the weight, the more focused the corresponding feature, where the weight represents the importance of the feature. The self-attention mechanism reduces the dependence on external information and is better at capturing the internal correlations of data or features.

A schematic diagram of the self-attention mechanism is shown in Figure 2. In the figure, three multimodal features, such as the depth of the crack, the load, and the environmental humidity, are used as input, and the output is their correlation information. The feature vectors of a^1, a^2 *and* a^3, which have certain meanings, are obtained from the preprocessing of the three multimodal features. They are respectively multiplied by three weight vectors (w^q, w^k, and w^v) to obtain three corresponding vectors (q^i, k^i, v^i, and i denotes the number of features). The following process can be divided into three steps. Firstly, the similarity calculation of q^i and k^i is performed to obtain the weight of feature. The calculation formula is as follows

$$\alpha_{i,j} = q^i k^j \quad i = 1,2,3, \tag{1}$$

where $\alpha_{i,j}$ denotes the weight. Then the softmax function is used to normalize the weight of each feature. The normalized weight can be calculated by

$$\hat{\alpha}_{i,j} = \frac{e^{\alpha_{i,j}}}{\sum_{j=1}^{3} e^{\alpha_{i,j}}} \quad i = 1,2,3, \tag{2}$$

where $\hat{\alpha}_{i,j}$ denotes the normalized weight. Finally, a weighted sum operation is performed on the normalized weights and each corresponding vector (V^i) to obtain their corresponding outputs. The calculation method is as follows

$$b^i = \sum_{j=1}^{3} \hat{\alpha}_{i,j} v^j \quad i = 1,2,3, \tag{3}$$

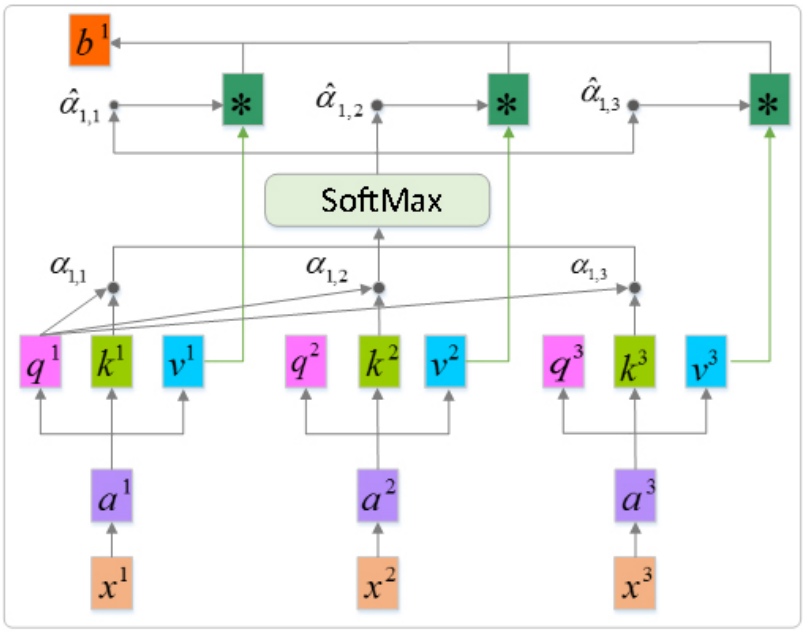

Figure 2. Schematic of the self-attention mechanism.

where b^i contains the relevant information among the three input features. Through this way, the self-attention mechanism effectively assigns weight coefficients via the degree of similarity relationship between two feature vectors and quickly extracts relevant information among multimodal parameters.

Pan *et al.* built a spatial-channel hierarchical network with a base net visual geometry Group 19 (VGG19) to automatically detect bridge cracks at the pixel level and applied the self-attention mechanism not only for mining the semantic dependence features of the spatial and channel dimensions but also for adaptively integrating local features into their global dependence features[49]. The segmentation performance of the proposed approach was validated with public datasets containing 11,000 cracked and uncracked images and achieved excellent evaluation results in terms of the mean intersection over union (85.31%). Zhao *et al.* proposed a modified U-net for minute crack segmentation of 200 raw images in real-world, steel-box-girder bridges and applied a self-attention module with softmax and gate operations to obtain the attention vector, which enables the neuron to focus on the most significant receptive fields when processing large-scale feature maps[50]. The self-adaptation module, which consists of a multiplayer perceptron subnet, was selected for deeper feature extraction inside a single neuron. The self-attention mechanism mimics the internal process of biological observation behavior and can quickly extract important features of data, which is especially good at capturing the internal correlation of data or features.

For feature extraction from bridge crack multimodal data, the traditional feature extraction method of representative information has certain limitations, but the self-attention mechanism can reasonably allocate weights among the time domain, spatial domain and channel domain to extract the most relevant features of the target. The methods of feature extraction utilized in the above studies are summarized in Table 1.

2.2. Research status of the multisource heterogeneous data fusion representation of bridge cracks

The multisource heterogeneous parameters, such as the operating environment, load and structural mechanical state indices of bridge cracks, have a strong correlation and low density, and it is difficult to accurately and comprehensively reflect the evolution state of cracks. By analyzing and synthesizing the

Table 1. Summarized approaches of feature extraction on bridge cracks

Research	Method/approach	Advantages	Drawbacks
Yu *et al.*[31] Mei *et al.*[32]	PCA	Ability to remove noise and extract effective features	Unable to analyze the real subspace structure of data
Li *et al.*[34] Wang *et al.*[35]	Sparse decomposition	Ability to separate the signal and noise	Mass computation and computational complexity
Nguyen *et al.*[37] Nigam *et al.*[38]	Wavelet transform	Good denoising effect	Unable to identify the optimal wavelet base
Bilir *et al.*[43]	Adaptive neural fuzzy inference system	Self-learning ability and fuzzy logic reasoning ability	
Guo *et al.*[15] Zheng *et al.*[46] Xu *et al.*[47] Teng *et al.*[48]	Deep learning	Strong expression ability	Long calculation time
Pan *et al.*[49] Zhao *et al.*[50]	Self-Attention	Ability to quickly extract important features of data	

redundant and related monitoring data of the fracture, the data fusion method can more comprehensively and accurately evaluate the evolution state of the fracture. Classical information fusion methods include Bayesian estimation, DS (Dempster-Shafer) evidence theory, and the Kalman filter.

Bayesian estimation is based on the prior probability and posterior probability criteria in probability theory and uses conditional probability to represent the uncertain information in the monitoring data[51]. Li *et al.* employed a fully CNN and naive Bayesian data fusion model to automatically segment cracks and noise and fused the extracted multilayer features to obtain significant crack recognition performance[18]. The algorithm was verified with 7200 datasets of bridge substructures collected from 20 in-service bridges under various circumstances. The recognition results showed remarkable performance of the proposed algorithm compared to other recent algorithms. Bayesian estimation must rely on the distribution of the subjective prior probability of the data. However, some of the prior probability distribution of the monitoring data in the actual project is unknown. Therefore, there is a contradiction between this subjectivity and scientific objectivity.

DS evidence theory uses DS synthesis rules to fuse multiple pieces of evidence (feature information), eliminate or reduce the complementarity, redundancy and uncertainty among data, and obtain the fusion judgment or diagnosis of comprehensive features with certain decision rules. Zhao *et al.* applied DS evidence theory to perform weighted fusion on structural health monitoring data from multiple sensors of a two-story concrete frame to provide an accurate and final interpretation of the structural health status[52]. Guo *et al.* applied multiscale space theory and a data fusion method to detect the multiscale damage of beams and plates in a noisy environment and applied DS evidence theory to fuse and express the multiscale damage characteristics in a multiscale space to obtain good anti-noise ability and damage sensitivity[53]. DS evidence theory is mainly utilized to address the reasoning of uncertain information, but it lacks a certain theoretical basis and has potential exponential explosion risk in calculation.

According to the statistical principle, the Kalman filter uses the statistical characteristics of monitoring data and empirical data to perform real-time fusion representation of uncertain and dynamic redundant monitoring data. Prof. Zhang *et al.* employed a Kalman filter to fuse the parameters of the residual generator during the design of two-degrees-of-freedom controllers in a data-driven environment and a residual generator to explain all the stability[54]. Palanisamy *et al.* estimated a Kalman state structure model

based on finite element construction, which effectively fuses different types of acceleration, strain and tilt response data, minimizes internal measurement noise, and realizes the overall response measurement of bridge crack structures[55]. When the state of the monitoring system satisfies the Gaussian distribution and the linear model, the Kalman filter can perform a good fusion representation of the uncertain information and realize the optimal estimation. However, when the system does not satisfy the conditions of the Gaussian distribution and the linear model, this method will be limited.

In recent years, deep neural networks have become a controversial topic for scholars, and their application in data fusion has also achieved good results. Professor Li Hui *et al.* applied a fusion CNN for crack identification from real-world images containing complicated disturbance information (cracks, handwriting scripts, and background) inside steel box girders of bridges with 350 raw images as input[56]. The results demonstrated that the recognition errors of the fusion CNN in both the training and validation processes are smaller than those of the regular CNN. Li *et al.* developed a flexible crack recognition system for the complex bridge crack detection environment, which uses sliding window technology to process the acquired images and uses a trainable context encoder network to fuse the crack image information and features to achieve pixel-level bridge crack detection[57]. Chen *et al.* proposed a deep learning framework based on a CNN and naive Bayesian data fusion scheme to analyze the crack detection of a single video frame and proposed a novel data fusion scheme to extract spatiotemporal coherence information of cracks in videos to improve the overall performance and robustness of the system[58]. Yang *et al.* proposed an effective concrete crack segmentation network based on UAV-enabled edge computing and applied the method of atrous spatial pyramid pooling to realize free multiscale feature extraction and to fuse different levels of feature map information into lower-level features for crack detection[59].

Granular computing realizes the fusion representation of incomplete, imprecise and multimodal information by selecting the granularity space suitable for the diagnosis problem and via granularity transformation in different partition spaces. Granular computing[60] is a natural model that simulates human thinking and the solving of problems. It is a new paradigm for data analysis and problem-solving based on the relationship between two particles. Granular computing provides multi-granularity, multiperspective and multilevel description, reasoning and solution strategies for the satisfactory solution of complex problems and effectively fuses and represents massive multimodal data.

For multisource heterogeneous data fusion representations of fractures, although many traditional data fusion algorithms can fuse and represent multisource heterogeneous data, the monitored data have high dimensions and strong correlations and comprise spatiotemporal data. Traditional information fusion methods have difficulty mining the internal deep and complex feature information. The granularity space in granular computing is consistent with the multilevel and space-time characteristics of bridge health monitoring data, and these monitoring data can be fused and represented according to the granularity space that matches the crack damage diagnosis problem of the bridge.

The abovementioned methods for multisource heterogeneous data fusion representation are summarized in Table 2.

2.3. Research status of intelligent detection models for bridge cracks

The monitoring data is mixed, and the fracture evolution state and characterization information present a nonlinear relationship. The separability of this characterization information is weak, so it is difficult to analyze the monitoring data, accurately evaluate the fracture state and predict the development trend. Presently, intelligent detection methods can be divided into shallow network models, wide learning network

Table 2. Multisource heterogeneous data fusion representation methods

Research	Method/approach	Advantage	Drawback
Li *et al.*[18]	Bayesian estimation	Simple operation	Reliance on the distribution of the subjective prior probability of data
Zhao *et al.*[52] Guo *et al.*[53]	DS evidence theory	Applies reasoning to address uncertain information	Exponential explosion risk
Zhang *et al.*[54] Palanisamy *et al.*[55]	Kalman filter	Sufficient processing of data subject to Gaussian distribution	Inadequate processing of non-Gaussian data
Li *et al.*[56] Li *et al.*[57] Chen *et al.*[58] Yang *et al.*[59]	Deep learning time	Strong expression ability	Long calculation
Li *et al.*[60]	Granular computing	Sufficient processing of multi-granularity spatiotemporal data	

models and deep network models.

The shallow network model adopts a neural network with one single hidden layer and mines the characteristic information in the nonlinear data to realize the intelligent identification and diagnosis of scientific problems. Classic shallow diagnosis algorithms mainly include extreme learning machines, BP neural networks, and SVMs. Wang *et al.* proposed a multiview multitask crack detector to calculate various visual features (such as texture and edge) of the image area, suppress various background noise, and emphasize the separability of crack region features and complex background features[61]. The experimental results with 350 crack images showed that the proposed method improves the training efficiency with a precision of 92.3% and a recall of 89.7%. Yan *et al.* used a simple supported beam with a single crack and double cracks as an example to identify local cracks and proposed a damage identification method for beam structures based on a BP neural network and SVM[62]. The results showed that the strain mode difference curve at the damaged part undergoes considerable changes, and better identification accuracy is obtained, where the recognition efficiency for a single crack is 99.9% and 100% for a double crack with the BP neural network and 99.6% for a single crack and 99.9% for a double crack with the SVM. Liu *et al.* selected the cantilever beam as the research object and proposed a crack damage detection method with a BP neural network based on the curvature modulus ratio, the natural frequency, which uses the parameters of frequency relative attenuation and the first-order maximum curvature modulus ratio as the input, and the parameters of crack position and damage degree as the output and achieves a good crack identification effect in terms of a relative error of 1.7 on crack images with a size of 248.3 mm and an injury degree of 84.6%[63]. The shallow intelligent diagnosis algorithm has a hidden layer, which can mine complex feature information and be applied for intelligent diagnosis in many fields. However, when the data present massive growth and have multilevel high-dimensional features, the shallow intelligent diagnosis method is limited.

The broad learning system (BLS) method[64,65] is a kind of neural network that does not depend on the structure depth and can realize the diagnosis of research problems by widening the width of the network for information mining. Guo *et al.* adopted a network structure that combines deep learning and BLS on 40,000 concrete crack images, intelligently trains the network with the original image via linear and nonlinear mapping processes with dynamic updating of the weights, and performs binary classification of concrete surface cracks[66]. The results proved that the accuracy of the presented method achieves 98.55% and 96.12% and that the training time is 59.8 s and 95.76 s with two different datasets. Chen *et al.* and Xu *et al.* proposed a recursive BLS, which uses recursive connections at the enhancement nodes of the network to capture the dynamic characteristics of time series and shows excellent performance on the chaotic time series[67,68]. Their

experimental results showed that the accuracy achieved 91.96% with a training time of 123 minutes with the MS-Celeb-1 M face database and that the RMSE was reduced to 121.9 on air quality dataset prediction. The BLS performs abstract representation and incremental learning of dynamic high-dimensional data and achieves a high diagnostic accuracy, short time and strong real-time performance. However, the BLS is inferior to deep networks in terms of the deep data mining performance of feature extraction and has a poor effect on detection problems for time-dependent data.

The deep neural network model uses not only a deep neural network to represent the multilayer features of the identified object but also the extracted high-level features to reflect the intrinsic nature of the data, which has better robustness and diagnostic ability than the shallow network. Classic deep intelligent diagnosis methods include CNNs, deep belief networks and recursive neural networks. Li *et al.* employed the sliding window algorithm to divide not only the bridge crack image into slices with a size of 16 pixels × 16 pixels but also the slices into the bridge crack surface element and bridge background surface element[69]. The authors then proposed a deep bridge crack classification model based on CNN for the identification of bridge background surface elements and bridge crack surface elements. The proposed algorithm achieved an average accuracy of 94.5% with 2000 bridge crack images. Islam *et al.* established a deep CNN using an encoder and decoder framework for semantic segmentation to realize pixel-level automatic detection of bridge cracks, obtaining scores of approximately 92% for both the recall and F1 value[70]. Liang *et al.* utilized a double CNN model to identify cracks in actual concrete bridges, which highly improved the reliability and accuracy of identification with accuracies of 98.6% and 99.5% by the CNN and FCN models, respectively[71]. Li *et al.* proposed a new type of fully connected state, long-term and short-term memory neural network, which was employed to discriminate sensor faults and structural damage without knowing the fault details, and obtained excellent performance with an RMSE of 0.03[72]. The deep network model has made progress in big data processing. Although the training takes a long time due to the numerous network layers, complex structure, and many super parameters, it can process the data with complex internal information characteristics and is more suitable for the engineering needs of timely warning for dangerous situations in bridge health monitoring.

For intelligent crack detection model construction, a shallow network model can mine complex data for bridge crack detection, but its feature extraction ability is weak, and it cannot carry out multilayer feature representation for recognized objects. Thus the recognition rate is low and the generalization performance is mediocre. The BLS can mine and integrate multilevel and multimodal, complex state information by widening the network and incremental learning. The BLS achieves high diagnostic accuracy, fast speed and strong real-time performance for the research target but has a poor effect on the time-dependent data detection problem. The deep network model can represent the multilayer features of the recognized object and use the extracted high-level features to reflect the intrinsic nature of the data. The model has the ability of deep information mining and achieves better robustness, generalization and recognition performance.

The structure of the deep neural network mapping model is shown in Figure 3, and the methods utilized for intelligent detection in the above review articles are summarized in Table 3.

3. MAIN CHALLENGES

Despite great developments in the research on concrete bridge crack identification based on data, certain challenges exist.

As a cavity, the crack has three-dimensional information with length, width and depth. However, traditional crack identification is usually based on the recognition with the two-dimensional surface information

Table 3. Intelligent detection methods

Research	Method/approach	Advantage	Drawback
Wang *et al.*[61] Yan *et al.*[62] Liu *et al.*[63]	Machine learning	Excellent predictive performance	Unsuitable for large sample data
Guo *et al.*[66] Xu *et al.*[67,68]	Broad learning system	High accuracy and short time	Unsuitable for sequential data
Li *et al.*[69] Islam *et al.*[70] Liang *et al.*[71] Li *et al.*[72]	Deep learning	Sufficient for deep mining big data information	Long computing time

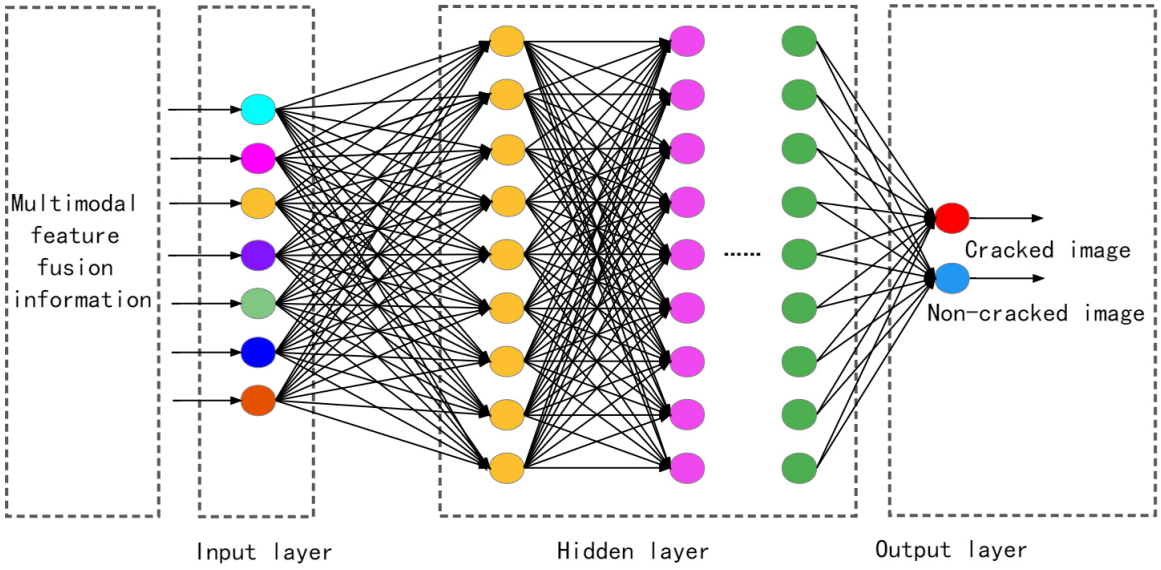

Figure 3. Structure of the deep neural network mapping model.

(length and width) of cracks, and research on three-dimensional cracks is limited. Although three-dimensional crack reconstruction technology has gradually attracted researchers' attention[73,74], its evolution mechanism remains ambiguous. There is an urgent need in the field of bridge disease detection to investigate the law of crack evolution and to predict the trend of crack degradation.

In bridge crack research based on data, bridge health monitoring systems has an irreplaceable role. The main purpose of research on the long-span bridge health monitoring system is to accumulate the design and scientific research data of bridge health monitoring, realize the real-time damage diagnosis and safety assessment of the structure, and support management and maintenance decision-making. Presently, the challenges faced in bridge health monitoring mainly include decision-making and the design of health monitoring systems, sensor signal preprocessing, and signal data noise reduction.

4. CONCLUSION

This paper presents a comprehensive review of recent advances in the field of data-driven bridge crack health detection. The latest achievements in bridge crack feature extraction, data fusion and intelligent

detection are introduced. Based on the discussion of the three technical difficulties of bridge crack multimodal data feature extraction, multisource heterogeneous data fusion representation, and intelligent crack detection model construction, the latest progress in bridge crack detection research is summarized in detail, and their major advantages and drawbacks in this field are highlighted. The main current challenges and potential future research directions are also discussed.

DECLARATIONS

Authors' contributions

Made substantial contributions to the research and investigation process, reviewed and summarized the literature, wrote and edited the original draft: Wang D

Performed oversight and leadership responsibility for the research activity planning and execution, as well as performed critical review, commentary and revision: Yang SX

Availability of data and materials

Not applicable.

Financial support and sponsorship

This work was supported by the National Natural Science Foundation of China (Grant No. 62103068; Grant No. 51978111), Science and Technology Research Project of Chongqing Education Commission (Contract No. KJQN202100745).

Conflicts of interest

All authors declared that there are no conflicts of interest.

Ethical approval and consent to participate

Not applicable.

Consent for publication

Not applicable.

REFERENCES

1. Sun Y, Ma K, Sheng D, Liu D, Dai B, Sun L. Research on bridge structural damage identification. *Sci Program* 2022;2022:1-14. DOI
2. Lin W, Sun Y, Yang Q, Lin Y. Real-time comprehensive image processing system for detecting concrete bridges crack. *Comput Concr* 2019;23:445-457. DOI
3. Putra SA, Trilaksono BR, Riyansyah M, Laila DS. Multiagent architecture for bridge capacity measurement system using wireless sensor network and weight in motion. *IEEE Trans Instrum Meas* 2021;70:1-14. DOI
4. Collings D, Sagaseta J. Modern concrete bridge deck analysis considering the effects of cracking. *Proc Inst Civ Eng: Struct Build* 2021;174:595-605. DOI
5. Mao J, Yang C, Wang H, Zhang Y, Lu H. Bayesian operational modal analysis with genetic optimization for structural health monitoring of the long-span bridge. *Int J Str Stab Dyn* 2022;22:2250051. DOI
6. Maes K, Van Meerbeeck L, Reynders E, Lombaert G. Validation of vibration-based structural health monitoring on retrofitted railway bridge KW51. *Mech Syst Signal Process* 2022;165:108380. DOI
7. Prasanna P, Dana KJ, Gucunski N, et al. Automated crack detection on concrete bridges. *IEEE Trans Automat Sci Eng* 2016;13:591-9. DOI
8. Zhang L, Zhou G, Han Y, Lin H, Wu Y. Application of internet of things technology and convolutional neural network model in bridge crack detection. *IEEE Access* 2018;6:39442-51. DOI
9. Li H, Xu H, Tian X, et al. Bridge crack detection based on ssenets. *Appl Sci* 2020;10:4230. DOI PubMed PMC
10. Jiang W, Liu M, Peng Y, Wu L, Wang Y. HDCB-net: a neural network with the hybrid dilated convolution for pixel-level crack

detection on concrete bridges. *IEEE Trans Ind Inf* 2021;17:5485-94. DOI

11. Yamaguchi T, Mizutani T, Tarumi M, Su D. Sensitive damage detection of reinforced concrete bridge slab by "time-variant deconvolution" of SHF-band radar signal. *IEEE Trans Geosci Remote Sensing* 2019;57:1478-88. DOI
12. Xu H, Su X, Wang Y, Cai H, Cui K, Chen X. Automatic bridge crack detection using a convolutional neural network. *Applied Sciences* 2019;9:2867. DOI
13. Gao R, He J. Seismic performance assessment of concrete bridges with traffic-induced fatigue damage. *Eng Fail Anal* 2022;134:106042. DOI
14. Lon Wah W, Xia Y. Elimination of outlier measurements for damage detection of structures under changing environmental conditions. *Struct Health Monit* 2022;21:320-38. DOI
15. Guo L, Li R, Jiang B. A cascade broad neural network for concrete structural crack damage automated classification. *IEEE Trans Industr Inform* 2021;17:2737-42. DOI
16. Okazaki Y, Okazaki S, Asamoto S, Chun P. Applicability of machine learning to a crack model in concrete bridges. *COMPUT-AIDED CIV INF* 2020;35:775-92. DOI
17. Lu Q, Zhu J, Zhang W. Quantification of fatigue damage for structural details in slender coastal bridges using machine learning-based methods. *J Bridge Eng* 2020;25:04020033. DOI
18. Li G, Liu Q, Zhao S, Qiao W, Ren X. Automatic crack recognition for concrete bridges using a fully convolutional neural network and naive Bayes data fusion based on a visual detection system. *Meas Sci Technol* 2020;31:075403. DOI
19. Kumar P, Sharma A, Kota SR. Automatic multiclass instance segmentation of concrete damage using deep learning model. *IEEE Access* 2021;9:90330-45. DOI
20. Pathak N. Bridge health monitoring using CNN. 2020 International Conference on Convergence to Digital World - Quo Vadis (ICCDW); 2020 Feb. 18-20; Mumbai, India: IEEE; 2020. p. 1-4. DOI
21. Attard L, Debono CJ, Valentino G, Castro MD, Masi A, Scibile L. Automatic crack detection using mask R-CNN. 2019 11th International Symposium on Image and Signal Processing and Analysis (ISPA); 2019 Sept. 23-25 Dubrovnik, Croatia: IEEE; 2019. p. 152-157. DOI
22. Kamada S, Ichimura T, Iwasaki T. An adaptive structural learning of deep belief network for image-based crack detection in concrete structures using SDNET2018. 2020 International Conference on Image Processing and Robotics (ICIP); 2020 Mar. 06-08 Negombo, Sri Lanka: IEEE; 2020. p. 1-6. DOI
23. Liu T, Zhang L, Zhou G, Cai W, Cai C, Li L. BC-DUnet-based segmentation of fine cracks in bridges under a complex background. *PLoS One* 2022;17:e0265258. DOI PubMed PMC
24. Simonetti F, Satow IL, Brath AJ, et al. Cryo-ultrasonic NDE: ice-cold ultrasonic waves for the detection of damage in complex-shaped engineering components. *IEEE Trans Ultrason Ferroelectr Freq Control* 2018;65:638-47. DOI PubMed
25. Zhou LQ, Colston G, Myronov M, et al. Ultrasonic inspection and self-healing of ge and 3C-SiC semiconductor membranes. *J Microelectromech Syst* 2020;29:370-7. DOI
26. Lee FW, Chai HK, Lim KS, Lau SH. Concrete sub-surface crack characterization by means of surface rayleigh wave method. *ACI Materials Journal* 2019:116. DOI
27. Wadas SH, Tschache S, Polom U, Krawczyk CM. Ground instability of sinkhole areas indicated by elastic moduli and seismic attributes. *Geophys J Int* 2020;222:289-304. DOI
28. Ghasemi MF, Bayuk IO. Application of rock physics modelling to investigate the differences between static and dynamic elastic moduli of carbonates. *Geophys J Int* 2020;222:1992-2023. DOI
29. Luan X, Huang B, Sedghi S, Liu F. Probabilistic PCR based near-infrared modeling with temperature compensation. *ISA Trans* 2018;81:46-51. DOI PubMed
30. Zhu J, Ge Z, Song Z. Distributed parallel PCA for modeling and monitoring of large-scale plant-wide processes with big data. *IEEE Trans Ind Inf* 2017;13:1877-85. DOI
31. Yu Y, Rashidi M, Samali B, Yousefi AM, Wang W. Multi-image-feature-based hierarchical concrete crack identification framework using optimized SVM multi-classifiers and D-S fusion algorithm for bridge structures. *Remote Sens* 2021;13:240. DOI
32. Mei Q, Gül M, Boay M. Indirect health monitoring of bridges using Mel-frequency cepstral coefficients and principal component analysis. *Mech Syst Signal Process* 2019;119:523-46. DOI
33. Dong Z, Sun X, Xu F, Liu W. A low-rank and sparse decomposition-based method of improving the accuracy of sub-pixel grayscale centroid extraction for spot images. *IEEE Sensors J* 2020;20:5845-54. DOI
34. Li L, Gao X, Sun R, Lu C. Study on bridge floor crack classification method based on sparse coding. *J Light Technol* 2018;33:66-74. DOI
35. Wang B, Zhang Q, Zhao W. Fast concrete crack detection method via L2 sparse representation. *Electron lett* 2018;54:752-4. DOI
36. Naveed K, Rehman NU. Wavelet based multivariate signal denoising using mahalanobis distance and EDF statistics. *IEEE Trans Signal Process* 2020;68:5997-6010. DOI
37. Nguyen TQ, Vuong LC, Le CM, Ngo NK, Nguyen-Xuan H. A data-driven approach based on wavelet analysis and deep learning for identification of multiple-cracked beam structures under moving load. *Meas Sci Technol* 2020;162:1-21. DOI
38. Nigam R, Singh SK. Crack detection in a beam using wavelet transform and photographic measurements. *Structures* 2020;25:436-47. DOI
39. Wang S, Feng J, Jiang Y. Input-output method to fault detection for discrete-time fuzzy networked systems with time-varying delay

and multiple packet losses. *Int J Syst Sci* 2016;47:1495-513. DOI

40. Liu L, Wang Z, Zhang H. Adaptive NN fault-tolerant control for discrete-time systems in triangular forms with actuator fault. *Neurocomputing* 2015;152:209-221. DOI
41. Mao W-L, Chu C-T. Modeless magnetic bearing system tracking using an adaptive fuzzy hermite neural network method. *IEEE Sens J* 2019;19:5904-15. DOI
42. Na J, Huang Y, Wu X, Su S-F, Li G. Adaptive finite-time fuzzy control of nonlinear active suspension systems with input delay. *IEEE Trans Cybern* 2020;50:2639-50. DOI PubMed
43. Bilir T, Gencel O, Topcu IB. Prediction of restrained shrinkage crack widths of slag mortar composites by Takagi and Sugeno ANFIS models. *Neural Comput Appl* 2016;27:2523-36. DOI
44. Sharma M, Anotaipaiboon W, Chaiyasarn K. Concrete crack detection using the integration of convolutional neural network and support vector machine. *Sci Technol Asia* 2018;23:19-28. DOI
45. Wang D, Dong Y, Pan Y, Ma R. Machine vision-based monitoring methodology for the fatigue cracks in U-Rib-to-Deck weld seams. *IEEE Access* 2020;8:94204-19. DOI
46. Zheng M, Lei Z, Zhang K. Intelligent detection of building cracks based on deep learning. *Image Vis Comput* 2020;103:1-10. DOI
47. Xu H, Su X, Wang Y, Cai H, Cui K, Chen X. Automatic bridge crack detection using a convolutional neural network. *Appl Sci* 2019;9:2867. DOI
48. Teng S, Liu Z, Chen G, Cheng L. Concrete crack detection based on well-known feature extractor model and the YOLO_v2 network. *Appl Sci* 2021;11:1-13. DOI
49. Pan Y, Zhang G, Zhang L. A spatial-channel hierarchical deep learning network for pixel-level automated crack detection. *Autom Constr* 2020;119:103357. DOI
50. Zhao J, Hu F, Qiao W, Zhai W, Xu Y, Bao Y, et al. A modified U-net for crack segmentation by self-attention-self-adaption neuron and random elastic deformation. *Smart Struct Syst* 2022;29:1-16. DOI
51. Yang Y, Sun H, Xue J, et al. Correction to: estimating evapotranspiration by coupling bayesian model averaging methods with machine learning algorithms. *Environ Monit Assess* 2021;193:207. DOI PubMed
52. Zhao X, Wang R, Gu H, Song G, Mo YL. Innovative data fusion enabled structural health monitoring approach. *Math Probl Eng* 2014;2014:1-10. DOI
53. Guo T, Xu Z. Data fusion of multi-scale representations for structural damage detection. *Mech Syst Signal Process* 2018;98:1020-33. DOI
54. Zhang Y, Ding SX, Yang Y, Li L. Data□driven design of two□degree□of□freedom controllers using reinforcement learning techniques. *IIET Control Theory Appl* 2015;9:1011-21. DOI
55. Palanisamy RP, Cho S, Kim H, Sim S. Experimental validation of Kalman filter-based strain estimation in structures subjected to non-zero mean input. *Smart Struct Syst* 2015;15:489-503. DOI
56. Xu Y, Bao Y, Chen J, Zuo W, Li H. Surface fatigue crack identification in steel box girder of bridges by a deep fusion convolutional neural network based on consumer-grade camera images. *Struct Health Monit* 2019;18:653-74. DOI
57. Li G, Li X, Zhou J, Liu D, Ren W. Pixel-level bridge crack detection using a deep fusion about recurrent residual convolution and context encoder network. *Measurement* 2021;176:109171. DOI
58. Chen F, Jahanshahi MR. NB-CNN: Deep learning-based crack detection using convolutional neural network and naïve bayes data fusion. *IEEE Trans Ind Electron* 2018;65:4392-400. DOI
59. Yang J, Li H, Zou J, Jiang S, Li R, Liu X. Concrete crack segmentation based on UAV-enabled edge computing. *Neurocomputing* 2022;485:233-41. DOI
60. Li X, Zhou J, Pedrycz W. Linking granular computing, big data and decision making: a case study in urban path planning. *Soft Comput* 2020;24:7435-50. DOI
61. Wang B, Zhao W, Gao P, Zhang Y, Wang Z. Crack damage detection method via multiple visual features and efficient multi-task learning model. *Sensors (Basel)* 2018;18:1796. DOI PubMed PMC
62. Yan B, Cui Y, Zhang L, et al. Beam structure damage identification based on BP neural network and support vector machine. *Math Probl Eng* 2014;2014:1-8. DOI
63. Liu M, Li L, Zhao X, Liu H. The crack injury detection based CMR and Natural frequency with BP neutral network. 2nd International Conference on Future Networks (ICFN 2010); 2010 Jan. 22-24; Sanya, Chin: IEEE; 2010. p. 314-17. DOI
64. Chen CLP, Liu Z. Broad learning system: a new learning paradigm and system without going deep. 32nd Youth Academic Annual Conference of Chinese Association of Automation (YAC); 2017 May 19-21; Hefei, China: IEEE; 2017. p. 17009788. DOI
65. Chen CLP, Liu Z. Broad learning system: an effective and efficient incremental learning system without the need for deep architecture. *IEEE Trans Neural Netw Learn Syst* 2018;29:10-24. DOI PubMed
66. Guo L, Li R, Jiang B, Shen X. Automatic crack distress classification from concrete surface images using a novel deep-width network architecture. *Neurocomputing* 2020;397:383-92. DOI
67. Chen CLP, Liu Z, Feng S. Universal approximation capability of broad learning system and its structural variations. *IEEE Trans Neural Netw Learn Syst* 2019;30:1191-204. DOI PubMed
68. Xu M, Han M, Chen CLP, Qiu T. Recurrent broad learning systems for time series prediction. *IEEE Trans Cybern* 2020;50:1405-17. DOI PubMed
69. Li C, Cheng D, Li Y. Research on bridge crack detection algorithm based on deep learning. *J Lab Autom* 2019;45:16. DOI

70. Islam MMM, Kim JM. Vision-based autonomous crack detection of concrete structures using a fully convolutional encoder-decoder network. *Sensors (Basel)* 2019;19:4251. DOI PubMed PMC
71. Liang D, Zhou X, Wang S, Liu C. Research on concrete cracks recognition based on dual convolutional neural network. *KSCE J Civ Eng* 2019;23:3066-74. DOI
72. Li L, Liu G, Zhang L, Li Q. FS-LSTM-based sensor fault and structural damage isolation in SHM. *IEEE Sensors J* 2021;21:3250-9. DOI
73. Zhao Z, Zhou X. 3D digital analysis of cracking behaviors of rocks through 3D reconstruction model under triaxial compression. *J Eng Mech* 2020;146:04020084. DOI
74. Yang L, Li B, Li W, Brand H, Jiang B, Xiao J. Concrete defects inspection and 3D mapping using CityFlyer quadrotor robot. *IEEE/CAA J Autom Sinica* 2020;7:991-1002. DOI

AUTHOR INSTRUCTIONS

1. Submission Overview

Before you decide to publish with *Intelligence & Robotics* (*IR*), please read the following items carefully and make sure that you are well aware of Editorial Policies and the following requirements.

1.1 Topic Suitability

The topic of the manuscript must fit the scope of the journal. Please refer to Aims and Scope for more information.

1.2 Open Access and Copyright

The journal adopts Gold Open Access publishing model and distributes content under the Creative Commons Attribution 4.0 International License. Copyright is retained by authors. Please make sure that you are well aware of these policies.

1.3 Publication Fees

Before December 31, 2024, there are no article processing charges for papers accepted for publication after peer review. OAE subsidizes and helps authors publish their manuscripts totally free. For more details, please refer to OAE Publication Fees.

1.4 Language Editing

All submissions are required to be presented clearly and cohesively in good English. Authors whose first language is not English are advised to have their manuscripts checked or edited by a native English speaker before submission to ensure the high quality of expression. A well-organized manuscript in good English would make the peer review even the whole Editorial handling more smoothly and efficiently.

If needed, authors are recommended to consider the language editing services provided by Charlesworth to ensure that the manuscript is written in correct scientific English before submission. Authors who publish with OAE journals enjoy a special discount for the services of Charlesworth via the following two ways.

Submit your manuscripts directly at http://www.charlesworthauthorservices.com/~OAE;

Open the link http://www.charlesworthauthorservices.com/, and enter Promotion Code “OAE” when you submit.

1.5 Work Funded by the National Institutes of Health

If an accepted manuscript was funded by National Institutes of Health (NIH), the author may inform editors of the NIH funding number. The editors are able to deposit the paper to the NIH Manuscript Submission System on behalf of the author.

2. Submission Preparation

2.1 Cover Letter

A cover letter is required to be submitted accompanying each manuscript. Here is a guideline of a cover letter for authors’ consideration:

List the highlights of the current manuscript and no more than 5 short sentences;

All authors have read the final manuscript, have approved the submission to the journal, and have accepted full responsibilities pertaining to the manuscript’s delivery and contents;

Clearly state that the manuscript is an original work on its own merit, that it has not been previously published in whole or in part, and that it is not being considered for publication elsewhere;

No materials are reproduced from another source (if there is material in your manuscript that has been reproduced from another source, please state whether you have obtained permission from the copyright holder to use them);

Conflicts of interest statement;

If the manuscript is contributed to a Special Issue, please also mention it in the cover letter;

If the manuscript was presented partly or entirely in a conference, the author should clearly state the background information of the event, including the conference name, time, and place in the cover letter.

2.2 Types of Manuscripts

There is no restriction on the length of manuscripts, number of figures, tables and references, provided that the manuscript is concise and comprehensive. The journal publishes Research Article, Review, Technical Note, etc. For more details about paper type, please refer to the following table.

Manuscript Type	Definition	Abstract	Keywords	Main Text Structure
Research Article	A Research Article is a seminal and insightful research study and showcases that often involves modern techniques or methodologies. Authors should justify that their work is of novel findings.	The abstract should state briefly the purpose of the research, the principal results and major conclusions. No more than 250 words.	3-8 keywords	The main content should include four sections: Introduction, Methods, Results and Discussion.
Review	A Review should be an authoritative, well balanced, and critical survey of recent progress in an attractive or a fundamental research field.	Unstructured abstract. No more than 250 words.	3-8 keywords	The main text may consist of several sections with unfixed section titles. We suggest that the author include an "Introduction" section at the beginning, several sections with unfixed titles in the middle part, and a "Conclusions" section at the end.
Technical Note	A Technical Note is a short article giving a brief description of a specific development, technique, or procedure, or it may describe a modification of an existing technique, procedure or device applied in research.	Unstructured abstract. No more than 250 words.	3-8 keywords	/
Editorial	An Editorial is a short article describing news about the journal or opinions of senior Editors or the publisher.	None required	None required	/
Commentary	A Commentary is to provide comments on a newly published article or an alternative viewpoint on a certain topic.	Unstructured abstract. No more than 250 words.	3-8 keywords	/
Perspective	A Perspective provides personal points of view on the state-of-the-art of a specific area of knowledge and its future prospects.	Unstructured abstract. No more than 250 words.	3-8 keywords	/

2.3 Manuscript Structure

2.3.1 Front Matter

2.3.1.1 Title

The title of the manuscript should be concise, specific and relevant, with no more than 16 words if possible.

2.3.1.2 Authors and Affiliations

Authors' full names should be listed. The initials of middle names can be provided. The affiliations and email addresses for all authors should be listed. At least one author should be designated as the corresponding author. In addition, corresponding authors are suggested to provide their Open Researcher and Contributor ID upon submission. Please note that any change to authorship is not allowed after manuscript acceptance. The authors' affiliations should be provided in this format: department, institution, city, postcode, country.

2.3.1.3 Abstract

The abstract should be a single paragraph with word limitation and specific structure requirements (for more details please refer to Types of Manuscripts). It usually describes the main objective(s) of the study, explains how the study was done, including any model organisms used, without methodological detail, and summarizes the most important results and their significance. The abstract must be an objective representation of the study: it is not allowed to contain results that are not presented and substantiated in the manuscript, or exaggerate the main conclusions. Citations should not be included in the abstract.

2.3.1.4 Graphical Abstract

The graphical abstract is essential as this can catch first view of your publication by readers. We recommend you submit an eye-catching figure. It should summarize the content of the article in a concise graphical form. It is recommended to use it because this can make online articles get more attention.

The graphical abstract should be submitted as a separate document in the online submission system. Please provide an image with a minimum of 531 × 1328 pixels (h × w) or proportionally more. The image should be readable at a size of 5 cm × 13 cm using a regular screen resolution of 96 dpi. Preferred file types: TIFF, PSD, AI, JPEG, and EPS files.

2.3.1.5 Keywords

Three to eight keywords should be provided, which are specific to the article, yet reasonably common within the subject discipline.

2.3.2 Main Text

Manuscripts of different types are structured with different sections of content. Please refer to Types of Manuscripts to make sure which sections should be included in the manuscripts.

2.3.2.1 Introduction

The introduction should contain background that puts the manuscript into context, allow readers to understand why the study is important, include a brief review of key literature, and conclude with a brief statement of the overall aim of the work and a comment about whether that aim was achieved. Relevant controversies or disagreements in the field should be introduced as well.

2.3.2.2 Methods

The methods should contain sufficient details to allow others to fully replicate the study. New methods and protocols should be described in detail while well-established methods can be briefly described or appropriately cited. Statistical terms, abbreviations, and all symbols used should be defined clearly. Protocol documents for clinical trials, observational studies, and other non-laboratory investigations may be uploaded as supplementary materials.

2.3.2.3 Results

This section contains the findings of the study. Results of statistical analysis should also be included either as text or as tables or figures if appropriate. Authors should emphasize and summarize only the most important observations. Data on all primary and secondary outcomes identified in the section Methods should also be provided. Extra or supplementary materials and technical details can be placed in supplementary documents.

2.3.2.4 Discussion

This section should discuss the implications of the findings in context of existing research and highlight limitations of the study. Future research directions may also be mentioned.

2.3.2.5 Conclusion

It should state clearly the main conclusions and include the explanation of their relevance or importance to the field.

2.3.3 Back Matter

2.3.3.1 Acknowledgments

Anyone who contributed towards the article but does not meet the criteria for authorship, including those who provided professional writing services or materials, should be acknowledged. Authors should obtain permission to acknowledge from all those mentioned in the Acknowledgments section. This section is not added if the author does not have anyone to acknowledge.

2.3.3.2 Authors' Contributions

Each author is expected to have made substantial contributions to the conception or design of the work, or the acquisition, analysis, or interpretation of data, or the creation of new software used in the work, or have drafted the work or substantively revised it.

Please use Surname and Initial of Forename to refer to an author's contribution. For example: made substantial contributions to conception and design of the study and performed data analysis and interpretation: Salas H, Castaneda WV; performed data acquisition, as well as providing administrative, technical, and material support: Castillo N, Young V.

If an article is single-authored, please include "The author contributed solely to the article." in this section.

2.3.3.3 Availability of Data and Materials

In order to maintain the integrity, transparency and reproducibility of research records, authors should include this section in their manuscripts, detailing where the data supporting their findings can be found. Data can be deposited into data repositories or published as supplementary information in the journal. Authors who cannot share their data should state that the data will not be shared and explain it. If a manuscript does not involve such issues, please state "Not applicable." in this section.

2.3.3.4 Financial Support and Sponsorship

All sources of funding for the study reported should be declared. The role of the funding body in the experiment design, collection, analysis and interpretation of data, and writing of the manuscript should be declared. Any relevant grant numbers and the link of funder's website should be provided if any. If the study is not involved with this issue, state "None." in this section.

2.3.3.5 Conflicts of Interest

Authors must declare any potential conflicts of interest that may be perceived as inappropriately influencing the representation or interpretation of reported research results. If there are no conflicts of interest, please state "All authors declared that there are no conflicts of interest." in this section. Some authors may be bound by confidentiality agreements. In such cases, in place of itemized disclosures, we will require authors to state "All authors declared that they are bound by confidentiality agreements that prevent them from disclosing their conflicts of interest in this work.". If authors are unsure whether conflicts of interest exist, please refer to the "Conflicts of Interest" of *IR* Editorial Policies for a full explanation.

2.3.3.6 Ethical Approval and Consent to Participate

Research involving human subjects, human material or human data must be performed in accordance with the Declaration of Helsinki and approved by an appropriate ethics committee. An informed consent to participate in the study should also be obtained from participants, or their parents or legal guardians for children under 16. A statement detailing the name of the ethics committee (including the reference number where appropriate) and the informed consent obtained must appear in the manuscripts reporting such research.

Studies involving animals and cell lines must include a statement on ethical approval. More information is available at Editorial Policies.

If the manuscript does not involve such issue, please state "Not applicable." in this section.

2.3.3.7 Consent for Publication

Manuscripts containing individual details, images or videos, must obtain consent for publication from that person, or in the case of children, their parents or legal guardians. If the person has died, consent for publication must be obtained from the next of kin of the participant. Manuscripts must include a statement that written informed consent for publication was obtained. Authors do not have to submit such content accompanying the manuscript. However, these documents must be available if requested. If the manuscript does not involve this issue, state "Not applicable." in this section.

2.3.3.8 Copyright

Authors retain copyright of their works through a Creative Commons Attribution 4.0 International License that clearly states how readers can copy, distribute, and use their attributed research, free of charge. A declaration "© The Author(s) 2022." will be added to each article. Authors are required to sign License to Publish before formal publication.

2.3.3.9 References

References should be numbered in order of appearance at the end of manuscripts. In the text, reference numbers should be placed in square brackets and the corresponding references are cited thereafter. If the number of authors is less than or equal to six, we require to list all authors' names. If the number of authors is more than six, only the first three authors' names are required to be listed in the references, other authors' names should be omitted and replaced with "et al.". Abbreviations of the journals should be provided on the basis of Index Medicus. Information from manuscripts accepted but not published should be cited in the text as "Unpublished material" with written permission from the source.

References should be described as follows, depending on the types of works:

Types	**Examples**
Journal articles by individual authors	Weaver DL, Ashikaga T, Krag DN, et al. Effect of occult metastases on survival in node-negative breast cancer. *N Engl J Med* 2011;364:412-21. [PMID: 21247310 DOI: 10.1056/NEJMoa1008108]
Organization as author	Diabetes Prevention Program Research Group. Hypertension, insulin, and proinsulin in participants with impaired glucose tolerance. *Hypertension* 2002;40:679-86. [DOI: 10.1161/01.HYP.0000035706.28494.09]
Both personal authors and organization as author	Vallancien G, Emberton M, Harving N, van Moorselaar RJ; Alf-One Study Group. Sexual dysfunction in 1,274 European men suffering from lower urinary tract symptoms. *J Urol* 2003;169:2257-61. [PMID: 12771764 DOI: 10.1097/01.ju.0000067940.76090.73]
Journal articles not in English	Zhang X, Xiong H, Ji TY, Zhang YH, Wang Y. Case report of anti-N-methyl-D-aspartate receptor encephalitis in child. *J Appl Clin Pediatr* 2012;27:1903-7. (in Chinese)
Journal articles ahead of print	Odibo AO. Falling stillbirth and neonatal mortality rates in twin gestation: not a reason for complacency. BJOG 2018; Epub ahead of print [PMID: 30461178 DOI: 10.1111/1471-0528.15541]
Books	Sherlock S, Dooley J. Diseases of the liver and billiary system. 9th ed. Oxford: Blackwell Sci Pub; 1993. pp. 258-96.
Book chapters	Meltzer PS, Kallioniemi A, Trent JM. Chromosome alterations in human solid tumors. In: Vogelstein B, Kinzler KW, editors. The genetic basis of human cancer. New York: McGraw-Hill; 2002. pp. 93-113.
Online resource	FDA News Release. FDA approval brings first gene therapy to the United States. Available from: https://www.fda.gov/NewsEvents/Newsroom/PressAnnouncements/ucm574058.htm. [Last accessed on 30 Oct 2017]

Conference proceedings	Harnden P, Joffe JK, Jones WG, Editors. Germ cell tumours V. Proceedings of the 5th Germ Cell Tumour Conference; 2001 Sep 13-15; Leeds, UK. New York: Springer; 2002.
Conference paper	Christensen S, Oppacher F. An analysis of Koza's computational effort statistic for genetic programming. In: Foster JA, Lutton E, Miller J, Ryan C, Tettamanzi AG, editors. Genetic programming. EuroGP 2002: Proceedings of the 5th European Conference on Genetic Programming; 2002 Apr 3-5; Kinsdale, Ireland. Berlin: Springer; 2002. pp. 182-91.
Unpublished material	Tian D, Araki H, Stahl E, Bergelson J, Kreitman M. Signature of balancing selection in Arabidopsis. *Proc Natl Acad Sci U S A*. Forthcoming 2002.

The journal also recommends that authors prepare references with a bibliography software package, such as EndNote to avoid typing mistakes and duplicated references.

2.3.3.10 Supplementary Materials

Additional data and information can be uploaded as Supplementary Materials to accompany the manuscripts. The supplementary materials will also be available to the referees as part of the peer-review process. Any file format is acceptable, such as data sheet (word, excel, csv, cdx, fasta, pdf or zip files), presentation (powerpoint, pdf or zip files), image (cdx, eps, jpeg, pdf, png or tiff), table (word, excel, csv or pdf), audio (mp3, wav or wma) or video (avi, divx, flv, mov, mp4, mpeg, mpg or wmv). All information should be clearly presented. Supplementary materials should be cited in the main text in numeric order (e.g., Supplementary Figure 1, Supplementary Figure 2, Supplementary Table 1, Supplementary Table 2, *etc*.). The style of supplementary figures or tables complies with the same requirements on figures or tables in main text. Videos and audios should be prepared in English, and limited to a size of 500 MB.

2.4 Manuscript Format

2.4.1 File Format

Manuscript files can be in DOC and DOCX formats and should not be locked or protected.
Manuscript prepared in LaTex must be collated into one ZIP folder (including all source files and images, so that the Editorial Office can recompile the submitted PDF).
When preparing manuscripts in different file formats, please use the corresponding Manuscript Templates.

2.4.2 Length

There are no restrictions on paper length, number of figures, or number of supporting documents. Authors are encouraged to present and discuss their findings concisely.

2.4.3 Language

Manuscripts must be written in English.

2.4.4 Multimedia Files

The journal supports manuscripts with multimedia files. The requirements are listed as follows:
Video or audio files are only acceptable in English. The presentation and introduction should be easy to understand. The frames should be clear, and the speech speed should be moderate;
A brief overview of the video or audio files should be given in the manuscript text;
The video or audio files should be limited to a size of up to 500 MB;
Please use professional software to produce high-quality video files, to facilitate acceptance and publication along with the submitted article. Upload the videos in mp4, wmv, or rm format (preferably mp4) and audio files in mp3 or wav format.

2.4.5 Figures

Figures should be cited in numeric order (e.g., Figure 1, Figure 2) and placed after the paragraph where it is first cited;
Figures can be submitted in format of TIFF, PSD, AI, EPS or JPEG, with resolution of 300-600 dpi;
Figure caption is placed under the Figure;
Diagrams with describing words (including, flow chart, coordinate diagram, bar chart, line chart, and scatter diagram, *etc*.) should be editable in word, excel or powerpoint format. Non-English information should be avoided;
Labels, numbers, letters, arrows, and symbols in figure should be clear, of uniform size, and contrast with the background;
Symbols, arrows, numbers, or letters used to identify parts of the illustrations must be identified and explained in the legend;
Internal scale (magnification) should be explained and the staining method in photomicrographs should be identified;
All non-standard abbreviations should be explained in the legend;
Permission for use of copyrighted materials from other sources, including re-published, adapted, modified, or partial figures and images from the internet, must be obtained. It is authors' responsibility to acquire the licenses, to follow any citation instruction requested by third-party rights holders, and cover any supplementary charges.

2.4.6 Tables

Tables should be cited in numeric order and placed after the paragraph where it is first cited;
The table caption should be placed above the table and labeled sequentially (e.g., Table 1, Table 2);
Tables should be provided in editable form like DOC or DOCX format (picture is not allowed);
Abbreviations and symbols used in table should be explained in footnote;
Explanatory matter should also be placed in footnotes;
Permission for use of copyrighted materials from other sources, including re-published, adapted, modified, or partial tables from the internet, must be obtained. It is authors' responsibility to acquire the licenses, to follow any citation instruction requested by third-party rights holders, and cover any supplementary charges.

2.4.7 Abbreviations

Abbreviations should be defined upon first appearance in the abstract, main text, and in figure or table captions and used consistently thereafter. Non-standard abbreviations are not allowed unless they appear at least three times in the text. Commonly-used abbreviations, such as DNA, RNA, ATP, *etc*., can be used directly without definition. Abbreviations in titles and keywords should be avoided, except for the ones which are widely used.

2.4.8 Italics

General italic words like *vs*., *et al*., *etc*., *in vivo*, *in vitro*; *t* test, *F* test, *U* test; related coefficient as *r*, sample number as *n*, and probability as *P*; names of genes; names of bacteria and biology species in Latin.

2.4.9 Units

SI Units should be used. Imperial, US customary and other units should be converted to SI units whenever possible. There is a space between the number and the unit (i.e., 23 mL). Hour, minute, second should be written as h, min, s.

2.4.10 Numbers

Numbers appearing at the beginning of sentences should be expressed in English. When there are two or more numbers in a paragraph, they should be expressed as Arabic numerals; when there is only one number in a paragraph, number < 10 should be expressed in English and number > 10 should be expressed as Arabic numerals. 12345678 should be written as 12,345,678.

2.4.11 Equations

Equations should be editable and not appear in a picture format. Authors are advised to use either the Microsoft Equation Editor or the MathType for display and inline equations.
Display equations should be numbered consecutively, using Arabic numbers in parentheses;
Inline equations should not be numbered, with the same/similar size font used for the main text.

2.4.12 Headings

In the main body of the paper, three different levels of headings may be used.
Level one headings: they should be in bold, and numbered using Arabic numbers, such as **1. INTRODUCTION**, and **2. METHODS**, with all letters capitalized;
Level two headings: they should be in bold and numbered after the level one heading, such as **2.1 Statistical analyses**, **2.2** ..., **2.3**..., *etc*., with the first letter capitalized;
Level three headings: they should be italicized, and numbered after the level two heading, such as *2.1.1 Data distributions*,and *2.1.2 outliers and linear regression*, with the first letter capitalized.

2.4.13 Text Layout

As the electronic submission will provide the basic material for typesetting, it is important to prepare papers in the general editorial style of the journal.
The font is Times New Roman;
The font size is 12pt;
Single column, 1.5× line spacing;
Insert one line break (one Return) before the heading and paragraph, if the heading and paragraph are adjacent, insert a line break before the heading only;
No special indentation;
Alignment is left end;
Insert consecutive line numbers;
For other details please refer to the Manuscript Templates.

2.5 Submission Link

Submit an article via https://oaemesas.com/login?JournalId=ir.

3. Publication Ethics Statement

OAE is a member of the Committee on Publication Ethics (COPE). We fully adhere to its Code of Conduct and to its Best Practice Guidelines.

The Editors of this journal enforce a rigorous peer-review process together with strict ethical policies and standards to guarantee to add high-quality scientific works to the field of scholarly publication. Unfortunately, cases of plagiarism, data falsification, image manipulation, inappropriate authorship credit, and the like, do arise. The Editors of *IR* take such publishing ethics issues very seriously and are trained to proceed in such cases with zero tolerance policy.

Authors wishing to publish their papers in *IR* must abide by the following:

The author(s) must disclose any possibility of a conflict of interest in the paper prior to submission;
The authors should declare that there is no academic misconduct in their manuscript in the cover letter;
Authors should accurately present their research findings and include an objective discussion of the significance of their findings;
Data and methods used in the research need to be presented in sufficient detail in the manuscript so that other researchers can replicate the work;
Authors should provide raw data if referees and the Editors of the journal request;
Simultaneous submission of manuscripts to more than one journal is not tolerated;
Republishing content that is not novel is not tolerated (for example, an English translation of a paper that is already published in another language will not be accepted);
The manuscript should not contain any information that has already been published. If you include already published figures or images, please get the necessary permission from the copyright holder to publish under the CC-BY license;
Plagiarism, data fabrication and image manipulation are not tolerated;
Plagiarism is not acceptable in OAE journals.

Plagiarism involves the inclusion of large sections of unaltered or minimally altered text from an existing source without appropriate and unambiguous attribution, and/or an attempt to misattribute original authorship regarding ideas or results, and copying text, images, or data from another source, even from your own publications, without giving credit to the source.

As to reusing the text that is copied from another source, it must be between quotation marks and the source must be cited. If a study's design or the manuscript's structure or language has been inspired by previous studies, these studies must be cited explicitly.

If plagiarism is detected during the peer-review process, the manuscript may be rejected. If plagiarism is detected after publication, we may publish a Correction or retract the paper.

Falsification is manipulating research materials, equipment, or processes, or changing or omitting data or results so that the findings are not accurately represented in the research record.

Image files must not be manipulated or adjusted in any way that could lead to misinterpretation of the information provided by the original image.

Irregular manipulation includes: introduction, enhancement, moving, or removing features from the original image; the grouping of images that should be presented separately, or modifying the contrast, brightness, or color balance to obscure, eliminate, or enhance some information.

If irregular image manipulation is identified and confirmed during the peer-review process, we may reject the manuscript. If irregular image manipulation is identified and confirmed after publication, we may publish a Correction or retract the paper.

OAE reserves the right to contact the authors' institution(s) to investigate possible publication misconduct if the Editors find conclusive evidence of misconduct before or after publication. OAE has a partnership with iThenticate, which is the most trusted similarity checker. It is used to analyze received manuscripts to avoid plagiarism to the greatest extent possible. When plagiarism becomes evident after publication, we will retract the original publication or require modifications, depending on the degree of plagiarism, context within the published article, and its impact on the overall integrity of the published study. Journal Editors will act under the relevant COPE guidelines.

4. Authorship

Authorship credit of *IR* should be solely based on substantial contributions to a published study, as specified in the following four criteria:

1. Substantial contributions to the conception or design of the work, or the acquisition, analysis, or interpretation of data for the work;
2. Drafting the work or revising it critically for important intellectual content;
3. Final approval of the version to be published;
4. Agreement to be accountable for all aspects of the work in ensuring that questions related to the accuracy or integrity of any part of the work are appropriately investigated and resolved.

All those who meet these criteria should be identified as authors. Authors must specify their contributions in the section Authors' Contributions of their manuscripts. Contributors who do not meet all the four criteria (like only involved in acquisition of funding, general supervision of a research group, general administrative support, writing assistance, technical editing, language editing, proofreading, *etc*.) should be acknowledged in the section of Acknowledgement in the manuscript rather than being listed as authors.

If a large multiple-author group has conducted the work, the group ideally should decide who will be authors before the work starts and confirm authors before submission. All authors of the group named as authors must meet all the four criteria for authorship.

5. Reviewers Exclusions

You are welcome to exclude a limited number of researchers as potential Editors or reviewers of your manuscript. To ensure a fair and rigorous peer review process, we ask that you keep your exclusions to a maximum of three people. If you wish to exclude additional referees, please explain or justify your concerns—this information will be helpful for Editors when deciding whether to honor your request.

6. Editors and Journal Staff as Authors

Editorial independence is extremely important and OAE does not interfere with Editorial decisions. Editorial staff or Editors shall not be involved in processing their own academic work. Submissions authored by Editorial staff/Editors will be assigned to at least two independent outside reviewers. Decisions will be made by the Editor-in-Chief, including Special Issue papers. Journal staff are not involved in the processing of their own work submitted to any OAE journals.

7. Conflict of Interests

OAE journals require authors to declare any possible financial and/or non-financial conflicts of interest at the end of their manuscript and in the cover letter, as well as confirm this point when submitting their manuscript in the submission system. If no conflicts of interest exist, authors need to state "All authors declared that there are no conflicts of interest". We also recognize that some authors may be bound by confidentiality agreements, in which cases authors need to state "All authors declared that they are bound by confidentiality agreements that prevent them from disclosing their competing interests in this work".

8. Editorial Process

8.1. Pre-Check

New submissions are initially checked by the Managing Editor from the perspectives of originality, suitability, structure and formatting, conflicts of interest, background of authors, *etc*. Poorly prepared manuscripts may be rejected at this stage. If your manuscript does not meet one or more of these requirements, we will return it for further revisions.

Once your manuscript has passed the initial check, it will be assigned to the Assistant Editor, and then the Editor-in-Chief, or an Associate Editor in the case of a conflict of interest, will be notified of the submission and invited to review. Regarding Special Issue paper, after passing the initial check, the manuscript will be successively assigned to the Assistant Editor, and then to the Editor-in-Chief, or an Associate Editor in the case of conflict of interest for the Editor-in-Chief to review. The Editor-in-Chief, or the Associate Editor may reject manuscripts that they deem highly unlikely to pass peer review without further consultation. Once your manuscript has passed the Editorial assessment, the Associate Editor will start to organize peer-review.

All manuscripts submitted to *IR* are screened using CrossCheck powered by iThenticate to identify any plagiarized content. Your study must also meet all ethical requirements as outlined in our Editorial Policies. If the manuscript does not pass any of these checks, we may return it to you for further revisions or decline to consider your study for publication.

8.2. Peer Review

IR operates a single-blind review process, which means that reviewers know the names of authors, but the names of the reviewers are hidden from the authors. The scientific quality of the research described in the manuscript is assessed

by a minimum of two independent expert reviewers. The Editor-in-Chief is responsible for the final decision regarding acceptance or rejection of the manuscript.

All information contained in your manuscript and acquired during the review process will be held in the strictest confidence.

8.3. Decisions

Your research will be judged on scientific soundness only, not on its perceived impact as judged by Editors or referees. There are three possible decisions: Accept (your study satisfies all publication criteria), Invitation to Revise (more work is required to satisfy all criteria), and Reject (your study fails to satisfy key criteria and it is highly unlikely that further work can address its shortcomings). All of the following publication criteria must be fulfilled to enable your manuscript to be accepted for publication:

Originality
The study reports original research and conclusions.
Data availability
All data to support the conclusions either have been provided or are otherwise publicly available.
Statistics
All data have been analyzed through appropriate statistical tests and these are clearly defined.
Methods
The methods are described in sufficient detail to be replicated.
Citations
Previous work has been appropriately acknowledged.
Interpretation
The conclusions are a reasonable extension of the results.
Ethics
The study design, data presentation, and writing style comply with our Editorial Policies.

8.4. Revisions

Authors are required to submit the revised manuscript within one week if minor revision is recommended while two weeks if major revision recommended or one month if additional experiments are needed. If authors need more than one month to revise their manuscript, we usually require the authors to resubmit their paper. We request that a document of point-to-point response to all comments of reviewers and the Editor-in-Chief or the Associate Editor should be supplied along with the revised manuscript to allow quick assessment of your revised manuscript. This document should outline in detail how each of the comments was addressed in the revised manuscript or should provide a rebuttal to the criticism. Manuscripts may or may not be sent to reviewers after revision, dependent on whether the reviewer requested to see the revised version. Apart from in exceptional circumstances, *IR* only supports a round of major revision per manuscript.

9. Contact Us

Journal Contact

Intelligence & Robotics Editorial Office
Suite 1504, Plaza A, Xi'an National Digital Publishing Base,
No. 996 Tiangu 7th Road, Gaoxin District, Xi'an 710077, Shaanxi, China.

Managing Editor

Lijun Jin
Email: editorial@intellrobot.com

OAE Publishing Inc. (https:oaepublish.com) is a multidisciplinary open-access publishing company, founded in Los Angeles in 2015. Until now, OAE has been recognized by authoritative organizations in publishing industries,such as the *ORCID, COPE*, Scientific, Technical and Medical Publishers (STM), Crossref, and EASE.

As of June 2022, more than 1,200 outstanding scholars have joined OAE, who are from world-renowned universities and research institutions, including European Academy of Sciences, American Academy of Invention Sciences, Chinese Academy of Sciences, Royal Academy of Sciences of Belgium, British Academy of Medical Sciences, *etc*. There are more than 30 journals founded by OAE (https:oaepublish.com/about/journals), such as *Intelligence&Robotics*, *Journal of Materials Informatics, Complex Engineering Systems, Journal of Smart Environments and Green Computing*, and *Soft Science*, *etc.* Part of journals have been indexed by Scopus and CAS. We are currently working on database application including PubMed and ESCI. Up to June 2022, 3,154 articles have been published online, with 10,944,568 hits and 2,285,864 downloads. In the future, OAE Publishing Company will continue to found more quality journals with outstanding scholars, to promote the global academic development.

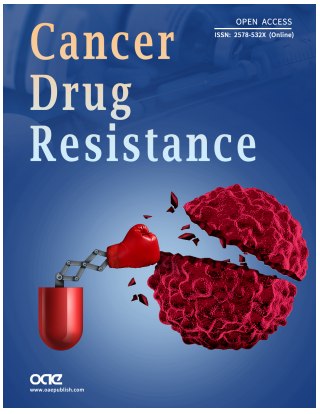

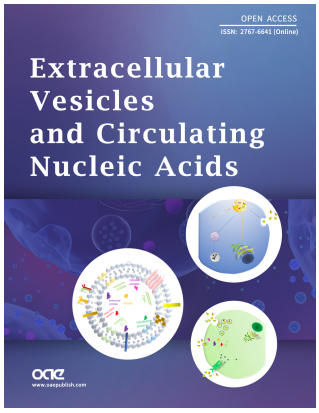

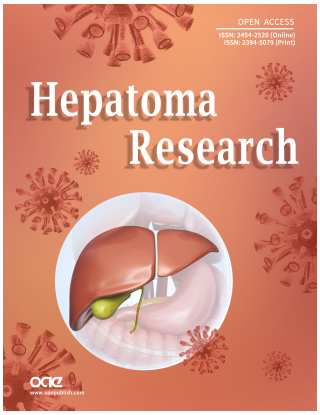

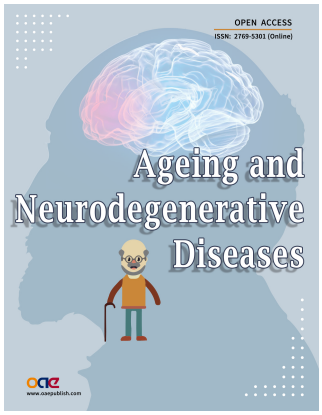

OAE Official Website